3

The Rings of Saturn

J. N. CUZZI, G. FILACCHIONE, AND E. A. MAROUF

3.1 INTRODUCTION

One could become an expert on Saturn's iconic rings pretty easily in the early 1970s, as very little was known about them beyond the distinction between the A, B, and C rings, and the Cassini Division or "gap" between rings A and B (Alexander, 1962; Bobrov, 1970). Water ice was discovered spectroscopically on the ring particle surfaces, and radar and microwave emission observations proved that the particles must be centimeters to meters in size, consisting *primarily*, not just superficially, of water ice (Pollack, 1975). While a 2:1 orbital resonance with Mimas had long been suspected of having something to do with the Cassini Division, computers of the time were unable to model the subtle dynamical effects that we now know to dominate ring structure.

This innocent state of affairs was exploded by the Voyager 1 and 2 encounters in 1980 and 1981. Spectacular images revealed filigree structure and odd regional color variations, and exquisitely detailed radial profiles of fluctuating particle abundance were obtained from the first stellar and radio occultations, having resolution almost at the scale of single particles. Voyager-era understanding was reviewed by Cuzzi *et al.* (1984) and Esposito *et al.* (1984). While the Voyager data kept ring scientists busy for decades, planning which led to the monumentally successful NASA-ESA-ASI Cassini mission, which arrived in 2004, had been under way even before Voyager got to Saturn. A review of pre-Cassini knowledge of Saturn's Rings can be found in Orton *et al.* (2009).

This chapter will build on recent topical and process-specific reviews that treat the gamut of ring phenomena and its underlying physics in considerable detail (Colwell *et al.*, 2009; Cuzzi *et al.*, 2009; Horányi *et al.*, 2009; Schmidt *et al.*, 2009; Esposito, 2010; Tiscareno, 2013b; Esposito, 2014). We will follow and extend the general organization of Cuzzi *et al.* (2010), the most recent general discussion of Saturn's rings. For brevity and the benefit of the reader, we will frequently refer to the above review articles instead of directly to the primary literature they discuss. We will focus on new work since 2010, within a general context, and will connect our high-level discussions with more detailed chapters in this volume.

In Section 3.2 we overview the general properties of Saturn's rings. We then build from the ground up with a discussion of individual particle sizes and the local microstructure (Sections 3.3 and 3.4). We next proceed through the main ring structural properties, starting with the A and B rings, which are similar in many ways, followed by the Cassini Division and C rings, which are also similar, finally describing the innermost D ring and the peripheral F ring (Sections 3.5.1–3.5.6). We next discuss the "diffuse" or dusty rings and ring arcs (Section 3.6), followed by the composition of ring material and how it varies radially (Section 3.7). In Section 3.8 we turn to the so-called "ring-moons," both external to and embedded within the rings. We briefly discuss the ring atmosphere of gas and dust, and possible connections to the planet, in Section 3.9. We summarize recent thinking on the origin and evolution of the rings in Section 3.10, and close with a short discussion of major outstanding puzzles and challenges (Section 3.11).

3.2 OVERVIEW

Diametrically, the main (A, B, C, and D) rings cover a distance of about 274 000 km, more than 2/3 of the distance between the Earth and Moon. Yet their local vertical extent is less then tens of meters – the equivalent of a sheet of paper a mile across. Figure 3.1 shows a Cassini image of the lit face of the rings, aligned with a radial plot of the *normal optical depth* $\tau = -\mu \ln(I/I_o)$, where I_o and I represent incident and directly transmitted intensity and μ is the cosine of the viewing angle from the ring normal. Physically, the optical depth is the vertical integral of the extinction cross section per particle weighted by the particle size distribution. Optical depth is a function of wavelength (Section 3.3) and of geometry because of local inhomogeneities (Section 3.4) but it is plain that most of the ring material is in the outer 2/3 of the B ring. The faint, narrow F ring is faintly visible in the image at the right, 3400 km outside the A ring outer edge.

A good visual idea of the mass distribution in the main rings is provided by Figure 3.2, in which the Sun illuminates the opposite side of the ring. The dark, nearly opaque region is the outer 2/3 of the B ring. Even in the depths of the central B ring, a few narrow lanes can be perceived where a little light gets through. The inner third or so of the B ring is more translucent, with roughly as much material as the A ring (Figure 3.1). The Cassini Division actually contains both a series of low brightness bands in its inner half, and a very bright band in its outer half – the so-called "ramp." The optical depths of these regions are comparable, and the brightness difference is caused by more reflective particles in the inner part of the Cassini Division (Section 3.5.3). A similar effect is seen in the outer C ring, where a twin ramp (both structurally and compositionally) is found just within the abrupt inner B ring edge

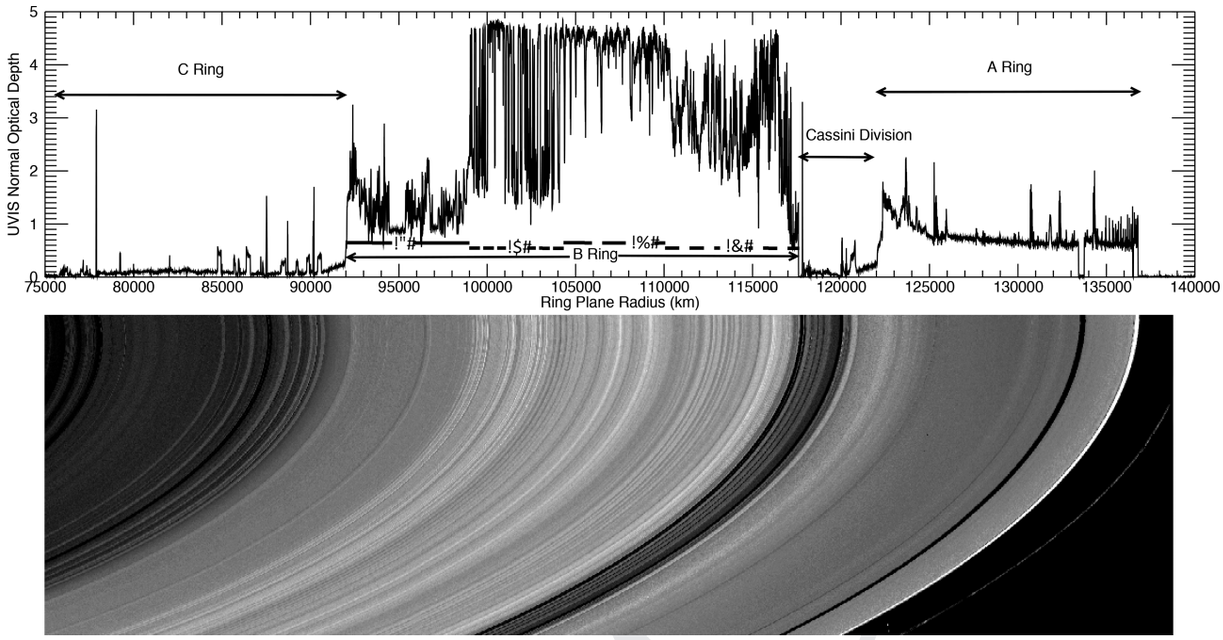

Figure 3.1 A global view of Saturn's main rings, aligned with a plot of the local normal optical depth τ as a function of radius (figure adapted from Colwell *et al.* (2009). Several subregions of the B ring, here designated B1–B4, have distinct properties, as described below and in Cuzzi *et al.* (2009).

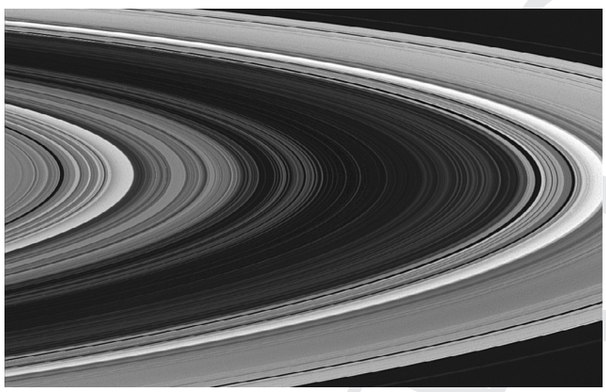

Figure 3.2 A view of the unlit face of the main rings, in which the optically thick central and outer B ring appears dark. The very inner edge of the B ring is also opaque. Note a few faint, narrow, partially transparent bands even in the darkest core of the B ring. The brightest features are the "ramps" at the outer edge of the C ring and Cassini Division. The outer C ring shows a series of bright "plateaus" arrayed about the Maxwell gap, which itself contains a narrow eccentric ringlet much like the ϵ ring of Uranus (see also Figure 3.9). Image PIA06533, NASA/JPL and SSI.

(see Figure 3.1 and Section 3.10). In the outer C ring, the Maxwell Gap contains an unexplained eccentric ringlet, and is straddled by a curiously symmetric and also unexplained set of "plateaus" (Section 3.5.4). Not shown in this figure are the barely visible D ring (Section 3.5.5) lying inside the C ring, and the diffuse E and G rings (Section 3.6), visible primarily in their tiny dust grain component, which lie well outside the main rings.

3.3 RING-PARTICLE SIZE DISTRIBUTION

A breakthrough in understanding of the ring-particle size distribution came during the 1970's, based on active and passive radio observations from Earth. Measurements of the radar cross section at 3.5 and 12.6 cm wavelengths found it to be about 60% of the combined projected geometric cross-sectional area of the A and B rings, depolarized, and wavelength independent (Goldstein and Morris, 1973; Goldstein *et al.*, 1977). This ruled out the possibility that the rings were composed mainly of micrometer-size particles, as had been the previous belief.

The high reflectivity and strong depolarization was first explained by Pollack *et al.* (1973) as due to nearly pure water ice particles with size of the same order as the observation wavelength. The wavelength independence was further interpreted by Cuzzi and Pollack (1978) as indicating the existence of a broad size distribution. They found that a many-particle-thick layer of centimeter to meter radius particles having a differential power-law distribution of radius with slope index $q = 3$ (see Equation 3.3), was most consistent with the radar data. An analysis by Cuzzi *et al.* (1980) of interferometric observations of the ring brightness over several wavelength bands in the range 0.34 to 21 cm suggested a cutoff at about 1 m radius in a power-law distribution of index $q = 3$ (with a tradeoff between the cutoff size and power-law slope). An upper cutoff size in the range 0.3 to 5 m was also deduced by Epstein *et al.* (1980) from model fitting of their 3 mm radio brightness observations. (Esposito *et al.*, 1984; Orton *et al.*, 2009).

The Voyager encounters in 1980 and 1981 and the orbiting Cassini spacecraft opened new doors for better characterization of the ring-particle size distribution, with better instrument capabilities, higher spatial resolution, and measurements over

a broad range of observation geometry. The review chapter by Cuzzi *et al.* (2009) serves as a resource for the summary below; here we emphasize new results since 2009. Cassini will continue to acquire new data until September 2017 and analysis of much of the already collected data is yet to be completed; hence a complete ring particle size story is yet to be written. Moreover, in this section we discuss only the size distribution of particles in the main rings; for more discussion of particle sizes in the F ring and the diffuse rings, see Horányi *et al.* (2009), Sections 3.5.6 and 3.6, and Chapters 12 and 13.

3.3.1 Some Common Threads

Most of the ring-particle size information discussed below is derived from radio, stellar, and solar occultation observations. The occultation geometry is ideally suited to provide size information from two distinct measurement types. The first is measurement of the extinction of the incident electromagnetic radiation passing straight through the rings (the direct signal) characterized by the normal optical depth. Measurement of how optical depth varies with wavelength constrains particle sizes because the efficiency with which a particle removes energy from the incident radiation depends on its size relative to the wavelength. The second type of measurement involves the near-forward-scattered signal, that is, the collective diffraction pattern of ring particles or particle aggregates. The strength, angular width, and overall shape of the diffraction lobe are primarily controlled by the largest members of the particle size distribution and are relatively insensitive to particle composition and shape.

In both stellar and solar occultations, the incident radiation is incoherent in nature and it is not easy in general to separate the direct and forward scattered contributions to the total measured flux. Different techniques have been developed to achieve this objective, as discussed below (French and Nicholson, 2000; Harbison *et al.*, 2013; Becker *et al.*, 2016). Only in the case of radio occultations, where the spacecraft transmits coherent sinusoidal signals, is the separation straightforward because of the different spectral nature of the direct and scattered signal (Marouf *et al.*, 1982).

Inference of the size information from the measurements requires assumption of a ring model. Parameters of the model can, in principle, be recovered or constrained using either inverse techniques or direct comparison (least-square fit) of model predictions to the observations. Direct inversion has the advantage of not biasing the answer by an *a priori* assumed size distribution. Marouf *et al.* (1983) and Zebker *et al.* (1985) adopt the inversion approach to recover the size distribution of meter and larger particles. The model match/fitting approach is usually less demanding and is the one adopted by most analyses, as summarized below.

Finally, interpreting extinction and forward scattering measurements requires adoption of a physical ring model. Historically, the "classical" model is usually adopted, in which ring particles are uniformly distributed laterally and vertically in a layer that is many particles thick, and are assumed to be in the far field of each other (volume packing fraction $\ll 1$). The normal optical depth τ in this case is given by

$$\tau(\lambda) = \int_0^\infty \pi s^2 \, Q_{ext}(s, \lambda) \, n(s) \, ds, \tag{3.1}$$

where s is the particle radius, λ is the wavelength, Q_{ext} is the extinction efficiency, and $n(s)$ is the size distribution. For $\tau \ll 1$ and assuming particles large compared with the wavelength, the first-order, forward-scattered, signal intensity $I(\theta, \lambda)$ (power per unit area normal to the beam, per unit solid angle), in scattering directions close to the incidence direction, is given by

$$\frac{I(\theta, \lambda)}{I_{inc}} = \frac{e^{-\tau/\mu_o}}{4\pi\mu_o} \int_0^\infty \pi s^2 \, [\frac{2J_1(ks \sin\theta)}{\sin\theta}]^2 \, n(s) \, ds, \tag{3.2}$$

where I_{inc} is the incident intensity, J_1 is the Bessel function of first kind and first order, θ is the scattering angle, $k = 2\pi/\lambda$, and μ_o is the cosine of the incidence angle from the ring normal. A widely adopted model of $n(s)$ is the truncated power law model

$$n(s) = n_o \, (s/s_o)^{-q}, \qquad s_{min} \le s \le s_{max}, \tag{3.3}$$

where $n(s) = n_o$ at some arbitrary $s = s_o$. The measurements are used to determine/constrain the model parameters q, s_{min}, and s_{max}.

The classical ring model is usually adopted for computational simplicity; however, the model suffers from four main limitations which can bias the results. (1) For $\tau > 1$, multiple scattering effects are important and need to be included. Because of the narrow and intense forward diffraction lobe of particles large compared with the wavelength, numerical solutions of the radiative transfer equation can be costly, if feasible at all. Marouf *et al.* (1982, 1983) developed a successive-order of scattering solution especially tailored for diffraction by large particles which is adaptable to efficient numerical computations. (2) The actual rings are likely to be only a few, rather than many, particles thick, as implied by dynamical considerations and by the Voyager radio occultation (Zebker *et al.*, 1985; Schmidt *et al.*, 2009, see also Chapter 16). (3) In regions of gravitational wakes, the assumption of a uniform spatial distribution breaks down. The impact of particle crowding and clustering on both extinction and forward scattering needs to be included in a realistic ring model. (4) The extinction efficiency used in Equation 3.1 to compute optical depth depends also on the fraction of the forward scattered signal captured by the measuring aperture and often cannot be separated from a non-coherent direct signal (Cuzzi, 1985); see also Figure 15.4 of Cuzzi *et al.* (2009). For particles large compared to the wavelength, Q_{ext} varies from 2 when the the direct and diffracted signals are separable, to 1 when they are not. Thus the optical depth measured, for example, by radio occultation is roughly twice as large as that measured by UV stellar occultations. The first is usually referred to as the extinction optical depth and the second as the geometric optical depth. Ring models assumed in analysis of different types of observations below address these limitations to various degrees.

3.3.2 Centimeter to Meter Sizes from Voyager Radio Occultation

The Voyager 1 radio occultation in 1980 (Tyler *et al.*, 1983) was carried out using two coherent sinusoidal radio signals of 3.6 and 13 cm wavelengths (X- and S-band, respectively). Analysis of the forward-scattered signal was based on Equation 3.2 extended to include multiple scattering effects (Marouf *et al.*, 1982). An inversion technique was used to recover $n(s)$ over

the range 1 m $\leq s \leq$ 20 m (Marouf *et al.*, 1983). No specific $n(s)$ model was assumed. For selected broad features in the C and A rings and the Cassini Division (CD), the inversion revealed sharp upper size cutoffs in the few to several meters radius range depending on the feature observed.

Over the range 1 cm $\leq s \leq$ 1 m, Marouf *et al.* (1983) assumed a power-law model with $s_{min} \ll 1$ cm. They used the measured difference in optical depth at the two observation wavelengths (Tyler *et al.*, 1983) to determine the power-law index q. The combined results represented the first recovered size distribution over the 1 cm to several meters range.

A problem with the results was a discontinuity in $n(s)$ at $s = 1$ m. Zebker *et al.* (1985) used a similar inversion approach but replaced the many-particle-thick ring model by a physically thin-layer model, which limits the maximum number of total scattering events within the layer to a finite value N. They then searched for values of N that removed the discontinuity at $s = 1$ m, obtaining a nearly continuous size distribution extending from 1 cm to several meters.

The results of Zebker *et al.* (1985) are summarized (together with some other results discussed below) in Table 15.1 of Cuzzi *et al.* (2009). In the C ring, $s_{max} \simeq 5$ m and $q = 3.1$. In the CD "ramp" (Section 3.5.4), $s_{max} \simeq 7.5$ m, and $q = 2.8$; moving outward in the A ring, s_{max} increases from ∼5 to ∼9 m while q increases from 2.7 to 3. In all cases, N was no more than 3 – a layer only a few times as thick as the size of the largest particles (Zebker and Tyler, 1984; Schmidt *et al.*, 2009, see also Chapter 16).

3.3.3 Millimeter to Meter Sizes from Cassini Radio Occultations

Cassini enjoys two main advantages over Voyager. The first is the opportunity to conduct multiple radio occultations over a range of observation geometries and a range of ring opening angles. The second is the addition of a third observing wavelength (0.94 cm, Ka-band) to the two Voyager ones. The shorter wavelength extended the measurement sensitivity to particles in the millimeter size range.

A few optimized Cassini radio occultations resolved scattering by ring features of radial width approaching ∼ 300 km, about four times better than Voyager. Inverting the observations of over 50 subregions of the C ring background structure consistently yields sharp upper size distribution cutoffs of about 5 to 6 m (Marouf *et al.*, 2013). The measured differential X/S optical depth (see Figure 15.1 of Cuzzi *et al.*, 2009) yields power-law indices in the range $3.15 \leq q \leq 3.35$, with some subtle variations in the C ring wavy region (Marouf *et al.*, 2013). These inferences are consistent with Voyager results. The measured X/Ka differential optical depth provides new strict limits on the minimum particle radius of about 4 mm throughout the C ring background structure (Marouf *et al.*, 2008, 2013); see also Figures 15.1 and 15.3 of Cuzzi *et al.* (2009). Five optically thick confined features within the C ring (the plateaus; see Section 3.5.4) have interesting particle size differences compared to the wavy background structure (Marouf *et al.*, 2013). Their exact nature and potential cause are still being investigated.

Remarkable X/S optical depth differences characterize the A Ring, as was first revealed by Voyager (Tyler *et al.*, 1983) and more recently by Cassini; (see Figure 15.1 of Cuzzi *et al.*, 2009). The lack of X/S differential in the inner region of the A ring inwards of about 128 000 km, suggest either a minimum size larger than few tens of centimeters, or a shallow power-law index $q < 2.7$. Voyager yielded $q = 2.7$ to 2.75 over this region (Zebker *et al.*, 1985). The systematic increase in the X/S differential outside of ∼128 000 km indicates a systematic and dramatic increase in the abundance of cm-sized particles with increasing ring radius, likely due to increased dynamical activities (waves) known to permeate this A ring region. By comparison with the above values for the inner A ring, the observed X/Ka differential limits the minimum size to about 4 mm exterior to the Encke Gap, decreasing to about 3 mm close to the edge, and to about 4 mm in the flat feature of region B1 of the B ring (Marouf *et al.*, 2008; Cuzzi *et al.*, 2009); see Figures 15.1 and 15.3 of the latter. Little detectable S/X/Ka differential in regions B2 and B4 suggest either a minimum size larger than a few tens of centimeters, or a shallow power law index $q < 2.7$.

Results above for rings A and B do not include the effects of particle clustering due to gravitational wakes, which are known to permeate these regions, and thus must be considered with caution. The effect of wakes on extinction and forward scattering measurements continues to be investigated with randomly blocked diffraction screen models that include elongated clusters of ring particles embedded in an otherwise classical ring model (Marouf *et al.*, 2014). Numerical simulations of the diffraction patterns clearly show superposed cylindrical and spherical components. The first has a narrow diffraction pattern of angular width controlled by the width and height of each wake clump. The second has a broader angular width controlled by the individual particles. The strength and shape of the latter are consistent with diffraction by a classical ring model of optical depth equal to that of the simulated model. Both the cylindrical and spherical diffraction components are detectable in Cassini measurements. The measured angular shape of the cylindrical component constrains the width and height of typical wake clumps. Preliminary results for observed scattering by inner A ring features suggest wakes that are about a few tens of meters wide and several meters thick (Marouf *et al.*, 2014). In principle, the measured broad, symmetrical component may be used to recover the underlying ≥ 1 m *particle* size distribution from which the wake clumps are constructed, as was the case for Voyager. The wake signal (narrow cylindrical component) was not seen in the Voyager data because of a combination of low elevation angle and longitude sampled.

3.3.4 Millimeter Sizes from Cassini VIMS Solar Occultations

Cassini is the first spacecraft to observe occultation of the Sun by Saturn's ring system. The VIMS instrument "images" light at 0.9 to 5.2 μm wavelengths, extinguished and forward scattered by ring particles (Harbison *et al.*, 2013). The data are particularly sensitive to diffraction by particles in the radius range 100 μm to a few mm, nicely complementing the size range covered by radio occultations.

Unlike for radio occultations, separating the directly transmitted and scattered flux contributions of incoherent forward

scattered light is not straightforward. Harbison *et al.* (2013) remove the direct signal (the Sun's image) by integrating the observed forward scattered signal intensity over scattering angles larger than the Sun's radius as observed at about 9 AU (0.5 mrad). The computed flux is then compared with theoretical predictions to constrain s_{min} of a powerlaw size distribution. They assume known q and s_{max}, guided by the Voyager radio results: $q = 3.1$ and $s_{max} = 10$ m in the C ring; $q = 2.75$ – 2.90 and $s_{max} = 10$ m in the A ring.

In the C ring, the model reasonably assumes a classical ring layer and single scattering (Equation (3.2)). Comparisons of computed flux with data from 4 solar occultations yield $s_{min} = 4.1^{+3.8}_{-1.3}$ mm. Allowing q to vary between 2.95 and 3.5 yields s_{min} varying between 0.3 and 1 cm, comparable to the 4 mm estimate from Cassini radio occultations.

In the more optically thick A ring region inward of the Encke Gap, Harbison *et al.* (2013) include up to third-order multiple scattering contributions to forward scattering by adapting the multiple scattering formulation of Zebker *et al.* (1985). They also extend their model to include the likely effects of gravitational wakes, known to be present in the A ring (Colwell *et al.*, 2007; Hedman *et al.*, 2007b). Specifically, they assume the wake clumps are perfectly opaque to the incident radiation, with known geometric parameters from Hedman *et al.* (2007b), and that the gaps between the wakes have known optical depth between 0.3 and 0.6 (Nicholson and Hedman, 2010a). Using a similar approach to that for the C ring, they infer $s_{min} < 0.34$ mm for $q = 2.75$, and $s_{min} < 0.56$ mm (-0.16, +0.35) for $q = 2.9$.

3.3.5 Millimeter Sizes from Cassini UVIS Stellar Occultations

The measured photon count during a Cassini UVIS stellar ring occultation (110 to 190 nm wavelength) includes contributions from both the attenuated starlight passing straight through the rings (the direct signal) and forward scattering by all particles within the instrument field of view (FOV) (the scattered signal). Only in the "free-space" vicinity of a sharp ring edge is the scattered signal separable from the direct signal. Its relative magnitude is small (∼6%) but detectable at the outer edge of the A ring and the inner and outer edges of the Encke Gap (Becker *et al.*, 2016). Its magnitude, width, and shape are primarily controlled by q and s_{min} of the size distribution of the population of ring particles within a few tens of kilometers of the observed ring edge.

Becker *et al.* (2016) assume single scattering (Equation (3.2)) and add up contributions from all ring particles within the instrument FOV at any given time. They construct model diffraction patterns parameterized by q and s_{min} of an assumed power-law size distribution of fixed s_{max}= 8.9 m based on the Voyager radio results. The model diffraction patterns are then compared with the measurements to infer q and s_{min}. Neither multiple scattering nor wake effects are included in the model. They note, however, that ignoring multiple scattering (which broadens the diffraction pattern) could result in underestimates of s_{min}.

For the outer edge of the A ring, the best fit of the synthetic diffraction pattern to the measurements suggests s_{min} ranging from 1 to 10 mm with q from 2.8 to 3.5. The q and s_{min} estimates are correlated. Becker *et al.*'s mean estimates of $s_{min} = 4.5$ mm and $q = 3.2$ are in good agreement with inferences from Cassini radio occultations (see Figuer 15.3 of Cuzzi *et al.*, 2009). None of the Becker *et al.* (2016) best fit models indicate an $s_{min} < 1$ mm, unless $q < 2.8$, which is unlikely given the Voyager and Cassini radio results for the outer A ring.

Becker *et al.* note that the observed diffraction patterns exterior to the Encke Gap outer edge are not as strong as those observed exterior to the A ring edge and hence are harder to model. They estimate s_{min} ranging from 3 to 30 mm with q from 2.9 to 3.5. The q and s_{min} estimates appear to be more strongly correlated than in the A ring edge case. Their mean estimates are s_{min} = 9.3 mm and the mean $q = 3.1$. As for the A ring edge, no model with particle sizes below a few millimeters matches the observations, suggesting that the abundance of such particles is small in the sampled region a few tens of km outside the Encke Gap. Diffraction patterns observed interior to the inner edge of the Encke Gap are not as evident, suggesting relative depletion of mm-sized particles in that region.

3.3.6 Millimeter Sizes from Cassini UVIS/VIMS Stellar Occultation

Similar to the 3-wavelength radio occultations, inference of ring-particle sizes from differential optical depth measurement is also possible from combined VIMS/UVIS occultations (Jerousek *et al.*, 2014; Colwell *et al.*, 2014). Particles of radii less than about ∼9 mm diffract light outside the VIMS FOV, thus their extinction efficiency (Q_{ext} in Equation (3.1)) is larger for the VIMS occultation than for the UVIS occultation where the diffracted lobe *is* captured (see Section 3.3.1). Adjusted for the same observation geometry, reliable measurement of a UVIS/VIMS differential optical depth constrains the abundance of sub-centimeter sized particles with high spatial resolution. In the C ring region where gravitational wakes are absent so that the measured normal optical depth is not geometry dependent, Jerousek *et al.* (2014) report an s_{min} that is relatively constant across the C ring with mean value of ∼6 mm, in general agreement with other minimum size inferences discussed above. In the outer A ring, the observed differential optical depth indicates a significant population of sub-centimeter size particles of increasing fraction as the edge is approached (Colwell *et al.*, 2014); recall that the observed X/S/Ka differential optical depth of that region suggests a small-size cutoff at radii of 3 to 4 mm as discussed in Cuzzi *et al.* (2009) and Section 3.3.3. Future expansion of this important VIMS-UVIS combination would be very useful to study this interesting size range at high radial resolution.

3.3.7 Centimeter to Meter Sizes from Earth-Based Stellar Occultations

The 1989 stellar occultation of 28 Sgr was observed across the full ring system at 0.9, 2.1, and 3.9 μm wavelengths (French and Nicholson, 2000; Cuzzi *et al.*, 2009). The measured flux was a blend of directly attenuated starlight with light diffracted into the detector from other regions of the rings. French and Nicholson (2000) used the Voyager photopolarimeter (PPS) optical depth profile to estimate and remove the direct signal

contribution to the observed total flux, hence constructing a profile of the forward-scattered signal across the ring system. This technique, however, may introduce systematic errors since, for laterally inhomogeneous layers such as we now know most of the optically thick rings to be, the normal optical depth inferred from low elevation-angle observations (such as Voyager PPS) is biased by a small fraction of empty gaps and may not accurately reproduce the normal optical depth at large opening angles (such as for 28 Sag).

Assuming a classical ring model of each of the main ring regions (A, CD, B, and C), single scattering (Equation (3.2)), and a power-law size distribution, French and Nicholson inferred model parameters that provided a good match to the observations. The power-law parameters were fit separately for each main ring region, were assumed uniform across each region, and were selected to provide a compromise match to data at all three observation wavelengths.

French and Nicholson (2000) conclude that s_{max} = 20 m provides the best match to the data over the A and B rings and the CD, and a smaller s_{max} = 10 m in the C ring, hence providing an independent confirmation of the prevalence of meter-size particles throughout the ring system. An s_{min} = 1 cm best matched the C ring data. The estimate was confirmed by several of the Cassini results discussed above. The A ring was also split into two regions: interior and exterior to the Encke Gap (A1 and A2 below, respectively), and a similar $s_{min} \sim 1$ cm also characterizes region A2. However, a much larger s_{min} = 30 cm characterizes the B ring and region A1. French and Nicholson (2000) did not separate different segments of the B Ring, and while such a large s_{min} is probably consistent with Cassini RSS results for regions B2–B4, it is probably not applicable to region B1 (Section 3.3.3). The power-law index $q = 2.75$ was inferred for the B ring, the CD, and region A1, with value 2.9 in region A2, and a steeper $q = 3.1$ in the C ring.

3.3.8 Meter Sizes from Voyager PPS Stellar Occultations (Excess Variance Method)

Showalter and Nicholson (1990) argued that the photon count measured during the Voyager PPS stellar occultation is a Poisson random variable whose mean and variance are determined by the statistics of the random fraction of observed ring area not blocked by ring particles. Each of the statistical averages included two components: one is due to the intrinsic random nature of the incident starlight and the other is due to "ring noise," that is, the random blocking of the incident starlight by large individual particles.

The contribution of the second component to the count variance (the "excess variance") can be estimated from the data with a spatial resolution of a few to tens of kilometers (see Figure 15.7 of Cuzzi *et al.*, 2009), and is controlled by an "effective" particle size $s_{\rm eff}$ which is equal to the square root of the ratio of the fourth and second moments of the particle size distribution. For power-law distributions of $q \sim 3$, $s_{\rm eff}$ is strongly weighted toward the largest particle sizes.

Using this technique, Showalter and Nicholson (1990) estimated effective sizes of 1 to 4 m in the C ring, 6 to 9 m in the B ring, 1 to 4.5 m in the CD, and 9 to 12 m in the A ring. In general, these variance-based estimates provide an independent confirmation of the importance of meter-sized particles in all ring regions, but are larger than the "effective sizes" obtained the same way from Voyager and Cassini radio occultation size distributions by about a factor of 2 in the C Ring and a factor of 6 in the A Ring (Table 15.1 of Cuzzi *et al.*, 2009).

3.3.9 Sizes from Cassini UVIS Stellar Occultation Excess Variance

Numerous Cassini UVIS stellar occultations yield a rich set of excess variance profiles observed over a range of ring viewing geometry and ring opening angle (e.g., Colwell *et al.*, 2011b) (the VIMS field of view, Fresnel zone, and sampling times are less optimal for this technique). Significantly different dependencies of excess variance on normal optical depth are observed over the main ring regions and within local features of the same region. Colwell *et al.* (2012, 2013) relate the observed excess variance to an "autocorrelation length" L, likely a measure of some effective size controlled by statistical averages of the size distribution. They indicate that effective sizes within the inner 700 km of the B ring are different from the rest of the B ring and are also different among the B1–B4 regions (which had been identified solely based on their optical depth structure; Colwell *et al.*, 2009). They also indicate that particle sizes in the C ring plateaus are, in some average sense, smaller than in the rest of the C ring. Comparison of the observed excess variance behavior with statistics computed from model-based studies assuming a range of particle size distributions holds promise for fine spatial resolution characterization of particle size populations across the ring system (Colwell *et al.*, 2012, 2013).

3.3.10 Why a Millimeters to Meters Power-Law Distribution of $q \sim 3$?

Although the focus of our summary above has been a review of observational inferences of ring-particle sizes, the results invite obvious "why" questions. Why a power-law size distribution of power law index $q \sim 3$? Why the sharp upper size cutoff of several meters? Why the relative depletion of particles smaller than few to several millimeters?

Soon after the Voyager encounter, it was proposed that the revealed meter size particles may actually be aggregates many meters in size accreted from "grains" of much smaller size. The low-strength aggregates disintegrate by tidal stresses only to form again by gravitational accretion, hence dubbed dynamic ephemeral bodies, or DEBs (Davis *et al.*, 1984; Weidenschilling *et al.*, 1984). A DEB survives few days before it's torn apart.

Building on the pioneering DEBs idea, Longaretti (1989) developed an analytic theory to characterize relevant accretion and erosion processes. When the differential keplerian velocity of a pair of colliding aggregates exceeds the dispersion velocity, erosion is enhanced, depleting aggregates of radius larger than a "critical" radius s_c. For conditions in Saturn's rings, $s_c \simeq 5$ m, in good agreement with the observed s_{max}.

Longaretti uses his characterization of the accretion and erosion process (and the assumption that fragments generated during collisions have a power-law size distribution) to develop an approximate power-law ring particle size distribution over

each of the ranges: $s < s_c$ and $s > s_c$. The power law index over each segment is q_1 and q_2, respectively; $q_2 > q_1$. Limits on q_1 and q_2 are set by the parameters characterizing the erosion mechanics.

More recently Brilliantov *et al.* (2013), also starting from the DEBs assumption, used kinetic theory to investigate evolution of the particle size distribution, balancing aggregation and fragmentation. Binary collisions yield an outcome (sticking, rebound, breakup) that depends on the velocity dispersion. They determine the frequency of all collision outcome types and solve the Boltzmann equation analytically under various assumed conditions. For the case when: (1) kinetic energy of random motion is equally distributed among all sizes, (2) velocity dispersion of particles of all sizes is equal, and (3) debris particles generated by fragmentation during a collision have a power-law size distribution, Brilliantov *et al.* derive a steady-state solution for the ring particle size distribution

$$n(s) \sim s^{-q}\, e^{-(s/s_c)^3}, \tag{3.4}$$

where $2.75 \leq q \leq 3.5$ and s_c = constant = s_1/λ, s_1 is the size of the grain and λ is the ratio of the frequencies of the disruptive and coagulative collisions. The distribution is a power law for $s \ll s_c$ and decays exponentially for $s \gg s_c$, transitioning between the two asymptotic behaviors around $s = s_c$. The upper size "cutoff" is implied by the analytic solution without invoking tidal stresses. The exponential part of the distribution explains the observed sharp cutoff. The derived range $2.75 \leq q \leq 3.5$ is in remarkable agreement with inferences from the radio occultation measurements discussed above. Brilliantov *et al.* claim that the power-law size distribution and the q-range are universal, applicable to other ring systems as well. In a sense, their parameter λ was implicit in the approach of Longaretti (1989). Future work should explore the assumption of size-independent relative velocities, however, as this may not be the case in an equipartition situation with rotating particles (Ohtsuki, 2006; see also Chapter 16).

Neither Longaretti (1989) nor Brilliantov *et al.* (2013) address the lower cutoff of the size distribution. Bodrova *et al.* (2012) argue that the observed relative depletion of abundance of centimeter and smaller size particles can be explained if adhesion is included in modeling the collisional process. They assume a simple bimodal size distribution model and calculate the rates of accretion and release of small particles, depending on material parameters, sizes, and plausible velocity dispersion of the large carriers and the smaller debris particles.

Adhesive strength increases relative to inertial forces for decreasing particle sizes. Particles smaller than a certain critical size remain tightly attached to the surfaces of the large ones even when the latter collide at their typical speed. For an expected 0.1 to 1 cm/s velocity dispersion and a large particle population in the 5 to 15 m size range, Bodrova *et al.* estimate a critical size of few to few tens of cm for clean ice surfaces and 1 to a few cm for (perhaps) more realistic surfaces, again in general agreement with the experimental observations. In ring regions perturbed by density and vertical waves induced by satellites orbital resonances, increased velocity dispersion of the carrier particles causes significant increase in the fraction of free debris particles. Observed X/S/Ka differential optical depth behavior in the A ring provides clear observational evidence of this behavior.

3.4 VERTICAL STRUCTURE AND MICROSTRUCTURE

Average vertical structure It is not surprising (in hindsight) that Galileo observed the rings to vanish when viewed edge-on (Pollack, 1975), because the rings have the aspect ratio of a sheet of paper a mile across. In the decades before spacecraft exploration, considerable effort was devoted to determining the ring thickness from residual edge-on ring brightness, but it is now clear that structural complications including the vertical extent of spiral bending waves (Section 3.5.1), and an inclined F ring (Section 3.5.6), preclude this approach.

The *true, local* vertical thickness H constrains the relative velocity between particles $c = H\Omega$, where Ω is the orbit frequency. H and the optical depth τ determine the volume density or filling fraction $D \sim \tau s/H$ (where s is a typical particle radius), and thus the interparticle spacing $l \sim (4\pi/3D)^{1/3}$. Their innumerable, constantly colliding particles give the rings the nature of a fluid, in which c, H, and τ define the collision frequencies and mean free paths, determining a local ring "pressure" and "viscosity" (Salo, 2012; Schmidt *et al.*, 2009; see also Chapter 16). The particle velocities are excited by collisions and gravitational impulses from large particles, but are damped by collisions with each other. Laboratory measurements of the elasticity of frost-covered ice particles have led to a nearly unanimous expectation that the particles flatten into a layer that is not more than a few of the largest particle sizes in thickness – maybe several tens of meters at most. Voyager radio occultations (Zebker *et al.*, 1985) tend to support this view. In regions where self-gravity dominates and *self-gravity wakes* form (see below), the wakes themselves act as locally massive objects, scattering smaller ring particles into somewhat thicker layers (Figure 3.3).

In addition to their importance for dynamical behavior, local vertical structure and especially the value of l/s are critical to all radiative transfer modeling of ring photometry, radar backscattering, etc. The long-known "opposition effect" of the rings is usually thought of as a nonlinear surge in reflected sunlight within a few degrees of opposition (zero phase angle). Classically this effect was explained by lit particle faces covering up their own shadows at phase angles that decrease with decreasing volume density. Interpreted in this way, the classical opposition effect implies volume densities on the order of 0.001 (Poulet *et al.*, 2002; French *et al.*, 2007b; Cuzzi *et al.*, 2009; Salo and French, 2010; Déau, 2012; Déau *et al.*, 2013; Déau, 2015). These low volume densities are the defining characteristic of the "classical" or many-particle-thick ring model, in which l, $H \gg s$; however, they are inconsistent with the dynamical expectations as well as with Zebker *et al.* (1985). In fact, recent work suggests that the very narrow classical opposition effect of the rings arises from coherent multiple scattering and interference within the granular material on the surface of individual particles, and has little to say about macroscopic vertical ring structure (French *et al.*, 2007b; Déau, 2015, and references therein).

However, Salo and French (2010) have shown that an *extended opposition effect*, affecting ring brightness out even to tens of degrees phase angle, depending on optical depth and ring opening angle, has broad implications for ring structure and particle albedo in realistic layers with a dense midplane

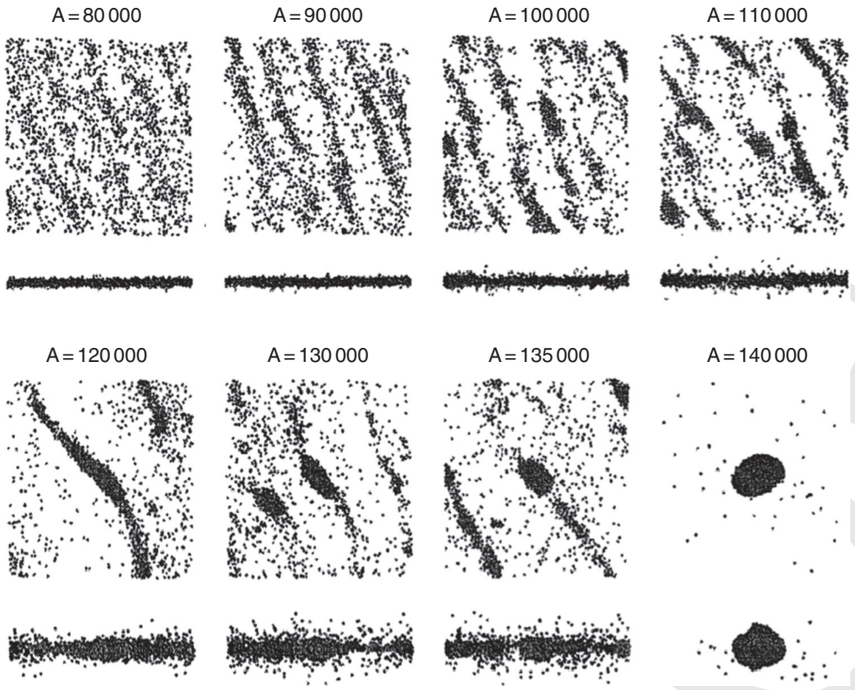

Figure 3.3 Numerical results showing self-gravity wakes at different distances from Saturn (A, km; for comparison, the outer edge of the A ring is at 136 780 km). Each of the eight panels shows both a view normal to the ring, and an edge-on view. As larger clumps form in the outer A ring, their stronger self gravity perturbs particles around them into a vertically thicker layer with higher relative velocities (see Chapter 16). Figure taken from Salo (1995); a movie of wake clumping and dispersal can be found in Cuzzi *et al.* (2010).

($D \sim 0.3$), a vertical decrease of particle density, *and* a moderately broad particle-size distribution, all of which are expected from dynamical models. In these conditions, shadow hiding is capable of producing a significant brightness increase relative to "classical" many-particle thick predictions over a wide range of backscattering geometries where the so-called "Chandrasekhar expression" for diffuse reflection I/F in lit or unlit face viewing,[1]

$$I/F_{\rm lit} = \frac{\varpi\, P(\alpha)\mu_o}{4(\mu_o+\mu)}\left[1-\exp\left(\frac{-\tau(\mu_o+\mu)}{\mu_o\mu}\right)\right], \qquad (3.5)$$

$$I/F_{\rm unlit} = \frac{\varpi\, P(\alpha)\mu_o}{4(\mu_o-\mu)}\left[\exp\left(\frac{-\tau}{\mu_o}\right)-\exp\left(\frac{-\tau}{\mu}\right)\right], \qquad (3.6)$$

which neglects multiple scattering, is usually regarded as remaining valid. In the above equation, ϖ is the particle single-scattering (or spherical) albedo, $P(\alpha)$ is the phase function at phase angle α, (μ_o, μ) are the cosines of the solar incidence and viewer emission angles from the ring normal (i, e) respectively.

Equation (3.5) is valid only for layers in which $l/s \gg 1$, which are *not* expected to characterize most of the A and B Rings (Salo and French, 2010; Cuzzi *et al.*, 2002). For typical groundbased or HST observations, nonclassical effects can increase the ring brightness by 20–80% (see e.g. Figure 7 of Salo and French, 2010), and even at phase angles of 90° or more, the effect can reach tens of percent for large τ and/or large ring opening angles; this effect should certainly be accounted for in interpreting groundbased and HST observations. The Monte Carlo models of Salo and French (2010) make certain approximations about the angular distribution of scattered photons that can and should be improved on in future models, and at present neglect nonaxisymmetric "wake" effects, but even these initial conclusions are extremely important for anyone attempting to infer the albedo and composition of ring particles from remote observations in these geometries (which include any Earth-based observations).

Essentially, Equation (3.5) underestimates the ensemble contributions of the ring layer in the above geometries, and thus leads to a significant overestimate of the the ring particle albedo from any observed I/F. Salo and French (2010) and Déau (2015) also show that the local particle size distribution (see Section 3.3) also affects the brightness correction. While competent Monte Carlo radiative transfer models (Porco *et al.*, 2008; Salo and French, 2010) are nontrivial to run, they are now approaching a fidelity which will allow us to infer the underlying properties not only of the local ring structure, but also of the composition of the ring particles (see Sections 3.7 and 3.11 for more discussion).

Other constraints on local ring structure are afforded by (a) future analysis of Cassini RSS occultations and bistatic scattering along the lines of Zebker *et al.* (1985), and (b) recent work on the thermal response of the rings to diurnal and seasonal variations in illumination (Flandes *et al.*, 2010; Ferrari and Reffet, 2013; Spilker *et al.*, 2013; Morishima *et al.*, 2016; Pilorz *et al.*, 2015; Reffet *et al.*, 2015). For a detailed discussion of the results and implications of thermal properties of the rings, which are subtle, we refer the reader to Chapter 15 in this volume.

Self-gravity wakes A pervasive, inhomogeneous granular structure, seen throughout at least the A and B rings, is caused by the constant tendency of local material to spontaneously clump together under its own self gravity, because the relative

[1] See Chandrasekhar (1960), Sections 13 and 52 (Equations 35). The version published in the Appendix of Cuzzi *et al.* (1984) has several typos: the demominators of Equations A2 are 4μ (wrong symbol typeset for θ) and S should not be primed; in Equations A3, a factor of ϖ was omitted and the denominator should read $(\mu' - \mu)$.

particle velocities are dampened by collisions. The properties of the structure are thus tied to the local surface mass density. In the time it takes each clump to collapse, radial Keplerian shear in the orbital velocities stretches it into irregular strands, systematically tilted to the local orbit direction. These *self-gravity wakes* were actually inferred decades before the arrival of Cassini, from telescopically observed nonaxisymmetric azimuthal brightness variation in the A ring where the effect is the most dramatic (Orton *et al.*, 2009). Figure 3.3 shows an early numerical model of how the effect varies with distance from Saturn (see Salo, 2012, for more recent discussion). More detailed physical discussion of self-gravity wakes and other forms of so-called "microstructure" (structure on the length-scale of the ring vertical thickness) can be found in Chapter 16 in this book. Time evolution of the structure can be seen in movie S1 in the supplementary material of Cuzzi *et al.* (2010).

Closer to the planet, Keplerian shear and tidal forces are stronger, so the wake structures are weaker and more aligned with the orbit direction (Colwell *et al.*, 2007; Nicholson and Hedman, 2010b). The wakes are strongest in the A ring because the disruptive tidal effects are smaller, allowing dense, long-lasting clumps to form more easily. This behavior is closely related to the long-known "Roche tidal stress" which prevents self-gravitating bodies from forming too close to a massive planet (Canup and Esposito, 1995). Beyond or near (depending on particle internal density) the outer edge of the A ring, stable clumps can persist indefinitely (the final panel is at 140 000 km).

This clumpy microstructure affects observations in several ways. The transparency of such a clumpy ring does not behave in the simple exponential fashion as the widely used slant path optical depth τ (Section 3.2; Colwell *et al.*, 2009), which must be used cautiously. In addition, these clumps and strands have a vertical thickness comparable to the ring vertical thickness H, which is comparable to the width of the gap between wake strands. Thus, depending on the azimuth angle at which they are viewed, the gaps are more or less visible, which leads to the long known nonaxisymmetric brightness of the A ring. The effect is less striking in the B ring both because of the smaller pitch angle of the wakes, and because of dilution due to the larger overall τ in most of the B ring (Colwell *et al.*, 2009). Clearly, photometry and thermal radiometry of the A and B rings must allow for this effect (French *et al.*, 2007a; Porco *et al.*, 2008, see also Chapter 15) and can even be used to constrain the local dynamical properties.

3.5 MAIN RING REGIONS

3.5.1 A Ring

The A ring is perhaps the best-understood part of Saturn's rings. Figure 3.4 shows its outer third, which contains the 300-km wide Encke Gap and the 30-km wide Keeler gap. The Encke Gap is seen to contain several narrow, "kinky" ringlets (Horányi *et al.*, 2009; Hedman *et al.*, 2013b), which are similar in several ways to the F ring strands (Section 3.5.6). The ringlet in the center of the gap shares the orbit of the largest (30 km diameter) embedded ring-moon Pan, but no other discrete objects have been found sharing the orbits of the several other azimuthally incomplete ringlets (at least three in all) seen in the gap (see Hahn, 2006, for a discussion). Generating the dust abundance seen in these ringlets has been found problematic by Sun *et al.* (2015b). The Keeler Gap, also, has been found to contain a smaller moon, Daphnis, in its center. These gaps are the only known examples where discrete moonlets are known to clear discrete gaps, in spite of several extensive, dedicated searches by Cassini of the similar-looking Cassini Division and C ring gaps (see Section 3.8 for more on ring-moons). The placid looking situation may be misleading though – Bromley and Kenyon (2013) believe that Daphnis is actually in somewhat of a precarious state, only marginally trapped in the Keeler gap and vulnerable to runaway migration right out of the A ring.

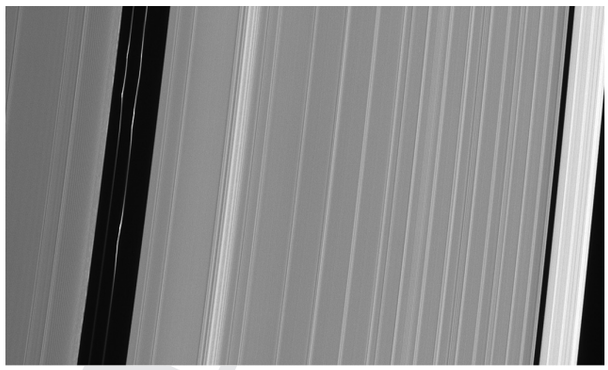

Figure 3.4 The outer A ring, with the 300km wide Encke Gap at the left, and the Keeler Gap and A ring outer edge at the right. Two clumpy, incomplete ringlets are seen in the Encke Gap. The bright bands are spiral density waves driven by small moons just outside the rings. A different view, and several striking movies of dynamical simulations of these ring edges, are found in Cuzzi *et al.* (2010). PIA18277; JPL and SSI.

The outer A ring is characteristically scored by dozens of regularly spaced, wavelike features whose locations align with known *orbital resonances* between local ring particles and one or another nearby ringmoons (Figure 3.4; see also Chapter 2). High-resolution images (Figure 3.5) and higher-resolution stellar and radio occultations have characterized these features in detail as tightly wrapped spiral density (radially compressing and expanding) and bending (vertically flapping) waves, excited at resonances and propagating away from them by virtue of the local self-gravity of the ring material.

The physics of spiral waves was perhaps the first, but is certainly not the only, example of how classical pressure and viscosity play a critical role, along with local gravity, in controlling ring structure, as if the countless ring particles represented molecules in a fluid (Goldreich and Tremaine, 1982; Section 3.4). The theory of spiral density (and bending) wave generation and propagation is quite mature for small wave amplitudes (Shu, 1984), but where the wave amplitude is comparable to the background (the nonlinear regime) it is less so (Shu *et al.*, 1985a). Moreover, the theory of how the wave amplitudes damp by viscosity and transfer momentum to their surroundings, while sophisticated, is not always in agreement with observations (Shu *et al.*, 1985b). Non-ideal effects such as the impenetrability of finite size particles, leading to vertical

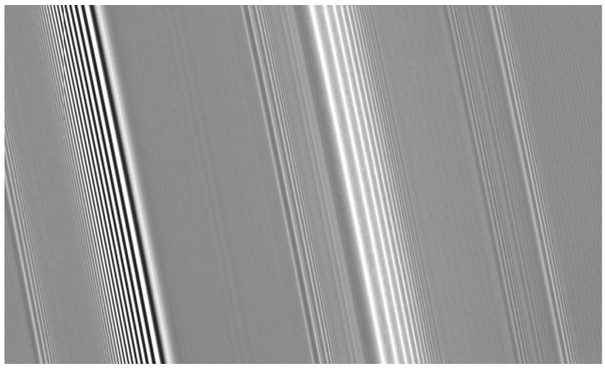

Figure 3.5 A closeup view of spiral density waves (which propagate towards their perturber (in this case Mimas, which is outwards or to the right) and one prominent spiral bending wave (left center), which propagates away from its perturber (also Mimas), in this case inwards or to the left. The bright crests in the density wave represent more compacted, optically thick material. The strong contrast in the bending wave in this viewing geometry is due to differential shading of light from the Sun, off to the right, striking the rolling, inclined surface of the rings at different angles. The longer wavelengths are tens of km and, for the bending wave, the vertical flapping has a peak-to-peak amplitude of 1.5 km (Shu *et al.*, 1983). PIA10501, JPL and SSI.

"splashing" in zones of high compression, have been treated only in a preliminary way (Borderies *et al.*, 1985; Schmidt *et al.*, 2009).

One critical aspect of the theory, which seems to remain valid in the nonlinear regime, is a direct relationship between radial wavelength and local surface mass density (Shu, 1984; Schmidt *et al.*, 2009). Since radial wavelengths are much longer than individual particle sizes or even the likely scales of large local clumps of particles (Section 3.4), density waves provide a robust measurement of the underlying surface mass density, which can be compared with observations of particle size and optical depth as a constraint on the internal density of individual particles. Figure 3.6 shows how thoroughly the surface mass density and viscosity of the A ring can be measured, because of the abundance of spiral waves there. A major surprise is that the surface mass density *decreases* inwards from 130 000 km and varies only smoothly across the *inner* edge of the A ring (Figure 3.6; Tiscareno *et al.*, 2013b), whereas the *optical depth* or integrated particle *area increases* inwards over the same radial range, and has a dramatic jump at 122 000 km (Figure 3.1). Somehow, the particle size distribution changes to allow this combination of effects. Viewed as surface mass density, it is hard to even say where the inner edge of the A ring is. The ratio of the local optical depth τ to the local surface mass density σ is called the *opacity* $\kappa = \tau/\sigma$, and will be remarked on subsequently. For a layer of identical particles with radius s and internal density ρ it is easy to show that $\kappa \approx 3/4\rho s$, decreasing with increasing particle size (see Section 3.3).

Spiral density waves have now been found in the C ring, apparently driven by structure in Saturn's own interior, with intriguing implications (Section 3.5.4).

Isolated resonances can control ring edges, depending on their strength and the viscosity of the underlying ring material (see Chapters 10 and 11). The outer edge of the A ring, seen at the far right side of Figure 3.4, is controlled by the Janus 7:6 Lindblad resonance (Spitale and Porco, 2009; El Moutamid *et al.*, 2016), and the inner edge of the Keeler Gap is controlled by the 32:31 resonance with Prometheus (Colwell *et al.*, 2009). A similar, but more complicated, situation allows the Mimas 2:1 resonance to control the outer B ring edge (Section 3.5.2). The diagnostic fingerprints of these resonances are seen in periodic azimuthal variations in the radial location of the edges that move with the angular speed of the moon responsible (see Chapter 2 for more details on resonance dynamics).

The densely compacted crests of spiral density waves produce another kind of microstructure (Figure 3.7). When driven

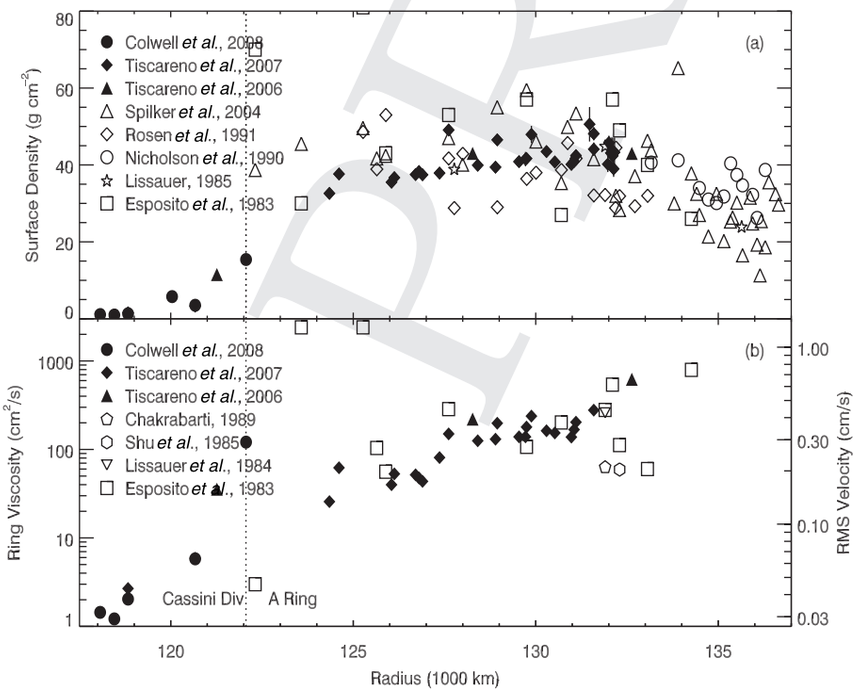

Figure 3.6 A collection of determinations of surface mass density from density wave wavelengths, and viscosity from wave damping lengths. Cassini results are shown in filled symbols, and Voyager results in open symbols. The vertical dotted line is the inner edge of the A ring (figure from Colwell *et al.*, 2009, where references are given).

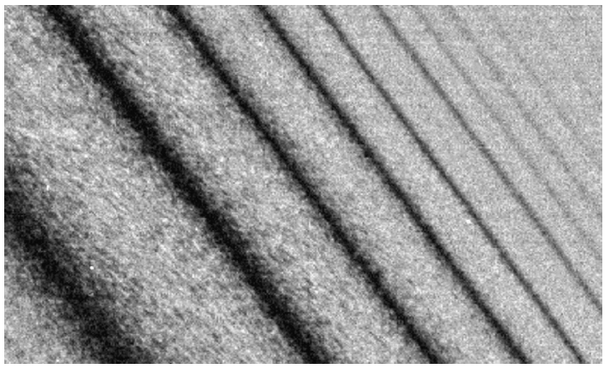

Figure 3.7 Very large trailing clumps of particles, dubbed "straw," apparently form when ring material is compressed in the dense crests of spiral density waves. This previously unpublished Cassini image was taken with sub-km resolution during Saturn Orbit Insertion on the unlit face of the rings, so dense material appears dark. Similar sized clumps *could* have been resolved beyond the first few crests, but are not seen; thus they are only formed in the first few crests, or are more quickly dissipated beyond them. For more discussion see Porco *et al.* (2005). Image PIA06096, NASA/JPL and SSI.

inexorably together in density wave crests (here appearing dark on the unilluminated face of the rings), particles get mashed together and remain stuck by surface forces (see also Chapter 17) even as the material passes out of the wave crest, leaving behind clumps the size of railroad trains (barely resolved in this image) which are ultimately dissipated and eroded by collisions; these huge clumps are informally known as "straw". Few images have as yet been obtained by Cassini capable of resolving "straw" (during Saturn Orbit Insertion; Porco *et al.*, 2005), so its broad radial distribution is unknown.

3.5.2 B Ring

The B ring is almost certainly the most massive of Saturn's main rings; as seen in Figure 3.2, the outer 2/3 of this ring is very densely filled. As discussed below however, the scarcity of spiral density waves in the B ring, especially in its densest regions, makes it hard to measure the surface mass density as thoroughly as in the A ring (Figure 3.6). The B ring is actually *full* of structure, but almost none of it is understood. Structure is observed in both ring brightness and/or color from images, and in optical depth variations from occultations. Even the degree of correlation between these different structural manifestations has not been studied.

Radial spatial scales range from a fairly well defined, semi-periodic 80 km in the inner, less opaque region from 92 000 to 99 000 km called B1 (see Colwell *et al.*, 2009, for nomenclature of the different regions) to typically larger radial scales of several hundred km in the more opaque regions B2, B3, and B4 outside 99 000 km (Horn and Cuzzi, 1996; Colwell *et al.*, 2009). It has been suggested that the typically 80 km B1 structure might be related to ballistic transport of meteoroid ejecta (Durisen *et al.*, 1992; Estrada *et al.*, 2015a; see also Chapter 9), but there is as yet no good explanation for the several hundred km scale structures in B2–B4. Within some of the broadest of the features in the most opaque region B3, one also sees bursts of km-scale structure (Horn and Cuzzi, 1996) even in Voyager images. At the boundary between region B1 and the more dense region B2, the visual-wavelength color of the rings also changes dramatically and starts to correlate very closely with underlying ring brightness, while the color in region B1 is uncorrelated with brightness and optical depth (Estrada *et al.*, 2003). In the outermost B ring the irregular structure is non-axisymmetric (Smith *et al.*, 1981), and Madhusudhanan *et al.* (2016) have suggested a kind of nonlinear behavior known as a Duffing oscillator for this structure.

Cassini images have not, as yet, been carefully analyzed in terms of B ring structure, but progress has been made using stellar and radio occultations. The occultations have revealed a number of 50-km wide "channels" of dramatically lower, but still substantial, optical depth, and with very sharp boundaries, carved out of the densest regions (Colwell *et al.*, 2009, 2010). Radio occultations (Thomson *et al.*, 2007; Colwell *et al.*, 2009) have also revealed widespread structure on the 100-m scale in regions B2 and B4, as well as in the inner A ring, which appears to be axisymmetric (is not canted to the orbit direction) but persists for only a fraction of a circumference. This behavior is reminiscent of the expectations for the so-called "overstabilities" (see Chapter 16).

Self-gravity wakes and surface mass density Even more ubiquitous and overlapping, nonaxisymmetric (canted) self-gravity wakes have been inferred throughout the B ring (as in the A ring) from stellar and radio occultations. Perhaps the most global evidence for this is the systematic deviation of the slant path optical depth from a simple $1/\sin B$ dependence for a uniform ring slab, where B is the opening angle of the ring. The observations are much better fit by a medium containing some area fraction of low-τ gaps separated by very dense clumps. Because all regions of the rings have been observed from a variety of opening angles and longitudes, models can even determine the relative height-to-width and separation-to-width properties of typical dense clumps, as well as their cant angle to the orbital direction (Colwell *et al.*, 2007). However, in the B ring, the "gaps" actually have moderate $\tau \sim 0.25$, even at the very highest spatial resolutions (Colwell *et al.*, 2007; Sremčević *et al.*, 2011a).

Based only on the observed ring optical depths, typical particle sizes from occultations, and plausible internal particle densities, the total main ring mass (dominated by the B ring mass) was estimated in Voyager-era studies as roughly the mass of Mimas (Esposito *et al.*, 1984; Cuzzi *et al.*, 1984). However, some recent arguments, based on model simulations, suggest that the small-scale clumping in self-gravity wakes leaves open the possibility that the true amount of mass in the B ring, hidden within opaque clumps, has been underestimated by as much as an order of magnitude (Robbins *et al.*, 2010). The surface mass density (and total mass) of the B ring is of special importance because only in the unplumbed depths of regions B2–B4 has it not been independently constrained (Figure 3.6). If the B ring indeed had a mass density an order of magnitude larger than simplistic estimates, the B ring may be able to resist meteoroid darkening and pollution for a duration comparable to the age of the solar system (Estrada *et al.*, 2015a, see also Chapter 9). For further discussion of ring age and evolution see Section 3.10 and Chapter 18.

The size of and separation between the dense self-gravity wake clumps mentioned above, roughly 100–200m, is itself a constraint on the local surface mass density (Schmidt *et al.*, 2009), and is roughly consistent with a simple scaling from ring optical depth as in the A ring where the surface mass density *has* been measured independently (Colwell *et al.*, 2006; Hedman *et al.*, 2007c), arguing against a significant underestimate of B ring surface mass density. Also, Estrada *et al.* (2015b) have shown that, since the A ring surface mass density is known, an arbitrary and coincidental age difference between the A and B rings would be needed to explain the very similar color and brightness of the A and B ring particles under meteoroid bombardment, if the B ring mass indeed *were* an order of magnitude larger than simplistic estimates. That is, the A ring must be young even if the B Ring is more massive than expected (Esposito, 1986). Moreover, Hedman and Nicholson (2015) have used new, sophisticated techniques to detect and analyze very weak spiral density waves in the most opaque regions of the B Ring, obtaining surface mass densities comparable to or even slightly lower than traditional, optical-depth-based estimates. Based on these recent results, Hedman and Nicholson (2015) estimate the total ring mass as comparable to that of Mimas. In some of the most eagerly anticipated observations of the Cassini "Grand Finale" orbits (see Chapter 19), the Radio Science team will measure the ring mass directly, from gravitational perturbations to the spacecraft's orbit, and settle this question definitively.

The floppy outer B Ring edge The closely spaced Voyager flybys provided a snapshot in time of the B ring outer edge, and found it to be well fit by an $m = 2$ pattern rotating with the mean motion of Mimas, as expected from its proximity to the Mimas 2:1 inner Lindblad resonance (Porco *et al.*, 1984).[2] However, Cassini observations over longer time baselines found the situation to be considerably more complicated. French *et al.* (2010) showed from a combination of stellar and radio occultations that the $m = 2$ pattern was, at best, weaker and shifted from the predictions of the Voyager-era model. Hedman *et al.* (2010b), also based on occultation data, suggested that the $m = 2$ pattern was librating about some mean longitude rather than tracking Mimas. Spitale and Porco (2010) finally showed that the instantaneous shape of the B ring edge was actually a superposition of at least four independent modes: a forced $m = 2$ mode tracking Mimas, as originally suggested, plus "free" modes at $m =$ 1, 2, and 3 as well, perhaps spontaneously arising from internal viscous and/or pressure forces, each having a different angular rate. They showed that constructive and destructive interference between these independent modes leads to a B ring edge where the expected $m = 2$ angular radial displacement pattern appears and disappears with a roughly five-year period (see also Esposito *et al.*, 2012). Hahn and Spitale (2013) suggested that these disturbances might have arisen from impacts even hundreds of years ago. Most recently, Nicholson *et al.* (2014b) showed that the dominant forced $m = 2$ mode never really vanishes, but is only periodically weakened by these cancellations, and determined improved angular rates for all modes. Their results support the suggestion of Spitale and Porco (2010) that the free modes are radially propagating waves that are amplified into a kind of standing wave by trapping between the Mimas 2:1 resonance and the sharp outer B ring edge. However, they noted that residuals of their final model remain larger than really satisfactory, suggesting that yet more dynamics may be in operation in this interesting region.

[2] In this paper m, the azimuthal wavenumber of a resonance, represents the number of lobes in the disturbance as seen in the frame rotating with the perturber, or the number of arms in any associated spiral density wave (Murray and Dermott, 1999; see also Chapter 2).

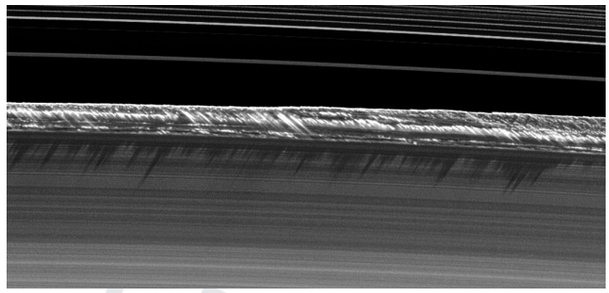

Figure 3.8 Image of the outer B ring edge taken very near to equinox. Note the highly disturbed and irregular structure at the very outer edge of the B ring, which includes both radial excursions at the edge, and vertical "splashing" of material into sharp peaks that cast shadows on the face of the B ring behind (Sun is at the top). The inner Cassini Division, including the narrow Huygens ringlet, is at the top of the image. Image PIA 11668; courtesy NASA/JPL and SSI, see also Spitale and Porco (2010).

Amongst the complications known to exist at or near the B ring outer edge are dramatic vertical "splashing" structures seen by virtue of their vertical structure in images taken near equinox (Figure 3.8) and a number of apparently isolated, Keplerian objects not seen directly but manifested in local disturbances at the edge (Spitale and Porco, 2010; Spitale and Hahn, 2016). Esposito *et al.* (2012) suggested that large objects are preferentially *created* in regions of strong streamline compression, such as at the outer B ring edge, and such objects can be responsible for some vertical disturbances (see Section 3.8 and Chapter 8 for more discussion).

"Spokes": evanescent dusty clouds on the face of the B ring Long before encounter, both Voyager spacecraft observed irregular, shadowy features which sporadically crossed the face of the B ring; these structures became brighter than their surroundings at high phase angles, making it immediately obvious that they were delineated by wavelength-sized particles and implicating electromagnetic effects in their creation (Mendis *et al.*, 1984; Doyle and Grün, 1990; Grün *et al.*, 1992). The nature of the process involved, and its possible dependence on ring opening angle to the Sun and/or Earth, were debated over the succeeding years into the Cassini era (Nitter *et al.*, 1998; McGhee *et al.*, 2005; Mitchell *et al.*, 2006). In the end it seems that seasonally varying solar photocharging of the ring layer, its "atmosphere", and the tiny grains levitated from the ring, accounts for the fact that spokes are primarily visible at low solar elevation angles; for recent reviews see Horányi *et al.* (2009) and Chapter 12.

More recently, D'Aversa *et al.* (2010) provided improved models of spoke particle sizes, based on Cassini VIMS observations from visual to near-IR wavelengths. They find a pure water ice composition for the spoke grains, but the high contrast in the 1–2.5 μm spectral range cannot be provided by only the ∼0.6 μm radius grains previously inferred (McGhee *et al.*,

2005). By modeling VIMS-VIS and near IR reflectance spectra, D'Aversa *et al.* (2010) obtained a modal radius of about 1.9 μm (area weighted $s_{\rm eff} = 3.5 \pm 0.3$ μm), and a number density of about 0.01–0.1 cm^{-3}. If generally applicable beyond the single spoke observed, the unexpected abundance of relatively large grains in the spoke has implications for spoke formation models, since the energy requirement to sustain the process increases by at least an order of magnitude. Mitchell *et al.* (2013) mapped the shapes and morphology of evolving spokes. They found that spokes grow quickly in radial extent, and are constantly evolving in intensity. They found evidence for the Saturn Kilometric Radiation (SKR) period (an auroral property) but no evidence for a Saturn Electrostatic Discharge (SED) period (an equatorial thunderstorm property). The fundamental underlying process by which spokes are triggered remains somewhat of a mystery, however (see also Chapter 14 in this volume).

3.5.3 Cassini Division

The Cassini Division (CD) separates the A and B rings (Figure 3.1); yet its properties are in nearly all ways a better match to those of the C ring (Section 3.5.4). Structurally it is composed of broad, low-τ bands separated by empty gaps, some of which contain narrow ringlets (Colwell *et al.*, 2009). Particles are also more similar in albedo, spectra, and plausibly composition to those in the C ring, being generally darker and less dominated by water ice than the A and B ring particles (Section 3.7 of this chapter, and Cuzzi *et al.*, 2009). The overall morphology of the outer CD is especially similar to the outer edge of the C Ring, consisting in both cases of a broad, nearly featureless "ramp" or nearly linear increase in $\tau(r)$, in which the *particle properties* slowly change as if material is drifting inwards from larger radii r (Cooke, 1991; Cooke *et al.*, 1991; Cuzzi and Estrada, 1998). *In general*, the outer regions of both the CD and C ring seem to correspond to the predictions of ring evolution under meteoroid bombardment and ballistic transport of ejecta, with associated radial drift, even while important puzzles remain regarding the specifics of the structure and the parameter values needed for the models to match the observations (Durisen *et al.*, 1992; Cuzzi and Estrada, 1998; Charnoz *et al.*, 2009; Estrada *et al.*, 2015a; see also Section 3.10 and Chapter 9 for more discussion).

One interesting difference between the CD ramp and the C ring ramp is a long-wavelength, periodic brightness pattern in the CD ramp, first identified in Voyager data as a spiral density wave due to Iapetus (Cuzzi *et al.*, 1981). However, the feature, while easily visible to the crude Voyager cameras, never reappeared in Cassini data until the low sun elevation angles of the Voyager geometry recurred during the equinox time period, and the feature was identified by Tiscareno *et al.* (2013b) as an Iapetus spiral *bending* wave analogous to a Titan wave first identified in the C ring by Rosen and Lissauer (1988). The CD ramp Iapetus wave propagates right across the A ring inner boundary, and reveals no significant discontinuity in surface mass density there, in spite of the significant step in τ which defines the boundary (see Figure 3.6).

It has long been known that the B ring outer edge is defined by the strong Mimas 2:1 inner Lindblad resonance. Just as the Colorado river was surely more powerful when the glaciers were melting, the full Cassini Division may have been carved out from a more massive, more viscous, newly-born ring by a powerful Mimas 2:1 spiral density wave that was, at the time, able to propagate across the 1400 km width of the current Cassini Division, carrying negative angular momentum and dredging material inwards until the residual viscosity was so low that gaps started to open, as seen today (see Section 3.5.4).

The innermost gap in the CD, just outside the B ring edge, contains the narrow, optically thick Huygens ringlet (Figure 3.8), whose presence is largely unexplained. Spitale and Hahn (2016) have shown that, like the nearby B ring outer edge, its structure results from an overlap of several dynamical modes. The primary mode is the "Keplerian ellipse" mode $m = 1$ (Porco *et al.*, 1984) but there are different combinations of forced and free $m = 2$ modes evident on the inner and outer edges of the ringlet. Moreover, Spitale and Hahn (2016) see disturbances attributable to several long-lived objects on Keplerian orbits, obscured within the ring material near the inner edge of the ring, reminiscent of the B ring outer edge (Section 3.5.2).

The missing moonlets Perhaps the most significant new result regarding the CD is a negative one: the *lack* of moonlets found orbiting within, and clearing, the eight regularly spaced gaps in the CD. The great success of this concept in the A ring (Pan and Daphnis; Section 3.5.1) makes this negative result surprising.

An extensive, but non-optimal, search was conducted by Voyager 2 (Smith *et al.*, 1982), which concluded that icy moonlets in the CD gaps larger than 6km diameter could be ruled out. From torque balance arguments applied to a mix of density waves and gaps observed in the C ring, Rosen *et al.* (1991) concluded that the C ring viscosity was in the range 10^{-4} to 10^{-2} cm^2/s. Torque scales with the mass of the responsible moonlet such that, in torque balance, the required moonlet radius is only weakly dependent on viscosity as $\nu^{1/6}$. Adopting the Rosen *et al.* (1991) viscosity range, we find that the tens-to-100-km wide CD gaps could be cleared by icy moonlets of perhaps 1 km radius.

A considerable amount of Cassini imaging was devoted to searching the CD at high resolution, in order to set definitive limits on the presence or absence of moonlets that are large enough to keep the observed gaps clear. Unfortunately, those designated searches never quite managed to cover the *full range of corotating longitudes* (C. Porco and J. Weiss, personal communication, 2014), so there is some chance that km-size moonlets might have been missed. Recalling that Pan was discovered in images where its diameter subtended 1/2–1/3 pixel (Showalter, 1991) *and* that the mean motion and even rough longitude of Pan was *already known* from its influence on the Encke Gap edges, and realizing the difficulty of covering the entire circumference of the CD at a resolution of only 2–3 km, which requires geometries which change rapidly, this situation is not hard to understand.

Since there are eight gaps, the probability that appropriate size moonlets would have been missed in *all* CD gaps seems small if they are really there (J. Spitale, personal communication, 2016). On the other hand, Cassini witnessed the birth in 2006 of a very dusty "charming" ringlet near the middle of the outer CD gap, which has persisted to the time of this writing.

Hedman *et al.* (2010c) have found that the ringlet behaves as if it is entirely composed of 10–100μm sized dust grains; this rapid appearance of so much dust suggests some impact or collision involving pre-existing sources at that auspicious location.

Meanwhile, other work hints at unexplained regularities between the CD gap edge locations which may suggest confinement mechanisms not requiring local moonlets. Hedman *et al.* (2010b) analyzed many stellar occultations of the CD. They found that the inner edges of six gaps (outer edges of ring structures) were noncircular, having modes with pattern speeds that followed a regular progression. They found that the speeds of the patterns on the gap inner edges could be expressed as a regular combination of the precession speed at the B ring edge, and integer multiples of a libration frequency which they claimed to see for the B ring $m = 2$ pattern, relative to Mimas. They thus suggested that the CD gaps were somehow maintained by resonances involving a librating $m = 2$ pattern at the B ring edge. However, Spitale and Porco (2010) found that the B ring edge was not librating at any regular frequency, but responding to cancellation of modes with different pattern speeds (Section 3.5.2). Nicholson *et al.* (2014a) use a much larger data set to confirm the peculiar relationships found by Hedman *et al.* (2010b); they admit that the lack of a well-defined B Ring edge libration frequency casts their original proposal into some doubt, but the observation remains, suggesting there may indeed be physical mechanisms for creating these gaps that does not require a moonlet for each one (recall the viscosity may be extremely low).

3.5.4 C Ring

The C ring is the innermost "main" or classical ring of Saturn. Its structure appears simple compared to the record-grooved B ring, but in fact very little of it is understood. The so-called "plateau" features in the outer C ring, and the Maxwell and Titan gaps (and narrow eccentric ringlets they contain), are perhaps its most notable features (see Figure 3.9). At the very outer edge of the C ring the optical depth shows a nearly linear "ramp" up to the inner B ring edge, in a fashion that mirrors the ramp structure in the Cassini Division, just inside the inner A ring edge (Section 3.5.3). The middle of the C Ring is generally bland except for a subtle, long-wavelength undulation in optical depth in the 78 000 to 87 000 km range (Figure 3.1) which is also manifested in spectral properties (Figure 3.15). The C ring contains a handful of spiral density waves, constraining its local mass density (see Section 3.5.1) and leading to interesting implications (see below). The creation of an empty gap containing a ringlet at a resonance with Titan, instead of the more typical spiral density wave, can be explained in terms of the inability of the underlying ring viscosity to transport material at a rate required by the resonant torque; the value of torque separating gap-features and wave-features with known causes provides a constraint on the poorly understood ring viscosity (Colwell *et al.*, 2009; Schmidt *et al.*, 2009). All this structure is discussed in some detail by Colwell *et al.* (2009); below we focus on several important results which have emerged more recently.

Impacts create ripples on the rings A hint of the occasionally violent life of the rings was uncovered by Hedman *et al.* (2011a). In Cassini images obtained near equinox at very low sun angles, a weak vertical ripple was detected running through the D and C rings, with wavelength systematically decreasing outwards. A similar structure had just been identified in Jupiter's faint ring (Showalter *et al.*, 2011). These ripples were explained in both cases by a somewhat extended "sandblasting impact" of the inner part of the ring system by an inclined stream of rubble from a tidally disrupted object, tilting the rings locally out of the equator plane. The systematic radial wavelength variation is a result of differential regression of the nodes of the inclined orbits of ring material. Two ring impacts can even be resolved in 1983, spaced by months (Hedman *et al.*, 2011a), and another one identified for 2011 (and maybe also 1979; Hedman and Showalter, 2016). Moreover, Marouf *et al.* (2011a) identified, in much higher-resolution Cassini RSS occultations, two other similar ripples of much shorter wavelength. The short wavelength implies they are much older – occurring 50 years apart more than 600 years ago.

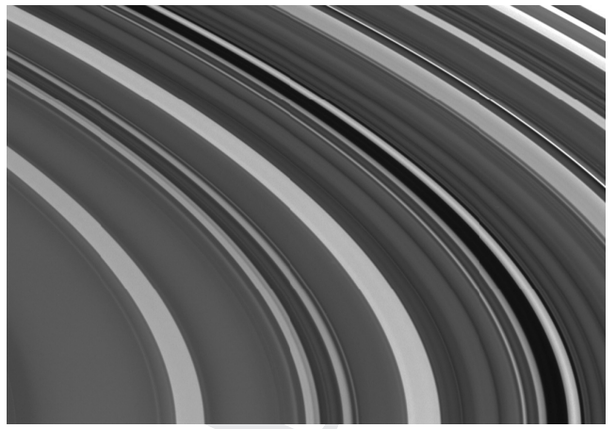

Figure 3.9 The outer C ring, showing the region of the "plateaus" (broad bright features surrounded by grey, lower optical depth material) and the narrower, eccentric Maxwell ringlet (the outermost bright feature crossing the lower border of the frame, and here lying near the outer edge of its gap). The plateaus are typically 200–300 km across (see also Figures 3.1 and 3.2). Cassini image PIA06540, courtesy NASA/JPL and SSI.

Ring-planet interactions in the Maxwell/Plateau region The Maxwell ringlet itself (Figure 3.9) has been studied somewhat inconclusively for decades (see Colwell *et al.*, 2009, for a review); unlike the Titan ringlet and gap, no clear dynamical cause has been found – until recently. Marley and Porco (1993) first suggested that internal modes within Saturn might have the proper amplitude and angular propagation speed, on top of the planet's rotation itself, to generate *outer* Lindblad (or even vertical) resonances capable of driving ring structure, just as the gravitational perturbations of tiny moons can drive visible structure at resonances in the rings (Murray and Dermott, 1999; see also Chapter 2). Uncertainties in the planet's internal structure precluded convincing direct identifications, but it was intriguing that the strongest (2:1) resonance of the predicted modes was in the general vicinity of the Maxwell Gap – itself the most significant unassigned dynamical feature in the C ring.

Hedman and Nicholson (2013, 2014) recently analyzed 14 previously known but unidentified waves in the C ring, most

of which had unusual inward propagation directions (Rosen *et al.*, 1991; Baillié *et al.*, 2011) and found them most easily explained by outer Lindblad resonances with $m = 2 - 9$ or larger, consistent with the general idea of Marley and Porco (1993). New models of Saturn's interior have been developed by Fuller (2014, 2015), which include vertically stable stratification of regions near the core, and which move the $m = 2$ outer Lindblad resonance from the original prediction of Marley and Porco (1993) into very good agreement with the Maxwell Gap location. Most recently, French *et al.* (2016) have identified the signature of an $m = 2$ outer Lindblad resonance *in the Maxwell ringlet itself*. The combination of these recent results is very compelling evidence that the mystery of the Maxwell Gap and ringlet has been resolved, and offers the hope that the more than a dozen other planet-generated waves will tell us even more about the interior structure of Saturn (Marley, 2014).

To speculate a little along these lines, the "plateaus" are nearly symmetrically distributed about the Maxwell gap, almost certainly not a coincidence but as yet unexplained. Models of restructuring by ballistic transport associated with meteoroid bombardment present intriguing possibilities in terms of how their sharp edges may be preserved (Estrada *et al.*, 2015a, and Section 3.10 and Chapter 9), but are not yet completely successful, and do not point to a radial pattern of features such as we see. Perhaps some fine structure or sidebands of the strong $m = 2$ resonance will yet be found to help explain how these unique features are created. Hedman and Nicholson (2013, 2014) find that the surface mass densities σ in the plateaus show little or no difference from their lower-τ surroundings – that is, only their opacity $\kappa = \tau/\sigma$ is elevated, normally a sign of more abundant small particles (see Section 3.3).

Buried centaur? The definitive identification of m for 14 planet-generated spiral waves in the C ring (Hedman and Nicholson, 2013, 2014) allows the local surface mass density σ to be determined unambiguously and with more radial coverage than previously. Combined with the local τ, a surprising opacity profile ($\kappa = \tau/\sigma$) is seen, with a broad dip between 79 000 and 86 000 km in the mid-C ring to values comparable to those seen in the A ring (Section 3.5.1) and much smaller than the opacity inferred for the inner and outer C ring (Baillié *et al.*, 2011) but consistent with the opacity determined by Hedman *et al.* (2011a) in the mid-C ring. Given constant composition and particle density, opacity variations only arise from variations in the local particle size, but neither RSS occultations (Section 3.3) nor statistical fluctuations in stellar occultation intensity (Showalter and Nicholson, 1990) show any evidence for a bump in particle size over this range of radii in the mid-C ring. C ring particles tend to be systematically smaller than A ring particles, consistent in size with the particles in the relatively *high* opacitiy inner and outer C ring regions.

However, it has been found by Zhang *et al.* (2017), from analyses of ring thermal emission at 2 cm wavelength using the Cassini Radar system as a radio telescope, that the middle C ring is extensively and uniquely polluted by nonicy material – most likely silicates – to much higher levels than the surrounding C ring. Zhang *et al.* (2017) suggest this is the result of some incoming, primarily rocky, centaur becoming tidally disrupted to rubble some 20–30 Myr ago, with the debris subsequently spreading radially within the mid-C ring (see Section 3.7 for more discussion). The evidence for 3–4 smaller ring impacts over the past several hundred years (the ripples discussed above) gives this suggestion some credibility. It would be plausible in that scenario for the centaur's rubble to remain in sizeable chunks of more or less solid silicate and become admixed with and covered by the native, primordial icy C ring material over time. Even if spectrally hidden, the buried silicate chunks could increase the surface mass density in a way that is consistent with the opacity "dip" in the mid-C ring (Hedman and Nicholson, 2014; Zhang *et al.*, 2017).

3.5.5 D Ring

The D ring is a faint, very low τ region lying just inside the C ring (for reviews see Horányi *et al.*, 2009, and Chapter 12). It was discovered by Voyager and is most visible at high phase angle, by virtue of its "dust"-size particle component. It consists of a handful of ringlets spread across a smooth, diffuse background, extending inwards to 67 000 km or so. It is generally believed to be delineated by an unseen, underlying belt or belts of macrocopic objects, like the G ring, Jovian ring, and Neptune ring as well as much of the structure in the Uranian ring system. The color and albedo of the D ring particles are not known.

Unremarkable as it may look, the D ring records remarkable events occurring on human timeframes. A bright ringlet seen by Voyager at 67 650 km, called D68, has been found to be eccentric, precessing, and longitudinally variable in brightness (Hedman *et al.*, 2014), with structure moving at the local orbital speed; so far, this is reminiscent of the G ring and Aegaeon, suggesting a small local moonlet underlies the feature. However, Hedman *et al.* (2014) dismiss this explanation, primarily on the grounds of not finding a moonlet in the obvious place. Instead, they discuss a variety of more complicated scenarios to confine a dusty ring, including plasma drag and corotation resonances with various moons or planetary interior structure; none of these are clearly preferable, and the situation remains unresolved. A novel peculiarity and potentially larger problem is that the semi-major axis of D68 meanders around by several km, on a decadal timeframe. The sparse observations do not obviously favor a smooth variation of semi-major axis over a jumpy one, and perhaps there is a moonlet there after all, undetectable because of a much lower albedo than expected.

One kind of time-variable structure in the D ring seems easier to interpret: wrapped spiral vertical corrugations of the same type (indeed due to the same event) as observed in the C ring (Section 3.5.4), caused by differential precession of a locally tilted and/or eccentric ring, are probably caused by a "distributed" impact by a trail of rubble from a disrupted interloper. These structures have very characteristic radial wavelength variations that allow the perturbing event to be dated fairly precisely. The D and C rings seem to have been sandblasted multiple times in the last few decades, once in 1979 (causing a pattern seen by Voyager but not Cassini), two closely spaced events in 1983 (only one of which is manifested in the C ring), and once in December 2011 (Hedman *et al.*, 2007a, 2011a, 2015; Hedman and Showalter, 2016). The responsible impactors would need to be a few km in diameter, assuming fairly complete conversion to rubble (Hyodo and Ohtsuki,

2014). In the meantime, the jovian ring was similarly disturbed by an event associated with comet S/L9 (Showalter *et al.*, 2011). Recalling that RSS occultations reveal even smaller-scale ripples pointing to impacts from centuries ago (see Section 3.5.4), we begin to sense the pulse of interplanetary bombardment by sizeable comets or centaurs, in human-scale terms.

3.5.6 F Ring

The so-called "F ring" was discovered by the Pioneer 11 spacecraft (Gehrels *et al.*, 1980; van Allen, 1982), and its odd, "kinky," and stranded nature was revealed by Voyager imaging (Smith *et al.*, 1981). A chapter of this volume is devoted to the F ring (see Chapter 13), so here we will provide only an overview of recent work, building on the review by Colwell *et al.* (2009). In this section we focus on F ring structure, and discuss the composition of the F ring material, and its nearby moonlets, in Sections 3.7 and 3.8.

What sets the F ring apart from other components of Saturn's rings is its pervasive and ongoing dynamical interactions with its nearby ringmoons Prometheus and (perhaps) Pandora (Figure 3.10). In the Voyager era, it was thought that the narrow F ring was confined or "shepherded" by a balance of torques due to Prometheus and Pandora, which became known as the "shepherding satellites." However, over the years, the angular momentum transport process generically known as shepherding has been shown to be multifacteted; for more discussion of its subtleties see Chapters 10 and 11 in this volume. In the case of the F ring in particular, it was realized shortly after its discovery that it is *not* in torque balance between Prometheus and Pandora (Showalter and Burns, 1982), and more recently that the primary influence of Prometheus and Pandora on the entire region is to stir particles into chaotic orbits rather than to confine them (Winter *et al.*, 2007, 2010; Cuzzi *et al.*, 2014a), leaving an explanation for the 35-year-stability of the narrow F ring core elusive. We will discuss recent developments on this issue in more detail, after describing the overall properties of the ring.

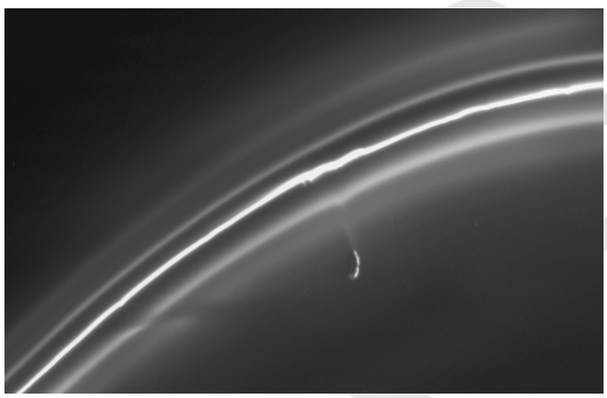

Figure 3.10 Image of the multi-stranded F ring and the nearby 135-km (long axis) ring-moon Prometheus, having a close encounter with the ring. The main core is the brightest, central ringlet, which has maintained a stable, precessing Keplerian orbit for over three decades. The outlying fainter strands are transitory features, resulting from the wrapping up into tight spirals of large jets of ejecta created by rare, sizeable objects (still much smaller than Prometheus) crashing through the F Ring core (Charnoz *et al.*, 2005). The faint, nearly horizontal feature crossing the strands at bottom left is a "gore" created by Prometheus perturbations on a prior close encounter with this patch of material (Murray *et al.*, 2008, see also Chapter 13). Image PIA 06143; courtesy NASA/JPL and SSI.

The *core* of the F ring is its most persistent feature; it is most visible in images at high phase angles because of its substantial component of fine dust grains (see Figure 3.12, Section 3.7, and Chapter 13). As seen in Figure 3.10, the main core is surrounded on both sides by fainter strands of variable number and radial separation. The outlying strands result from wrapping up into kinematic spirals, and ultimate dispersal, of large "jets" of material occasionally ejected from the core by vigorous, but infrequent, collisions with poorly understood objects on core-crossing orbits such as the 5-km-diameter object called S/2004S6, henceforth simply 2004S6 (Charnoz *et al.*, 2005; Murray *et al.*, 2008; Charnoz, 2009; Colwell *et al.*, 2009). The radial width covered by these outlying jets or strands, and the diffuse sheet they merge into, is perhaps as much as 1000km overall. The extent of the diffuse sheet is probably related to the orbits of the small moonlets that create the material in the first place, and radially limited by sweepup onto the surfaces of Prometheus and Pandora. It is probably these unusually large and temporally variable collisional events which lead to the complicated nonaxisymmetric brightness variations the F Ring exhibits over time in global, low resolution observations (McGhee *et al.*, 2001; French *et al.*, 2012, 2014).

The most obvious structures seen in and around the core and its outlying strands – time and longitudinally variable gores, channels, and radial spikes of various kinds – are due to gravitational perturbations by Prometheus, with the less massive and more remote Pandora playing a negligible role (Murray *et al.*, 2008; Colwell *et al.*, 2009, see figure 3.10). Image mosaics of the F ring reveal that the entire circumference is covered with irregular, spiky-looking radial perturbations of tens of km extent, which have the rough angular scale associated with close encounters with Prometheus (Murray *et al.*, 2008; Colwell *et al.*, 2009, see also Chapter 13). It is thought that most of these excursions are eccentricity-related rather than semi-major axis related (Chapter 13; see, however, below).

The core and strands have also been extensively observed in stellar occultations at visual wavelengths (Albers *et al.*, 2012; Meinke *et al.*, 2012), which indicate a *local* optical depth of several tenths over a radial width of several tens of km. Occultations also routinely detect rare, more opaque clumps on smaller lengthscales, some of which looking like essentially solid clumps hundreds of meters across.

The ubiquity and magnitude (typically tens of km) of significant local radial perturbations makes it difficult to obtain a completely satisfactory fit to any single Keplerian orbit, but to within the variance expected from the local disturbances, the visible F ring core *overall* has been fit independently using images and occultations at visual wavelengths, to a freely precessing Keplerian ellipse with semi-major axis of approximately 140221 ± 1 km (Bosh *et al.*, 2002; Albers *et al.*, 2012; Cooper *et al.*, 2013); these fits cover a > 30 year time period starting with the Voyager encounter, but they differ from each other by more than the stated formal errors. The inclination and node of the dominant F Ring core are similarly well behaved (Bosh *et al.*, 2002; Scharringhausen and Nicholson, 2013).

Occultations by the Cassini Radio Science (RSS) experiment provide an independent window on the structure and particle properties in the F ring. Because of the longer wavelengths involved (2–13 cm), the RSS occultations are sensitive primarily to cm-size and larger particles. Thus they see right through the micron-sized dust that dominates images and stellar occultations of the F ring, to reveal what is probably the "true core" of the F ring – the material making up nearly all of the underlying mass. A series of 23 RSS occultations taken over the 10 years since encounter shows the true core is extremely narrow – a mere 100 m in local radial extent. Moreover, the true core is only detected about 1/3 of the time, indicating that it is azimuthally incomplete (Marouf *et al.*, 2010a,b). An independent orbital solution can be obtained for the F ring's true core from RSS detections only; it is quite close to the value obtained from stellar occultations and imaging, but again, differs by more than the mutual formal error.

Some repeated patterns *within* the fine scale structure that permeates the F ring core (Murray *et al.*, 2008; Colwell *et al.*, 2009) imply the presence of numerous sub-km embedded objects, with small relative eccentricity and semi-major axis. The so-called "fans" seen by Beurle *et al.* (2010) generally appear right after a passage by Prometheus, suggesting that streamline compression may lead to the local formation of a temporarily coherent object capable of disturbing nearby material. The "minijets" seen by Attree *et al.* (2012, 2014) imply physical collisions at relative velocities of $\sim$1 m/s, typical for objects separated by $\sim$20 km in semi-major axis; that is, these objects lie mostly within or on the periphery of the dusty F ring core itself. The $10 - 10^4$ minijet-causing objects inferred by Attree *et al.* (2012, 2014) are thus quite distinct from the larger and less common 2004S6-type objects responsible for the large jets and kinematic spiral strands, which have semi-major axis differences of hundreds of km relative to the F Ring (Porco *et al.*, 2005) and encounter the core with relative velocity differences of 75-100m/s (Charnoz *et al.*, 2005; Murray *et al.*, 2008).

Why is the F ring core stable? Recent work suggests a new, rather more complicated role for Prometheus than generally believed. Prometheus and Pandora are themselves on formally "chaotic" orbits due to a weak, high-order mutual resonance (French *et al.*, 2003; Goldreich and Rappaport, 2003; Farmer and Goldreich, 2006), but their "chaos" manifests as very small, well-separated jumps in otherwise well-behaved mean motion. More importantly, because of the proximity of Prometheus to the F ring and the large mutual eccentricity of the system (Showalter and Burns, 1982), repeated encounters generate significant and unpredictable semi-major axis perturbations for objects in initial F-ring-like orbits. The orbits of these objects quickly become highly chaotic (Winter *et al.*, 2007, 2010; Cuzzi *et al.*, 2014a). Figure 3.11 shows that test particles initialized with the F ring's orbit are scattered chaotically over a range of $\sim$100 km in semi-major axis over only 20 years or so. This evolution may be the provenance of objects like 2004S6.

Meanwhile, Cuzzi *et al.* (2014a) also showed that certain very narrow locations, *slightly separated from* first-order resonances with Prometheus, permitted stable Keplerian orbits over long times in the face of this pervasive chaos. They explained these narrow stable regions using a kinematical effect they called "antiresonance." The effect allows prompt cancellation of weak semi-major axis perturbations on successive Prometheus encounters, before they have a chance to grow into the chaotic evolution of Figure 3.11, and arises only in regions where orbit precession is fast and synodic encounter times are long – conditions found only in the F ring region. Indeed the F ring core lies in one of these stable antiresonances, to within the uncertainty of the orbit determinations.

However, the effect described by Cuzzi *et al.* (2014a) does not completely solve the stability problem. There are numerous antiresonance radii that appear to offer stability, but only one F ring. More seriously, the sites are only *meta*stable in the sense that the requirement of weak perturbations is violated for any particles that encounter Prometheus near its apoapse, especially during times of apse antialignment. These encounters result in semi-major axis perturbations of 20 km (Showalter and Burns, 1982; Beurle *et al.*, 2010); such large jumps in semi-major axis cannot be canceled on a subsequent encounter and result in chaotic evolutions such as seen in Figure 3.11.

A missing element of this picture was suggested by Cuzzi *et al.* (2014b), and is currently in preparation for publication. The key clue came from the RSS occultation results, which as noted earlier show an azimuthally incomplete (and extremely narrow – 100 m wide) ring of cm–dm-size particles underlying the visible, dusty F ring. Cuzzi *et al.* (2014b) argued that the need for stable particles to avoid encountering Prometheus at its aopapse would be satisfied if they lay in a co-rotational resonance with Prometheus. They tested the hypothesis by regressing the set of 24 RSS (and Voyager) detections and 43 nondetections to a common epoch using a comb of orbit periods, and found that the regression leads to separated angular clusters at sites that avoid Prometheus encounter at apoapse if the core's orbit satisfies the m=110 first-order co-rotation–eccentric resonance with Prometheus. Cuzzi *et al.* (2014b) suggest it is not a coincidence that the observed F ring core occupies the *only location in the entire region* where an antiresonance lies on top of a co-rotational resonance, and believe that the combination of both effects is necessary and sufficient to explain the long-term stability of the F ring core. The stable core presumably supplies the dust grains dominating the ISS and stellar occultation observations; the dust can escape the stable longitudinal sites but is quickly swept up again on surfaces of more massive particles trapped in other stable sites. The scenario, however, does not explain how the entire F ring "true core" of separated, stable sites can maintain a single elliptical orbit with a well-defined pericenter. Murray *et al.* (2008) have suggested that a massive core may help explain this; the tendency of an overly massive core to undergo gravitational instability must be considered, though (Latter *et al.*, 2012).

Finally, we speculate briefly on connections of this scenario to other observations. The "minijet" objects seen by Attree *et al.* (2012, 2014) rarely lie more than 20 km or so from the nominal core semi-major axis, an amount that is comparable to the largest single-encounter Prometheus perturbation and in principle enough to lead to chaotic evolution. However, neither these objects nor the minijets they produce survive more than a few orbits, not long enough to re-encounter Prometheus in their perturbed state roughly 200 orbits later and thereby enter the fully chaotic regime. This is probably because they are quickly

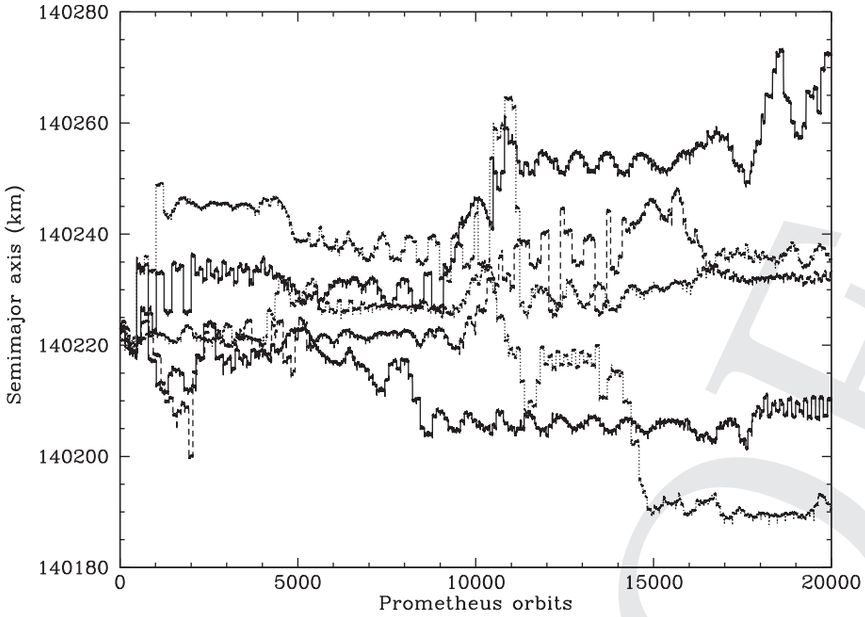

Figure 3.11 The chaotic evolution of the semimajor axes of five randomly chosen test particles, with initial semi-major axes within 10 m of each other, over a period of 20 000 Prometheus orbits. Individual encounters with Prometheus appear as narrow step functions, barely resolved here, spaced by roughly 200 orbits. Limited periods of relative stability can arise, but as soon as the particle encounters Prometheus near its apoapse, chaotic evolution begins with semimajor axis rapidly diverging to a radial spread of 80 km (adapted from Cuzzi *et al.*, 2014a).

damped back to the mean core orbit, or are disrupted, by the very collisions that produce the minijets, and never escape the stable sites. Thus collisional damping/disruption probably does play a role in maintaining the very narrow true core of the F ring and whatever large objects may grow within it, even if temporarily. Recent work on collisional disruption in the tidal environment has been done by Hyodo and Ohtsuki (2014). A prediction of the antiresonance–co-rotation resonance scenario is that the minijet objects lie in stable sites and should cluster under regression in the same way as the RSS detections.

Because Prometheus' orbit *is* chaotic, the stable orbit shifts slightly occasionally and the ring material must adjust; Cuzzi *et al.* (2014b) note some suggestion of this in 2013, just after a relatively large chaotic glitch in Prometheus' orbit (R. Jacobson, personal communication, 2014). During these transition times, some material may leak out of stable sites and become more strongly perturbed. Large objects that are not damped by collisions can then enter chaotic evolutions with semi-major axes ranging over hundreds of kilometers. Emerging cohorts of colliding objects can lead to a more "active" F ring (McGhee *et al.*, 2001; Murray *et al.*, 2008; French *et al.*, 2014).

3.6 DIFFUSE RINGS AND RING ARCS

Two recent review chapters are devoted to a discussion of the diffuse rings of Saturn in some detail (Horányi *et al.*, 2009, and Chapter 12), so here we will only sketch their properties. Figure 3.12 highlights the diffuse E and G rings, in a Cassini image taken in strongly forward-scattering geometry, with the Sun eclipsed by Saturn. Wavelength-size particles concentrate their scattered light into a high intensity beam within a narrow diffraction cone in the forward direction, making them much easier to see for a suitably located observer. Thus the E and G rings, having optical depth of only around 10^{-6}, here reveal the radial structure of their smoke-sized particles very clearly.

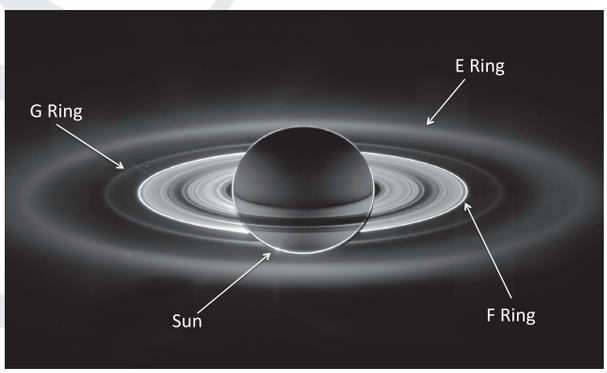

Figure 3.12 Saturn's ring system observed at very high phase angle (in strong forward scattering) that emphasizes tiny dust grains. The diffuse E ring (dust grains originally streaming from jets at the South pole of Enceladus) and G ring (dust and sand-size grains eroded from the surface of the km-size moon Aegaeon) are quite evident. The main rings probably have a small amount of similar fine-grained material, and can also contribute a multiple scattering component in this geometry. The narrow F ring is also bright because of its high abundance of tiny dust grains (Section 3.5.6). Some sunlight can be seen refracted through the planet's limb at lower left, but the spacecraft is essentially looking right down Saturn's shadow. The night side of the planet is illuminated by "ringshine," which is stronger in the southern hemisphere because the south face of the rings is illuminated (adapted from image PIA08329; NASA/JPL and SSI).

The delineation of diffuse rings in forward scattered light by wavelength-sized grains was first seen in the Voyager discovery of the Jovian ring, where it was quickly realized that these short-lived grains (they are quickly destroyed by sputtering) required an unseen underlying skeleton of larger rubble, containing most of the mass, to replenish the visible grains by collisions and/or meteoroid bombardment (Burns *et al.*, 1984). A similar situation was subsequently seen in the rings of Uranus and Neptune (French *et al.*, 1991; Porco *et al.*, 1995). The moonlet

belts underlying dust rings are a good analog for so-called debris disks seen around many other stars (Colwell and Esposito, 1990a,b, 1992; Wyatt, 2008; see also Chapter 20), and the well-constrained scattering phase function of dust in Saturn's diffuse rings (except for the unique E ring) has been proposed as a universal baseline for debris disk scattering properties in general (Hedman and Stark, 2015).

3.6.1 The E Ring: Frosty Breath of Enceladus

The E ring was first seen from Earth in backscattered light when the main rings could be viewed edge-on, and it was realized that its brightness peaked very close to the orbit of Enceladus; Voyager found other intriguing correlations between this odd ring and Enceladus (Horányi *et al.*, 2009). Cassini has now verified this long-suspected relationship. Cryo-volcanic jets near the south pole of Enceladus constantly spew small grains of water ice containing other minor constituents (Porco *et al.*, 2006). Observations suggest that the initial population of E ring particles shares the same size distribution as the Enceladus plume particles (see Chapter 12).

However, electromagnetic forces significantly perturb the eccentricities and semimajor axes of grains that lie in a relatively narrow size range near 1 μm radius. Specifically, apse *regression* due to electromagnetic forces acting on charged particles can cancel the gravitationally induced *precession* for those particles close to 1μm in radius. This allows solar radiation pressure to greatly amplify the orbital eccentricities of the micron-sized grains, leading to the broad radial extent of the visible E ring. The small size and narrow size distribution of most of its widely spread, micron-sized particles gives the E ring its unusual bluish color. At the same time, seasonal out-of-plane solar radiation pressure perturbations distort the E ring vertically, forcing particle apoapses out of the equator plane and away from the sun (Hedman *et al.*, 2012). Plasma drag on the ring particles from the magnetosphere leads to a slight outward radial offset in the location of maximum particle density (Juhász *et al.*, 2007). *In situ* measurements by Cassini CDA and RPWS support these dynamical and photometric inferences (see Chapter 12), and indeed show that the ring extends far beyond its visible limit near $8R_S$, to beyond the orbit of Titan at $20R_S$.

The composition of the E ring particles has been measured directly by Cassini CDA. All are dominated by water ice, but distinct populations have been found containing different contaminants – one set containing small amounts of sodium (presumably from salt) and another set containing silicates and organics (Postberg *et al.*, 2008). These compositions are generally believed to constrain the properties of Enceladus' subsurface liquid water ocean. The tiny E ring grains are sputtered away by magnetospheric ions and photolyzed by sunlight, resulting in even tinier, often silica-rich "stream" particles (Hsu *et al.*, 2011), and releasing oxygen atoms and molecules into the magnetosphere (Hsu *et al.*, 2014). Their removal rate is in general agreement with the production rate of particles from the jets (see Chapter 12). Because of the variability in the Enceladus plume ejecta rate, the E ring brightness and the abundance of oxygen atoms, ions, and molecules derived from it vary significantly in longitude and time (Horányi *et al.*, 2009).

3.6.2 G Ring and Other Debris Rings and Arcs

The G ring, by contrast, has been found to contain a significant population of (relatively) large particles eroded off the 0.5 km moon Aegaeon (Hedman *et al.*, 2010a). This rubble belt was inferred even before the ring was observed visually (van Allen, 1982). In this sense it is much closer to the well-modeled Jovian ring situation (Burns *et al.*, 2004; Throop *et al.*, 2004; Brooks *et al.*, 2004; Showalter *et al.*, 2008, see also Chapters 6 and 12). However, the G ring retains a significant longitudinal asymmetry not shown by the Jovian ring material. Aegaeon is trapped in a stable 7:6 co-rotational resonance with Mimas, and this dynamical trapping is consistent with the angular extent of coarse-grained material ejected by meteoroid bombardment (Hedman *et al.*, 2007d). Finer dust-size particles incur electromagnetic drift and can escape the resonant confinement, extending all around the ring as suggested above for the F ring. Drag on ring particles from the more rapidly orbiting magnetospheric plasma causes a systematic outward radial drift, explaining the more gradually tapered outer edge of the ring (Horányi *et al.*, 2009). There is also a ring of dust centered on the shared orbits of Janus and Epimetheus (Porco, 2006), which Williams and Murray (2011) have shown is likely to be unstable to close encounters between the co-orbitals; this material must thus be continually regenerated by, e.g., meteoroid bombardment and erosion. Winter *et al.* (2014) have addressed the problem and claim to derive an upper limit on meteoroid flux from the observed ring brightness that is at or even below the lower end of the uncertainty range in the flux based on other constraints. More study along these lines would be useful.

Two other small moonlets (Methone and Anthe) are trapped in mean motion resonances straddling Mimas (Spitale *et al.*, 2006; Cooper *et al.*, 2008), and both are embedded in similarly confined arcs of debris (Hedman *et al.*, 2009; see also Chapter 12). Sun *et al.* (2015a) find that, as in the G ring case, the dust abundance and angular extent of these arcs are consistent with meteoroid bombardment of their parent moonlets (although the parameters of the process are uncertain). Other similarly small moonlets that lie further from Saturn include Pallene (in a stable resonance with Enceladus; Spitale *et al.*, 2006) and the Trojan moons of Dione (Helene and Polydeuces) and Tethys (Telesto and Calypso); of these latter five, only Pallene is known to have an associated debris belt, which extends all around its orbit (Hedman *et al.*, 2009).

3.7 MAIN RING COMPOSITION

General background Crystalline water ice is the dominant component of Saturn's ring particles, but ring particles are generally much more red at visual wavelengths than the icy satellites (Filacchione *et al.*, 2012, 2013; see also Figures 3.27 and 3.28 later). The material responsible for this reddening remains unknown but both organic materials (tholins and polycyclic aromatic hydrocarbons) and inorganic materials such as nanophases of iron, hematite or carbon have been proposed (Cuzzi *et al.*, 2009; also see below in this section).

Knowing the primordial, intrinsic composition of the rings will help us understand their origin. However, the primordial

composition of ring material is changed by interplanetary meteoritic bombardment and interaction with magnetospheric and ionospheric particles (Section 3.9). Contamination and mixing processes are especially important in the rings because of their large surface area to mass ratio – about 10^5 times larger than Mimas (see also Chapter 9).

Ring particles show a great variability in size distribution, from small isolated grains in the diffuse D, E, F, and G rings to large chunks assembled into aggregates up to tens of meters in size which dominate the mass and area of the main rings (see Section 3.3 and Cuzzi *et al.*, 2009). In *this* section, "grain sizes" generally refer to regolith grains on the surfaces of much larger, macroscopic "particles" with rough, lumpy surfaces. Visual and near-IR data can be sensitive in several ways to both fine granular structure *and* macroscopic shadowing in lumpy surfaces, as discussed in Sections 3.7.5 and 3.7.6. Connecting the observed spectral properties of the rings with the composition of the material in them involves a complex modeling process leaving room for considerable uncertainty in quantitative abundances (Section 3.7.5). However, qualitative conclusions are on somewhat firmer ground.

3.7.1 Overall Spectral Properties

When observed in the visible and near infrared spectral range (Figure 3.13), Saturn's ring particles most prominently reveal the diagnostic spectral signature of water ice. In the 0.35–0.55 μm range, I/F spectra show a steep "red" slope (their brightness increases with increasing wavelength).[3] In the 0.55–0.95 μm range (some of the literature cited here has used 0.55-0.90 μm), the A and B ring spectra appear relatively flat while the C ring and CD are both moderately red. In the $>$ 1μm NIR spectral range, water ice dominates across the entire ring system showing absorption bands at 1.05, 1.25, 1.5, 2.05, and 3.0 μm, which are comparable in strength to the values measured on Enceladus and Calypso, the most water ice-rich objects in the Saturn system (Filacchione *et al.*, 2012). The presence of a secondary absorption at 1.65 μm, the position of the 2.05 μm band and the single-peak Fresnel feature at 3.1 μm indicate the presence of water ice particles in crystalline form (see Section 3.7.5). Finally, we note that the position of the 3.6 μm continuum peak is a hint of the regolith grain temperature (Filacchione *et al.*, 2014, see also Chapter 15).

The spectrum of Saturn's rings shows a dramatic absorption edge due to water ice at 160–170 nm, as observed by Cassini UVIS (Bradley *et al.*, 2010, 2013), but the spectral region between this drop and 350 nm (Cassini VIMS primarily) has never been observed until recently. Figure 3.14 shows the results of recent observations using the STIS spectrometer on HST (Cuzzi *et al.*, 2017). The agreement is excellent with previous overlapping observations by VIMS (Nicholson *et al.*, 2008; Filacchione *et al.*, 2012) and HST (Karkoschka, 1994; Cuzzi *et al.*, 2002). The key new aspect revealed by these results is the inflection near 300 nm. It is worthy of note that none of the HST observations, STIS or broadband, display the 600–900 nm dip which is often prominent in Cassini-VIMS observations (Figure 3.13) in comparable geometries. In Section 3.7.5, we discuss how modeling is used to constrain the composition of the materials responsible for these spectra.

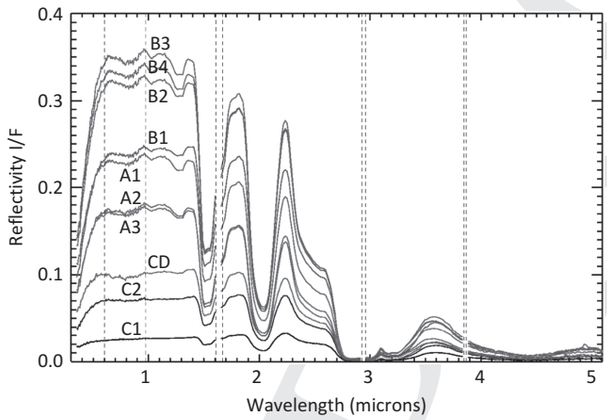

Figure 3.13 Reflectance spectra averaged over different ring regions: C1 (74 658 $\leq r \leq$ 87 523 km), C2 (87 523 $\leq r \leq$ 91 795 km), B1 (91 795 $\leq r \leq$ 99 000 km), B2 (99 000 $\leq r \leq$ 104 500 km), B3 (104 500 $\leq r \leq$ 110 000 km), B4 (11 000 $\leq r \leq$ 117 500 km), CD (117 500 $\leq r \leq$ 122 340 km), A1 (122 340 $\leq r \leq$ 127 000 km), A2 (127 000 $\leq r \leq$ 133 575 km), A3 (133 575 $\leq r \leq$ 136 780 km). Spectral sampling is 7.3 nm/band between 0.35–0.98 μm (VIMS-V range) and 16.5 nm/band between 0.98–5.1 μm (VIMS-IR range). VIS and IR bridging wavelength at 0.98 μm is indicated by the vertical light dashed line. VIMS order sorting filter junctions are indicated by vertical heavy dashed lines (Filacchione *et al.*, 2014). Observations are taken at 20.2° phase angle.

[3] I/F is the reflectivity of a ring surface element, specifically the ratio of its brightness to that of a perfect Lambert surface.

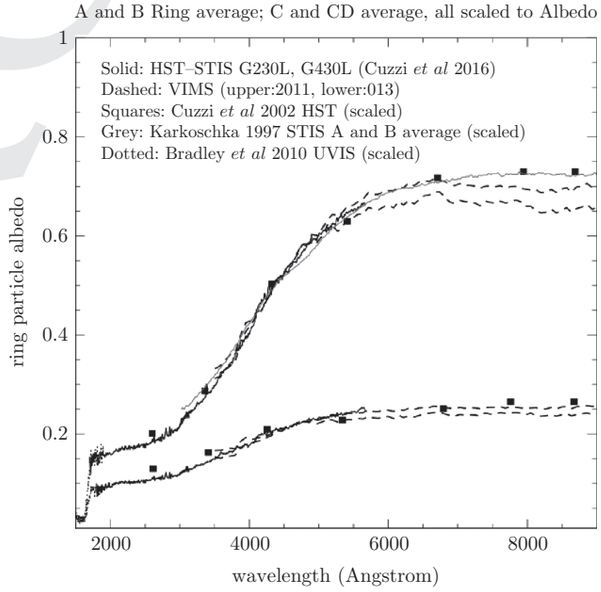

Figure 3.14 Black solid curves: HST-STIS observations averaged over Saturn's B and A rings (top set), and over the C ring/Cassini Division (bottom set). Overplotted are Cassini VIMS observations (dashed; G. Filacchione personal communication), and Cassini UVIS observations (dotted: Bradley *et al.*, 2010). The gray curve is from Karkoschka (1994) and the black squares from Cuzzi *et al.* (2002). Figure adapted from Cuzzi *et al.* (2017); see also Fig. 3.23 for discussion and interpretation.

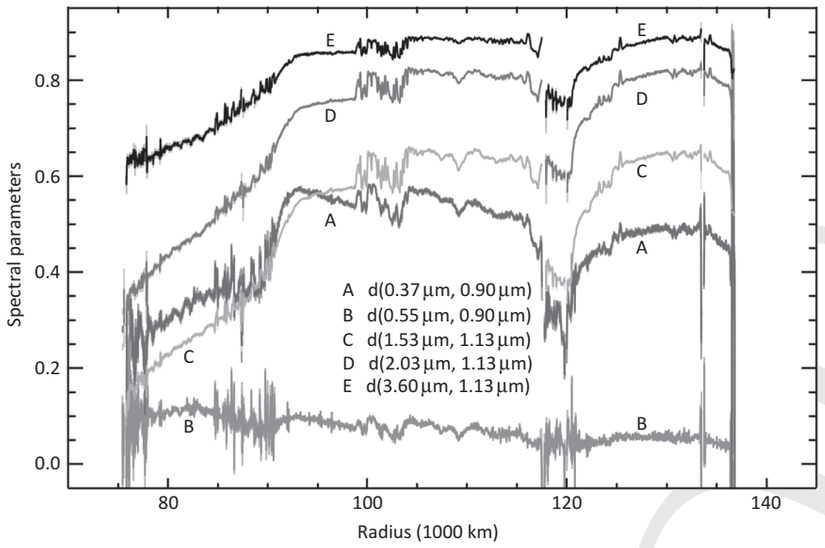

Figure 3.15 Radial profiles of spectral slopes and water ice band depths as measured between or at different wavelengths (Hedman *et al.*, 2013a). In this figure (only), the quantity $d = 1 - I/F(\lambda_1)/I/F(\lambda_2)$, and is either a normalized metric for spectral slope (A,B) or normalized metric for band depth (C,D,E). Enlargements of this plot in the original paper clearly show correlated UV-ice band spectral variability between the C ring "plateaus" and their surroundings and in other locations at the 200 km scale. Similar plots can be found in Cuzzi *et al.* (2009) and Estrada *et al.* (2003).

3.7.2 Radial Variation of Ring Composition

The radial variability of different spectral indicators traces the distribution and mixing of chromophores within and among water ice particles across the Saturnian system (Filacchione *et al.*, 2012, 2014; Hedman *et al.*, 2013a) (see Figures 3.15 and 3.16). The reddening effect between 0.35–0.55 μm is strongest in the higher optical depth (A and B) rings, while it is less pronounced across the C ring and Cassini Division (CD). However, the 0.55–0.95 μm reddening is slightly larger in the C ring and the Cassini division, where the 0.35–0.55 μm slope is small. Filacchione *et al.* (2012) and Ciarniello *et al.* (2011) argue for the presence of a small fraction of dark material in *areal mixing* among the ice particles, compatible with a a similar 0.55–0.95 μm reddening behavior (Hedman *et al.*, 2013a). However, at the end of Section 3.7.5 we caution that a proper allowance for surficial shadows will decrease the amount of such additional "dark" material. The A and B rings, which have stronger reddening in the 0.35–0.55 μm range, also have a larger 2.0 μm band depth than in the C ring (see Figures 3.15 and 3.16).

These different correlations suggest an intraparticle-intramolecular embedding of some UV-blue absorbing material within a dominant water ice matrix (Nicholson *et al.*, 2008), and an independent enhancement of a different component in the C ring and Cassini Division. The ring particle compositional trends derived from VIMS radial profiles are therefore in general agreement with the ballistic transport model (Cuzzi and Estrada, 1998; Estrada *et al.*, 2015b), which suggests that the UV absorber is intrinsic to the rings while the neutral pollutant is extrinsic and due to meteoroid and cometary bombardment. The exogenous dark material accumulates in the ring regions where the optical depth/mass ratio (the opacity) is higher, like the Cassini Division and C ring.

Bradley *et al.* (2010, 2013) have observed the UV reflectivity of the rings with coarse radial resolution, using Cassini UVIS data, and converted the I/F to particle albedo A_B using the observed phase function. The usual technique of assuming a "classical" layer reflectivity dominated by single scattering is *least* problematic in the UV, even for the A and B rings, because of the low ring-particle albedo. While the nonclassical vertical structure still can present a problem for low phase angle observations (see Section 3.7.5), this analysis used a fit to observations covering a wide range of phase angles. Consistent with other work (Figure 3.14 and Cuzzi *et al.*, 2002), the C ring and Cassini Division particles have lower 180 nm ring particle albedos (longwards of the ice absorption edge) than in the A and B ring (Figure 3.17), consistent with more contaminated ring particles. Bradley *et al.* (2010) found an interesting, nearly linear increase in spectral slope from the inner C ring, right across the B–C boundary, and all the way to the B ring outer edge (Figure 3.18), a profile not clearly matching those seen at visual and near-IR wavelengths (Figure 3.15 and Cuzzi *et al.*, 2009), *possibly* hinting at yet another compositional member (but the low radial resolution remains a caveat). On the other hand, Figure 3.17 also shows very little radial contrast *below* the 160 nm absorption edge, because the reflectance of water ice and nonwater ice materials are comparable (at least to our low absolute precision at these low reflectances). Thus, the fractional abundance of the water ice and non-water ice materials are indistinguishable from only the < 160 nm albedos.

3.7.3 Microwave Observations

Microwave (radio and radar) observations have long played a central role in defining the composition of the rings (Esposito *et al.*, 1984). The long wavelength and very low absorption coefficient of ice for microwaves allows them to probe deep inside the subsurfaces of the particles, probably throughout all but the very largest particles. In fact, the often quoted assertion that the rings are more than 90% water ice relies entirely on modeling of decades-old microwave observations, since all other wavelengths can sense only the upper mm or so of material (Esposito *et al.*, 1984, see Section 3.11). Recently, Cassini 2 cm radiometer observations of the rings, taken over a decade, have been reduced and analyzed (Zhang *et al.*, 2017). One of the

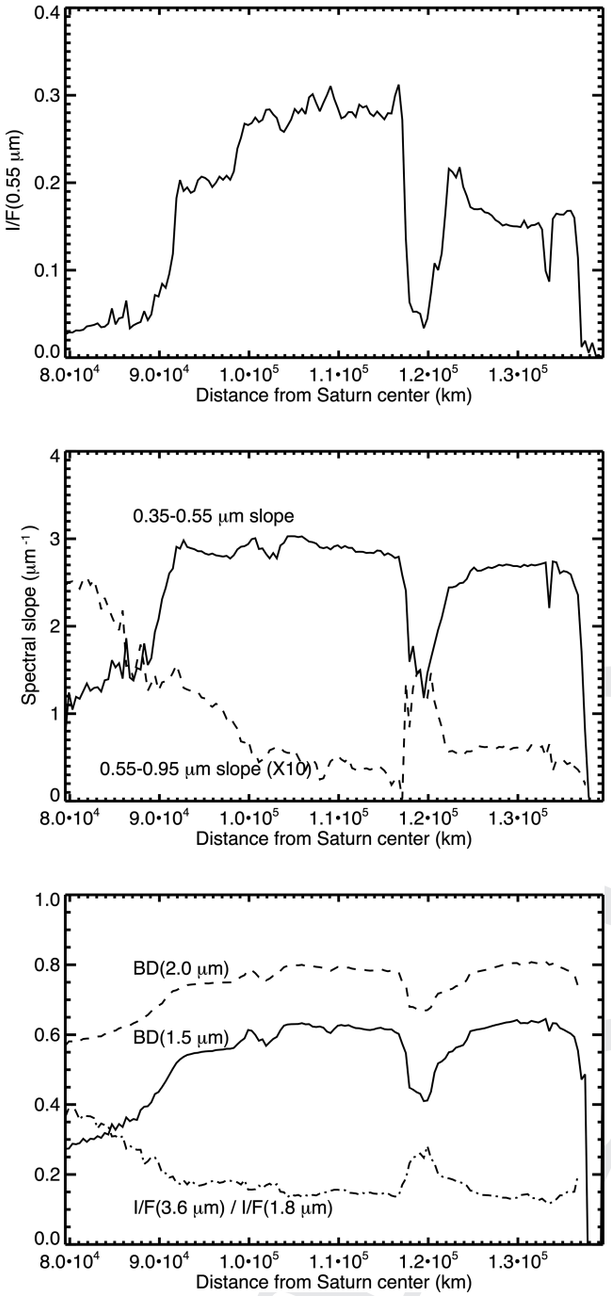

Figure 3.16 Ring radial profiles for visible–near infrared spectral indicators (adapted by averaging multiple low-phase angle observations from Filacchione *et al.*, 2014). Top panel: I/F(0.55 μm); central panel: 0.35–0.55 and 055–0.95 μm spectral slopes; bottom panel: water ice 1.5–2.0 μm band depth and I/F(3.6 μm)/I/F(1.8 μm) ratio. The careful reader will notice qualitative differences in the 0.5–0.9 μm spectral region between this figure and Figure 3.15. These can be ascribed to the difficulty of taking slopes and/or ratios between I/F values that are only slightly different, when background levels are uncertain. In the middle panel the "slope" is a best fit over all the points in the spectral range.

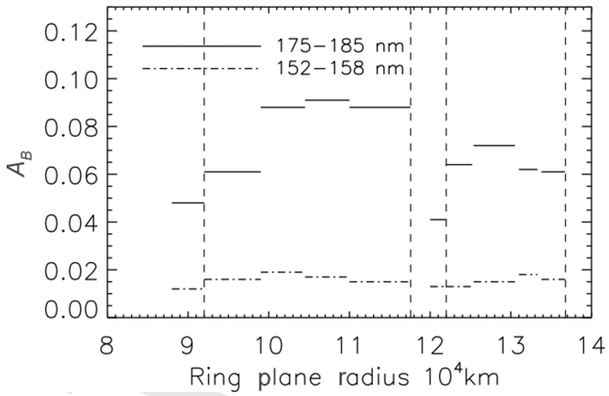

Figure 3.17 Modeled values of ring particle spherical (Bond) albedo A_B averaged over two wavelength ranges from the Cassini UVIS instrument (see Section 3.7.2). These values represent a best fit of Equation 3.5 to the I/F observed over a range of geometries, including phase angles between 5° and 60–80° (Bradley *et al.*, 2013).

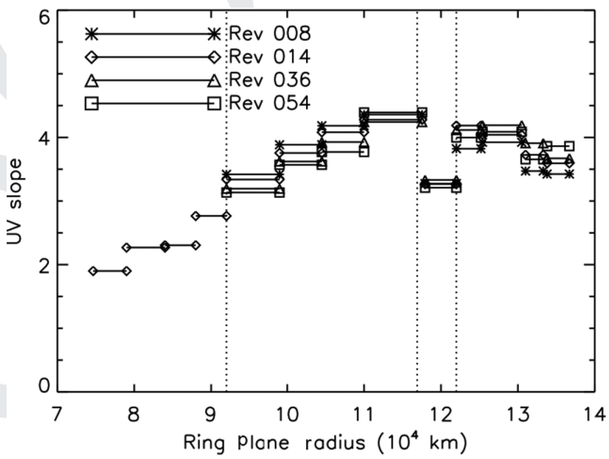

Figure 3.18 The spectral slope calculated as the ratio of I/F between 175–190 nm (just longward of the water ice absorption edge) to that between 140–160 nm (shortward of the ice edge), so in *some* sense a metric for the fractional abundance of uncontaminated water ice (Bradley *et al.*, 2010). Note, however, that the radial profile is qualitatively different from the radial profile of water ice band depth (curves C and D in Figure 3.15). A more noticeable step near 10^5 km, consistent with Figure 3.15, would be inferred from ratioing the two A_B profiles in Figure 3.17.

most interesting and straightforward results is a radial profile of a non-icy absorber buried within the ring particles in the C ring (Figure 3.19). The radial profile shown is the *mass fraction* of nonicy material, assuming the dielectric properties of a typical silicate. The fact that it somewhat resembles the optical depth profile in shape leads to a brightness temperature proportional to τ^2. The visual, NIR, and UV "color" profiles of the C ring, which map out the properties of the top tens of microns of material, have different radial profiles (Figures 3.15 and 3.16) *except* for the radial profile of the 0.55–0.90 (or 0.95)μm slope, which does show a radial variation similar to τ (or, the nonicy

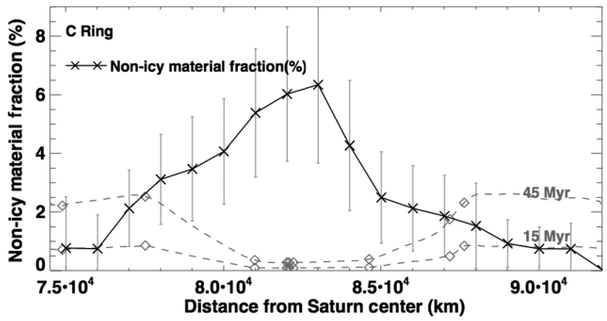

Figure 3.19 Black curve: Non-icy material fraction derived from Cassini 2 cm radiometer observations. Grey dashed curve: The non-icy material fraction as evolved over 15 and 45 Myr if meteoroid bombardment is the only source of contamination in a structurally fixed ring, and the flux has remained constant. Grey diamonds indicate locations where opacity measurements have been made through density waves. Figure adapted from Zhang *et al.* (2017).

fraction shown here) in the C ring (curve B of Figure 3.15 and the third panel of Figure 3.25). Zhang *et al.* (2017) interpret their results as suggesting that a 25 km radius rocky centaur was disrupted and emplaced in the region shown in Figure 3.19 some 20–30 Myr ago, enhancing both the non-icy content with some component of fine-grained dirt mixed into the ice, as sensed by the 2 cm radiometer, *and* the surface mass density (by embedding many sizeable rocky chunks within the local C ring material) over the range 77 000–89 000 km). Filacchione *et al.* (2012), Figure 20 (bottom panel) suggests a compositional continuum between the classical icy satellites and the CD, B, and A rings, but shows that the C ring is off this trend, with a larger 0.55–0.95 μm spectral slope. This may be consistent with the emplacement of some kind of interloper as suggested by Zhang *et al.* (2017), or it may be due to something else.

3.7.4 The F Ring Composition

Intermediate in properties between the main A, B, C rings and the diffuse D, E, G rings, the F ring is still somewhat of a dynamical puzzle (see Section 3.5.6). Since the Voyager era, the diffuse appearance of, and strong forward scattering by the ring has suggested the presence of very small particles (Showalter *et al.*, 1992; French *et al.*, 2012, 2014). Cassini VIMS observations carried out in forward scattering geometry at very high phase angles (177.4°–178.5°) revealed the Christiansen feature of crystalline water ice at 2.87 μm, and have been used to infer a grain size distribution and composition by means of the effective medium theory (EMT; Vahidinia *et al.*, 2011). The spectra were best modeled with water ice particle *aggregates* (as opposed to uniform density particles) having a porosity up to 30% and a "stubby" power law radius distribution running between 10–30 μm (Figure 3.20); that is, the discrepancy in depth of the well-defined Christiansen feature at 2.86 μm between the observations, and the black curve in Figure 3.20 is removed). The wavelength of the absorption indicates that the composition is dominated by crystalline water ice (see also Hedman *et al.*, 2011b, who studied the effect in other dusty ringlets as well).

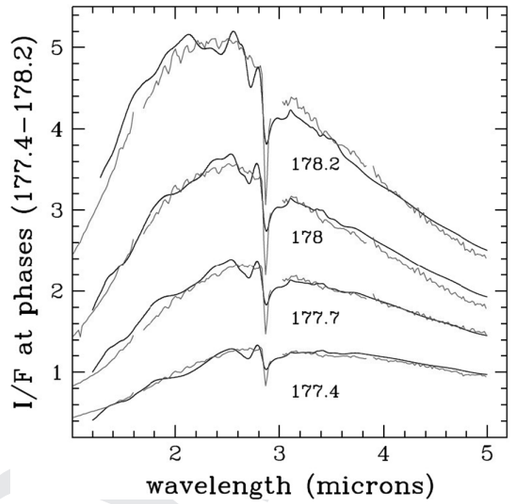

Figure 3.20 VIMS F ring high-phase observations (gray lines) simulated by ice particles having 30% porosity and a stubby powerlaw size distribution between 10 and 30 μm (black lines). Note the 2.87 μm crystalline water ice Christiansen feature (Vahidinia *et al.*, 2011).

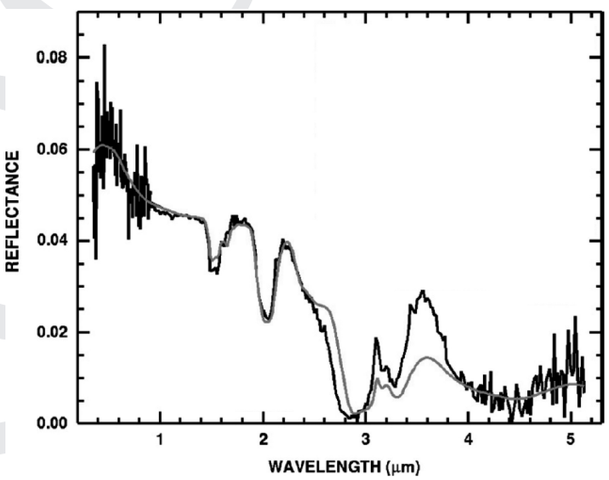

Figure 3.21 VIMS F ring low-phase observations (black curve) simulated with a radiative transfer model (gray curve). The model composition is described in section 3.7.4 (Clark *et al.*, 2012b).

Other constraints on the F ring composition have been obtained from VIMS spectra (Clark *et al.*, 2012b). Low phase angle (20°) VIMS observations were modeled with Hapke theory, giving the best spectral fit with an intimate mixture of seven grain sizes, each of four different materials (water ice with traces of iron and hematite nanophases and carbon dioxide), in a 40 % areal mixture with 200 mm (20 cm!) diameter blocky water ice particles containing 0.001% by weight of iron nanophase particles. The resulting percentage by weight is 97.3% water ice, 1.7% iron nanophase particles, 0.8% hematite nanophase particles and 0.19 % carbon dioxide (Figure 3.21). The unusual blue slope and peak at short wavelengths is attributed to Rayleigh scattering by Clark *et al.* (2012b), consistent with the known abundance of sub-micron particles in the F ring based on phase-angle brightness variations. The

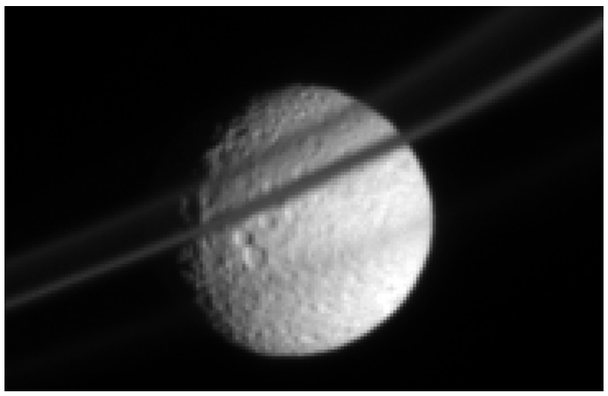

Figure 3.22 An unusual image showing two F ring strands, one opaque and having a lower brightness than the surface of Mimas at moderately low phase angle. Image PIA 09806, NASA/JPL and SSI.

large blocky particles in the model of Clark *et al.* (2012b) (Figure 3.21) would be undetectable in strongly forward scattered observations such as in Figure 3.20, but are plausible because Cassini radio occultations require *some* azimuthally spotty, radially narrow constituent of large objects (see Section 3.5.6). The mismatch near 2.6–2.9 μm is ascribed by Clark *et al.* (2012b) to insufficient tiny grains, but the mismatch near 3.1–3.6 μm is ascribed to the need for cleaner blocky surfaces – testifying to the complexity of modeling multicomponent systems. We discuss compositional modeling in general in Section 3.7.5.

It is difficult in general to obtain the absolute brightness of the F ring *particles*, because the ring brightness depends strongly on the local optical depth, which is highly variable spatially and temporally. One qualitative indication that the F ring particles are *not* pure ice is shown in Figure 3.22, where two F ring strands occult Mimas at a moderately low phase angle. One strand is not only *opaque*, in that it obscures Mimas, but its brightness is also less than that of Mimas at this phase angle. More careful modeling is needed to determine if a large degree of forward scattering can explain this (Showalter *et al.*, 1992; French *et al.*, 2012, 2014), whether it is a form of layer-surface-brightness effect, or whether the F ring particles are actually more polluted than the surface of Mimas.

3.7.5 Radiative Transfer Models: Caveats and Implications for Ring Composition

Radiative transfer models become very complex when the medium is made of closely packed, many-particle aggregates. In these cases compositional retrievals may have hidden model-based dependencies. The characterization of the light scattered by the rings at different phase angles helps us to separate the ring-particle properties from those of the layer as a whole. Near-zero phase-angle observations are useful to study the opposition effect, which mainly arises in the grainy regoliths of macroscopic particles (Section 3.7.6). By contrast with the case usually seen in diffuse rings composed mostly of tiny, wavelength-sized, forward-scattering particles (Section 3.6), rings filled with bright particles having sizes much larger than the wavelength, while dominated by singly *backscattered* light, can also produce significant intra- and inter-particle *multiple backscattering*, which ends up at high phase angles. Inter- or intra-particle shadowing, caused by finite particle sizes and close packing, is a complexity not generally considered to date in compositional inversions, but may have significant implications, as discussed below under *Caveats regarding nonclassical layers*.

The overall ring redness has been reproduced several ways in previous models. Some assume a regolith of water ice monomer particles, each containing much smaller embedded, or *intramixed*, grains of organic material (tholins) and amorphous carbon (Poulet *et al.*, 2002, 2003); see below, however, for caveats regarding shadowing and carbon. In support of organics, weak features have been detected by VIMS at 3.42–3.52 μm, compatible with the CH_2 aliphatic stretch signature (Filacchione *et al.*, 2014), as well as on Iapetus (Cruikshank *et al.*, 2014). The fairly subtle redness of the C ring has also been replicated using Rayleigh absorption by a few parts per thousand of nanophase iron and/or hematite grains mixed within larger water ice grains (Clark *et al.*, 2012a,b). Iron metal can be oxidized to hematite by ring atmosphere molecules (H_2O, OH, O_2; see Section 3.9). However, while organics have been detected *in situ* in E ring material (Postberg *et al.*, 2008), iron is rare in the magnetosphere and has not as yet been reliably detected in juxtaposition with ring material (Srama *et al.*, 2011; Christon *et al.*, 2015, S. Kempf, personal communication).

The ring-averaged UV-visual spectra of Cuzzi *et al.* (2017; see Figure 3.14) were modeled to test all of these possibilities, which have observable effects at UV-vis wavelengths because of the great transparency of ice longward of its 170 nm absorption edge. The analysis used standard Hapke theory, but corrected for both shadowing on the particle surface and for nonclassical layer effects (see various "*Caveats*" below). Because of the sensitivity of the location of the UV edge to grain diameter, a characteristic value of 5–10 μm can be regarded as reliable in this wavelength range (Bradley *et al.*, 2010), allowing estimates to be made of the mass fraction of nonicy pollutants with confidence. An excellent spectral fit (Figure 3.23) was obtained using a very small mass fraction (about 0.2%) of primarily aromatic "Low-Pressure" (LP) tholins (Imanaka *et al.*, 2004; West *et al.*, 2014) embedded in water ice. Organic material of similar composition but dominated by aliphatic bonds ("High-Pressure" or HP tholins) could not provide a decent fit with only a single type of grain, but by adding a free parameter, "intramixtures" of HP tholin-enriched grains with pure ice grains can come fairly close (Figure 3.23). While *actual* organics in the rings may be different than these particular experimental products, this result suggests that organics responsible for the A and B ring redness are dominated by aromatics, rather than aliphatics. Aromatic organics lack a strong 3.4 μm band, so would be very hard to detect in the NIR (Cuzzi *et al.*, 2017). Cuzzi *et al.* (2017) also found that the A and B ring spectra were much less well fit by iron, "nano-iron", or silicates (Figure 3.23).

After allowing for surface shadowing as constrained by the observed particle phase function (see *Caveats regarding intra-surface shadowing* below), no additional amorphous carbon or other neutral absorber was needed, and indeed only a small amount can be allowed, in the A or B rings. By comparison, the

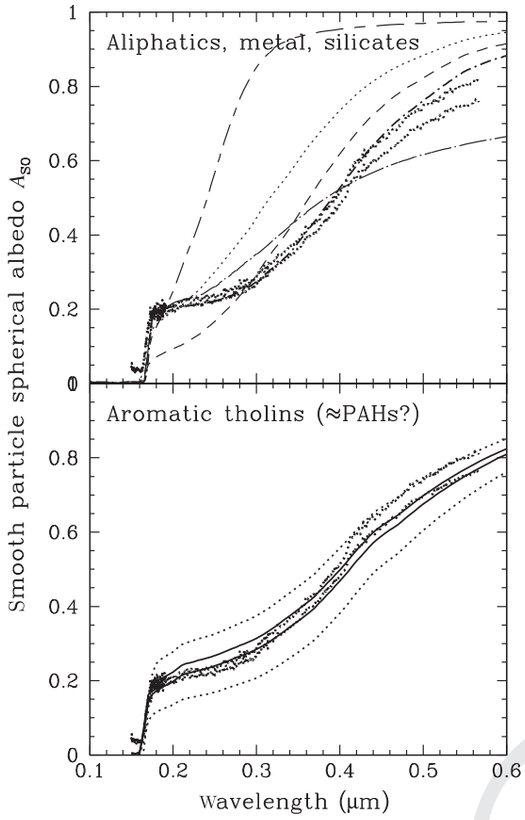

Figure 3.23 A comparison of *absolute* Hapke-model-based, smooth ring-particle albedo spectra (Figure 3.14 showed only scaled values of geometry-corrected I/F) as a function of wavelength, inferred by Cuzzi *et al.* (2017) from HST-STIS and Cassini-UVIS observations after accounting for ring layer effects and particle surface roughness (plausible range indicated by the two heavy dotted curves). Volume fractions f of "pollutant" assume 10 μm diameter regolith grains, as constrained by the Cassini UVIS spectral edge at 170 nm (Bradley *et al.*, 2010). Top: long dash-short dash: Silicate in ice with $f = 0.004$; dotted and short-dashed lines: aliphatic (HP) tholins in ice, $f = 0.002$ and 0.005 respectively. Dot-short dash: *two* component intimate mixture (95% pure water grains, mixed with 5% water grains containing $f = 0.06$ HP tholins); Dot-long dash: Fe metal with $f = 0.004$ intramixed in ice grains. Bottom: Single component intramixtures of aromatic (LP) tholin in ice. Upper and lower dotted curves: $f = 0.0007$ and 0.002 respectively; upper and lower solid curves: $f = 0.010$ and 0.012 respectively. All curves here have grain scattering asymmetry factor $g = 0.7$. Different flavors of Hapke theory change the overall slopes of the curves slightly (Cuzzi *et al.*, 2017).

very same analysis of the C Ring *requires* some 4–6% by mass of a combined silicate-neutral carbon absorber mix, in addition to the 0.3% LP tholin as in the A/B rings, to match the shape and absolute value of the particle albedos (Cuzzi *et al.*, 2017). These results are consistent with the findings of Zhang *et al.* (2017) from 2.5 cm radiometry. The very different C ring composition we find relative to the A and B rings is consistent with the finding that aliphatic organics were found mostly in the C ring and Cassini Division (Filacchione *et al.*, 2014). Distinction between aliphatic and aromatic tholins has not yet been made for the C ring based on models of the UV-vis spectra, but this will be interesting to explore. Laboratory studies (Boduch *et al.*, 2011; Shi *et al.*, 2011) have suggested that oxidants such as H_2O_2 or O_3, perhaps in ionized forms, might be created by ion bombardment or UV irradiation of ice. While these materials do absorb at very short wavelengths, no dedicated searches have as yet been made for spectral evidence for or against them in the rings.

Ciarniello *et al.* (2016) have modeled the composition of ring particles by adopting an intimate mixture of two populations of grains: (I) one population made of water ice with tholin inclusions and (II) another population made of pure amorphous carbon. The relative amount of the two populations is given by p_I and $p_{II} = 1 - p_I$, respectively. Tholin inclusions are intraparticle mixtures within water ice grains (Ciarniello *et al.*, 2011), and the relative tholin abundance in a single grain corresponds to $p_I^t = 1 - p_I^{H_2O}$. While these endmembers seem appropriate for the A and B ring particles, modeling of the C ring needs a third population of particles (III) corresponding to an intraparticle mixture of water ice and amorphous carbon with relative abundance $p_{III}^c = 1 - p_{III}^{H_2O}$ (Poulet *et al.*, 2003). In Ciarniello *et al.* (2011) and Ciarniello *et al.* (2016), Hapke's model is used to get the single scattering albedo, while optical constants used are from Imanaka *et al.* (2012) for tholins, from Zubko *et al.* (1996) for amorphous carbon and from Warren (1984), Mastrapa *et al.* (2009), and Clark *et al.* (2012b) for water ice. The distribution of grain diameter d in the regolith has been modeled with a power-law function d^{-3} with a minimum ($d_{\min}$) and maximum ($d_{\max}$) grain diameter. The resulting best spectral fits are shown in Figure 3.24 and listed in Table 3.1. However, if Cuzzi *et al.* (2016) are right about shadowing on rough particle surfaces (see below), these amounts of neutral (carbon) absorber may be overestimates.

An interesting multiple-composition regolith model for the ring particles has been developed by Hedman *et al.* (2013a),

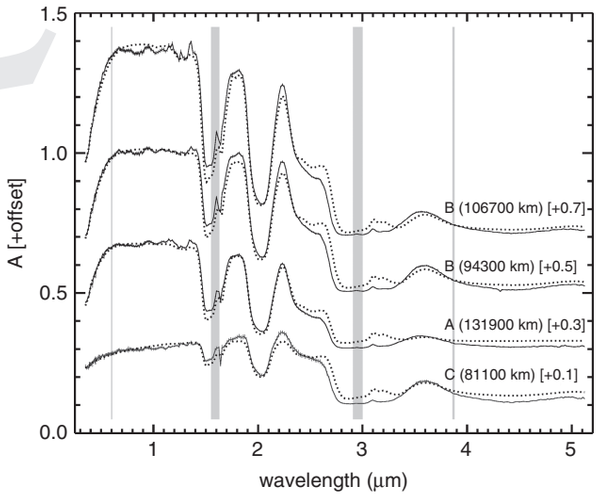

Figure 3.24 Spectral fit of the Bond albedo A for four ring regions, C(81100 km), B(94 300 km), B(106 700 km), A(131 900 km) adapted from Ciarniello *et al.* (2016). The solid curves are the Bond albedo retrieved from VIMS observations and dotted lines the modeled spectra. Vertical gray bars correspond to VIMS order sorting filters junctions. Spectral modeling compositional parameters are given in Table 3.1

Table 3.1. *Spectral modeling compositional parameters for A, B, C rings (see section 3.7.5 and Ciarniello* et al.*, 2016). The parameters $p_I - p_{III}$ are fractional abundances for different grain populations, with minimum and maximum diameters d_{min} and d_{max} (see text).*

Ring	p_I	p_{II}	p_{III}	$p_I^{H_2O}$	p_I^t	$p_{III}^{H_2O}$	p_{III}^c	d_{min}	d_{max}
C (81100 km)	0.41	0.29	0.30	0.99953	0.00047	0.9916	0.0084	38 μm	204 μm
B (94 300 km)	0.87	0.13	–	0.99912	0.00088	–	–	36 μm	363 μm
B (106 700 km)	0.96	0.04	–	0.99951	0.00049	–	–	35 μm	506 μm
A (131 900 km)	0.75	0.25	–	0.99956	0.00044	–	–	102 μm	617 μm

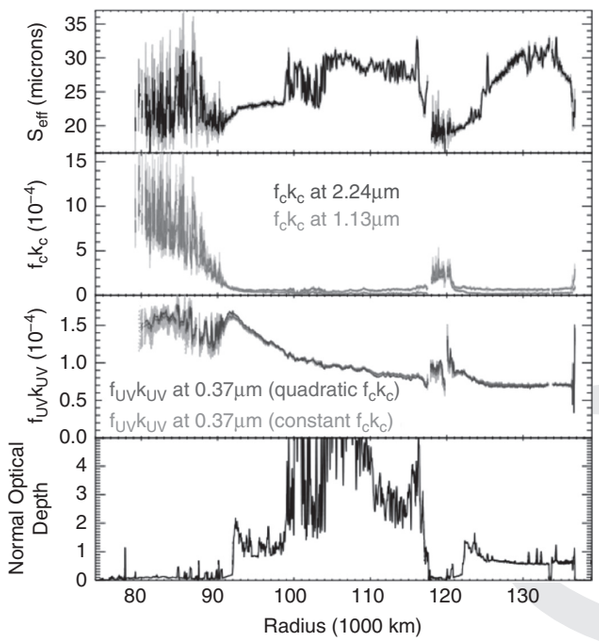

Figure 3.25 Bottom: Standard τ profile; first panel up: $f_{\rm UV}k_{\rm UV}$ for the UV-absorbing material as mapped by the 0.35–0.55 μm slope (with negligible dependence on the assumed form of the "constant" absorber); second panel up: $f_{\rm c}k_{\rm c}$ for the weakly reddish, possibly silicate, material as mapped by the 0.55–0.90 μm slope; top panel: "effective" grain diameter $S_{\rm eff}$ consistent with the above determinations *and* the observed water ice band depths. Adapted from Hedman *et al.* (2013a).

with the aim of disentangling the effect of the ring particle composition from the effects of the texture of the ring particles' regolith. This analysis (Figure 3.25) determines a regolith grain diameter $S_{\rm eff}$, and the local product fk where f is the fractional mass and $k = 4\pi n_i/\lambda$ is the absorption coefficient of some nonicy constituent, with n_i the imaginary refractive index at wavelength λ, for multiple constituents. Hedman *et al.* (2013a) find that an enhanced concentration of a spectrally neutral contaminant characterizes the particles in the C ring and Cassini Division, leading to the lower albedo measured for particles in these regions. A second major contaminant, absorbing light at short visible and near-ultraviolet wavelengths, is also needed. This UV-absorbing material is found to be smoothly distributed, with abundance increasing inwards across the A and B rings, but then falling off in the outer C ring before rising again in the mid-C ring (Figure 3.25). Radial variations in $S_{\rm eff}$ (top panel), are much more variable on small lengthscales. In some places these variations are clearly correlated with the ring's optical depth, while in other places, they correlate with disturbances generated by strong spiral density waves caused by satellites.

Caveats regarding nonclassical layers While it is possible that the regolith grain size could vary so systematically on such short radial scales as shown in Figure 3.25 (top panel), in a fashion that correlates with ring optical depth (lower panel), there are other possibilities. The analysis of Hedman *et al.* (2013a) has the classical layer reflectivity (Equation (3.5)) built into it. It has been shown by Salo and French (2010, their Figure 7 in particular) that "nonclassical" ring layers in which particles are closely packed can have higher reflectivity at low phase angles, by 25–65%, than the predictions of Equation (3.5). The effect depends on the width of the particle size distribution, as well as on the underlying optical depth. The observations involved with Figure 3.25 were obtained at phase angles between 13° and 41°, and may manifest this effect in a radially variable way that correlates well with optical depth, because of variations in volume density and/or particle size distribution, but the model inversion of Hedman *et al.* (2013a) lumps all ring layer effects into the parameter $S_{\rm eff}$. It would be interesting to repeat the analysis of Hedman *et al.* (2013a) using their higher-phase-angle dataset, which is less subject to this nonclassical effect. In general, all low-phase-angle observations, certainly from Earth or HST, must allow for these nonclassical layer effects. It should also be kept in mind that Salo and French (2010) themselves make several approximations, such as Lambert-surfaced particles, that are worthy of further study in the future.

Caveats regarding microwave observations As noted in Section 3.7.3, decades-old analyses of radar and passive microwave observations provide the fundamental constraints on the bulk composition of the ring material. However, some of the assumptions of these models require reassessment (see Section 3.11).

Caveats regarding intra-surface shadowing The absolute amount of "neutral absorber", traditionally added to the regolith mix in previous work to bring the ring particle albedo at long visual wavelengths down from that of nearly pure ice to observed values (Cuzzi and Estrada, 1998; Poulet *et al.*, 2002), is probably an upper limit because shadowing in rough surfaces makes real particles darker than the predictions of Hapke theory and its variants as ordinarily used (Cuzzi *et al.*, 2016). While known for some time to aficionados of Hapke theory (Hapke, 1993, Chapter 12), this effect has not been treated previously by ring modelers in general, and has implications for ring composition and age.

3.7.6 Regolith Grain Sizes; the Opposition Effect

Regolith grain sizes are required to obtain quantitative abundances of non-icy contaminants from models of observed brightness and spectra. To a first approximation, for minor contaminants in water ice, the abundance of the contaminant is inversely proportional to the assumed regolith grain size. There are several ways to constrain the size of regolith grains. The opposition effect is one of the longest-known aspects of Saturn's ring photometry. Originally regarded as being due to shadow hiding in a very low-volume-density "classical" ring (see Cuzzi *et al.*, 2009, for a discussion), more recent work concludes that it is a highly localized multiple scattering between neighboring regolith grains called "coherent backscattering," which constrains a combination of grain size and composition (Déau *et al.*, 2013; Déau, 2015). The opposition effect has been measured on ISS images at high resolution; important parameters are the amplitude A and angular width W of the brightness surge, and the angular dependence of the I/F at larger phase angles well outside the surge. The inferred $A(\tau)$ and $W(\tau)$ are nearly constant across the whole ring system when $\tau = 0.7$. For $\tau < 0.7$, $A(\tau)$ and $W(\tau)$ show decreasing values across the A, B, and C rings. Across the entire ring system the angular dependence of the I/F at phase angles well *outside* the surge appears to obey a roughly $\tau^{0.5}$ dependence, in agreement with the predictions of the shadow hiding effect (Déau *et al.*, 2013). The coherent backscattering effect, which can be related to the size of the regolith grains, is more likely to explain the narrow ($< 1°$ wide) angular surge near zero phase - however, the relation is complicated by the absorptivity of the grains (Cuzzi *et al.*, 2009; Déau *et al.*, 2013; Déau, 2015).

Determining the regolith grain size from the depths of NIR ice absorption bands is a perhaps more well-understood tool (Poulet *et al.*, 2002, 2003; Cuzzi *et al.*, 2009). The 2 μm band depth and the I/F(3.6 μm) to I/F(1.8 μm) ratio (see Figure 3.16) both allow us to derive the regolith grain size through comparison with pure water ice laboratory spectra (Filacchione *et al.*, 2014). The resulting grain diameter for the A and B rings is 80–100 μm (from the 2.0 μm band depth) and 50–80 μm (from the I/F(3.6) to I/F(1.8) ratio). For the C ring, a grain diameter of 20–50 μm is obtained from both the 2.0 μm band depth and the I/F(3.6) to I/F(1.8) ratio. For the Cassini division, a 50–60 μm particle diameter is obtained from the 2.0 μm band depth and a diameter of <30 μm is obtained from the I/F(3.6) to I/F(1.8) ratio. Also, Bradley *et al.* (2010, 2013) derive regolith grain sizes from the shape of the 170 nm UV ice absorption edge, Déau (2015) derives grain sizes from the opposition effect, Morishima *et al.* (2012) derive grain size from thermal properties, and Cuzzi *et al.* (2009) review grain size results from several different techniques. In general, the "grain size" determined at a given wavelength turns out to be roughly proportional to the wavelength used. These factors and uncertainties should be kept in mind when contemplating the implications of any derived composition.

3.8 RINGMOONS: ISOLATED AND EMBEDDED

Saturn's ring system – from the classical main rings through the extended and diffuse rings – is intertwined with a large and diverse family of small moonlets or ringmoons (see also Chapters 8 and 16). We previously mentioned the role of moonlets in observed ring structure in Sections 3.5.1, 3.5.3, 3.5.4, and 3.5.6.

3.8.1 Known, Observed Ring-Moons

A number of moonlets in the 10 to 100 km diameter range have been observed within, and just exterior to, the main rings. These objects have been found to have low mass density (around or even less than 0.5 g cm^{-3}) and low strength, filling their Roche lobes (Porco *et al.*, 2005, 2007; Thomas *et al.*, 2013a,b). They are probably all rubble piles to a large extent, although they may have solid cores. Ohtsuki *et al.* (2013) discuss accretion within the Roche zone and connections to the current size and shape of small moonlets.

Pan, Daphnis, and Atlas, which orbit within or just outside the main rings (Section 3.5.1), have very pronounced equatorial "skirts" of accreted rubble, giving them a flying-saucer appearance (Thomas *et al.*, 2013b). These skirts arise because the vertical thickness of nearby ring material is much, much smaller than even a several-km diameter moonlet (Section 3.4), so the ring material is swept up close to the moonlet's equator. A stable spin pole is required of the moonlet for this to occur, and no such buildup is seen on any of the larger, more remote objects (even Prometheus, which routinely enters the F ring's diffuse envelope); nor are Prometheus and Pandora especially close to Roche-lobe shape (Thomas *et al.*, 2013b). These differences may have implications for the significance of the surface composition for the origins if these objects (see below). Daphnis is very clearly on an inclined orbit relative to the nearby Keeler gap edges, as seen by shadows cast by its edge waves near equinox (Weiss *et al.*, 2009), and the thickness of its equatorial skirt is determined by its orbital inclination. Pan, on the other hand, shows no evidence for out-of-plane motions, possibly because they have been damped (Ward and Hahn, 1994). The eggshell-smoothness of these skirts, and other surfaces of the various small moonlets (Thomas *et al.*, 2013b), has led to suggestions that electrostatic dust levitation and redistribution is an important process on the surfaces of these tiny moons where gravity is extremely weak (Hirata and Miyamoto, 2012).

The dynamical properties of the known moonlets include several resonant or near-resonant interactions with the classical icy satellites and/or with each other (Cooper and Murray, 2004; Spitale *et al.*, 2006; Jacobson *et al.*, 2008). As mentioned in Section 3.5.6, Prometheus and Pandora's interactions produce occasional chaotic, and coupled, glitches in their orbit periods (French *et al.*, 2003; Goldreich and Rappaport, 2003; Renner *et al.*, 2005), amounting to semimajor axis jumps of a fraction of a kilometer. Cooper *et al.* (2015) give a good review of the history of the twitchy orbits of these two objects; improved observations show that the Prometheus–Pandora orbital jumps are not restricted to times of apse antialignment as was originally thought, consistent with Farmer and Goldreich (2006). These results have implications for the long-term stability of the F ring's "true core" (Section 3.5.6). Cooper *et al.* (2015) also identify the cause of the resonant trapping of the small ring-moons Anthe, Aegaeon, and Methone and find that Atlas's orbit is chaotic. Caudal (2013) argues that tidal influences on the Janus–Epimetheus system suggest that the co-orbital configuration was established 25 Myr ago.

3.8.2 Compositions of the Known Ring-Moons

Prometheus and Pandora are similar in showing the highest H_2O band depths (larger than 0.8) among all the Saturnian satellites, appearing very similar to the A and B ring particles. Conversely, with a band depth of about 0.6, Janus and Epimetheus are more similar to the more "polluted" C ring and Cassini division particles (Section 3.7). However, Prometheus and Pandora appear to be different in visual wavelength color. Prometheus is redder than Pandora, Janus, and Epimetheus (Filacchione *et al.*, 2013) and is the only ring-moon showing a reddening similar to A–B ring particles. The primary color difference between Prometheus and either Pandora, Janus, or Epimetheus is in the 0.35–0.55 μm range, and the spectral slopes for all of them are fairly similar in the 0.55–0.95 μm range. The colors of Pan and Daphnis are less well known, but based on their physical appearance it would never be clear whether their surface properties represented some underlying "core," or merely a coating of main ring material. The spectral properties of Saturn's classical icy satellites (except for Iapetus and Hyperion which have steeper 0.55–0.95 μm slopes) are much closer to those of Pandora, Janus, or Epimetheus than to those of Prometheus or the A and B rings (Filacchione *et al.*, 2012, 2013). As it has been argued that the unusual 0.35–0.55 μm "redness" of the A and B rings best represents their "initial" composition in some sense (Section 3.7), then Prometheus, which shares this property, seems to provide the best link connecting the main rings with nearby ringmoons (see Section 3.10).

The small objects Aegaeon, Methone, and Pallene, which are all embedded in diffuse dust rings, differ in composition: Aegaeon, buried within and arguably providing the source for the G ring, seems to have a *low* albedo, while the others seem to be predominantly icy (Hedman *et al.*, 2010a; Thomas *et al.*, 2013a,b).

3.8.3 Embedded Moonlets

By far the most numerous "ring-moons" are those that have never been seen directly, because they are too small to clear out a complete, circumferential, empty gap around themselves but are able to reveal themselves by their local perturbations on surrounding ring particles. The perturbations, which cause "propeller"-shaped disturbances in nearby ring material, are usually modeled as gravitational forces (Spahn and Sremčević, 2000; Sremčević *et al.*, 2002; Seiß *et al.*, 2005; Michikoshi and Kokubo, 2011), but Lawney *et al.* (2012) find that similar structures can be produced purely by collisional pileups. Vertical perturbations of ring material by propeller objects have been connected to shadows cast on the rings near equinox (Hoffmann *et al.*, 2013, 2015). An animation of the local dynamics near a propeller object can be found in Cuzzi *et al.* (2010). For detailed descriptions of the physics involved, and more observational examples, see Chapter 8 in this volume.

While objects of this type – typically on the order of 100 m radius but ranging up to 1–2 km radius – are found in all of the main ring regions, the largest, most numerous, and most well-studied reside in the A ring; these serve as the class type, although embedded objects in other regions (see below) are expected to behave in similar ways.

"Propeller" objects in the A ring Flocks of sub-km objects were discovered in three radial bands in the middle and outer A ring (Tiscareno *et al.*, 2006, 2008; Sremčević *et al.*, 2007), as described in earlier reviews by Colwell *et al.* (2009) and Cuzzi *et al.* (2009) where a "group photo" can be found. The size estimates for the underlying objects rely on difficult measurements of the very slightly different orbital radii of poorly resolved brightness fluctuations caused by their local optical-depth perturbations, and the brightness fluctuation is a function of illumination geometry. Improved photometric modeling of propeller wakes (Tiscareno *et al.*, 2010a) has refined these inferences. The size distribution of embedded propeller objects is very steep, and their total inferred mass is a negligible fraction of the total A ring mass.

More recently, so-called "giant propellers" have been discovered that are large enough (1–2 km radius) to be individually reacquired and tracked over time, allowing accurate measurements to be made of their orbital motion and semimajor axis (Tiscareno *et al.*, 2010b). Interestingly, these giant propeller objects are only found outside of the Encke Gap, while normal sub-km propeller objects are almost entirely seen inside of the Encke Gap.

It was immediately realized that the semi-major axes of these objects were changing with time (Tiscareno *et al.*, 2010b). This exciting discovery quickly led to a number of models of the "migration" of large propeller objects, ranging from deterministic torque balance or oscillatory models (Pan and Chiang, 2010, 2012; Tiscareno, 2013a) to random walk models under gravitational scattering by density fluctuations (Crida *et al.*, 2010; Rein and Papaloizou, 2010; Pan *et al.*, 2012). Random walk models are currently favored, but a problem remains with the mass scale of the perturbations required to match the meanderings of actual propeller objects (typical self-gravity wake masses are too small). One possible solution is that the giant propeller objects are being scattered off of huge clumps of "straw" forming in density wave crests (see Figure 3.7); the outer A ring is filled with spiral density waves where "straw" could, in principle, be formed. For reviews in more detail see Chapter 8.

While the A ring "propeller" objects are the most well characterized, there is good evidence for relatively large local, embedded objects, causing somewhat different observable disturbances but still orbiting at near-Keplerian rates, in the B and C rings, and elsewhere. In 2012, right at the very outer edge of the A ring, an object dubbed "Peggy" was revealed by its propeller-like perturbation of local ring material (Murray *et al.*, 2014), and tracked for eight months (see Figure 3.26). The object subsequently split into two or more objects orbiting at different rates, which receded back into the A ring, but the last detections in mid 2015 suggest it may have moved back towards the outer A ring edge (C. Murray, personal communication, 2016). Other "Keplerian features" have been seen and tracked near the outer edge of the B ring (Spitale and Porco, 2010), and near the edges of the Huygens ringlet in the Cassini Division (Spitale and Hahn, 2016). Glitchy structures have been seen along the edges of the Keeler gap (Porco *et al.*, 2005) as well. Evidence from Cassini images and UVIS occultations has also been presented for propeller-like features in the B ring, suggesting km-size objects at semi-major axes of 94 958 and

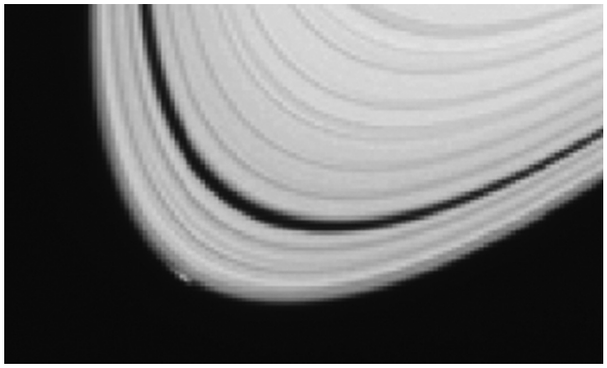

Figure 3.26 This figure shows a small bright clump right at the A ring edge, which apparently fragmented shortly after this image was taken (Murray *et al.*, 2014). This object may have been an unusually "lucky" large particle concentration – hundreds of meters across – analogous to the last two panels in the bottom row of Figure 3.3. It has since broken into several smaller pieces.

112 921km (Sremčević *et al.*, 2011b, 2012, 2013, 2014). These locations are in no way special, or correlated with known gaps or other remarkable features. Similarly, narrow, nearly empty gaps have been seen in the C ring and Cassini Division in stellar occultation data (Baillié *et al.*, 2013). The regions observed contain no self-gravity wakes, so the observed gaps are most likely "propeller-like" features caused by locally large particles. from these gaps, Baillié *et al.* (2013) infer a population of objects between several and several tens of meters in radius. The C ring objects do seem to be smaller than the Cassini Division objects. It is hard to assess the size distribution of these objects in detail because of possibly smaller gap-causing efficiency at their small-size limit, which approaches the size of the largest "ring particle," but in no case could they extend to the hundreds-of-meters radius commonly seen in the A ring propeller objects.

Finally, the intermediate size range between embedded, randomly diffusing propeller objects too small to see directly, and large, isolated, gap-trapped objects (Pan and Daphnis) has been studied by Bromley and Kenyon (2013). They find that deterministic radial migration in the "type-I" sense (by net torque imbalance, without gap clearing) studied by Ward (1997) and others, would quickly remove any 1–10 km radius objects from within the A ring, if they ever did exist there, either into the Encke and/or Keeler gaps, or away from the ring outer edge entirely as originally suggested by Goldreich and Tremaine (1982). Such sweeping out may explain the steep embedded ring-moon size distribution in this size range, as well as, perhaps, provide sources for the several different nonaxisymmetric ringlets found in the Encke Gap (Section 3.5.1).

3.8.4 Origin of embedded objects

Perhaps the most important question regarding large objects in or near the rings, whether isolated such as Pan, Daphnis, Prometheus, etc., or embedded such as the propeller objects, is – are they shards of some primordial parent body, or are they locally (and perhaps recently) grown from the basic ring material (Section 3.10). In recent years several hypotheses have been advanced along the lines of the latter type of scenario. Traditional physics such as gravitational instability has been studied (Griv, 2011), as well as accretion in tidally dominated environments (Yasui *et al.*, 2014). This physics is discussed in more detail in other chapters in this volume (see Chapter 8).

A separate line of thought envisions local formation as triggered by compression of patches of ring material due to some external perturber, much as "straw" is seen to arise in dense crests of spiral density waves. Beurle *et al.* (2010) observed perturbations in F ring strands, assignable to local (but unseen) objects orbiting precisely where Prometheus perturbations would create a maximum amount of streamline compression. They argued that compaction in these locations had actually created discrete, cohesive objects capable of perturbing their surroundings. The fact that these characteristic perturbations are *not* found *far* from streamline compression regions suggests that the objects so formed are perhaps only weakly bound, and are eventually battered back to their components by collisions (Murray *et al.*, 2008). A more general line of thought advocating a cyclic production and destruction of locally large objects has been dubbed the "predator–prey" model by analogy to how populations of hares and wildcats vary in nature (Esposito *et al.*, 2012; Torres *et al.*, 2013). In this model, conditions oscillate between low relative velocity environments favoring growth of locally large objects, until their own presence begins to drive relative velocities to large values capable of eroding or destroying them, upon which the larger frequency of dissipative collisions damps the system again into an accretionary state. This cycle might be free, or might be driven by regular local streamline compressions such as found near ring edges or Prometheus encounters.

3.9 RING GAS AND DUST "ATMOSPHERE" AND IONOSPHERE

The entire system of *diffuse* E and G rings resides within Saturn's magnetosphere, and electromagnetic interactions between tiny charged grains that are prominent (even dominant) in these rings, and the enveloping plasma and magnetic field, are of great importance; these subjects are discussed in detail elsewhere (Horányi *et al.*, 2009; see also Chapter 12). The relationship of the *main rings* to their own local atmosphere and ionosphere, created by photosputtering and meteoroid bombardment (Johnson *et al.*, 2006; Luhmann *et al.*, 2006), and how this regime connects with the global magnetosphere, were reviewed by Cuzzi *et al.* (2009); more recent advances can be found in Tseng *et al.* (2010, 2013). Oxygen atomic and molecular ions in particular are abundant in the ring atmosphere and ionosphere, and may play a role in creating oxidized iron compounds which (it has been suggested) may be responsible for the rings' reddish colors (see Section 3.7). These species show seasonal changes caused by the solar elevation above the ring-plane, with an observed minimum in 2010 after equinox (Elrod *et al.*, 2014).

A question of perennial interest is whether atomic or molecular ions, or tiny charged ring particles, can spiral along field lines into Saturn's ionosphere and upper atmosphere (Northrop and Hill, 1982, 1983a,b; Connerney and Waite, 1984; Cuzzi *et al.*, 2009). The equatorial latitudes of Saturn could even be

affected (Liu and Ip, 2014). A flurry of recent interest in this "ring rain" has been prompted by recent observations appearing to show a correlation between latitudinal variation of upper atmosphere composition and magnetic "L-shell" radii crossing the rings, suggesting a substantial water flux precipitating into Saturn (O'Donoghue *et al.*, 2013; Connerney, 2013; Moore *et al.*, 2013). However, these fluxes and abundances are not, on the face of things, entirely consistent with Cassini radio occultation determination of ionospheric densities, which are also affected by water molecules (Moore *et al.*, 2015). Thus the intensity of ring rain remains somewhat unsettled. In its "Grand Finale" orbits, when it threads the needle's eye between the rings and planet, one of Cassini's prime goals is to *directly measure* the flux of material from the rings to the planet, and perhaps *vice versa*.

3.10 ORIGIN AND EVOLUTION

The uniqueness of Saturn's rings has always challenged theories of their origin. In 1847, Edouard Roche famously suggested the tidal disruption of an inwardly evolving satellite, a "intrinsic" ring origin that has been expanded to cover tidal disruption of an "extrinsic" interloper from beyond the Saturn system. The first quantitative "intrinsic" ring origin scenario (see review by Pollack, 1975, and references therein) relied on primordial condensation of the present-day ring system in a cooling circumplanetary disk that filtered out early-formed silicates and retained only ice, to satisfy the ice-dominated composition of the rings. An inescapable assumption of the "condensation" model is that the rings formed, like the planets themselves, at the birth of the solar system. Harris (1984), based on new insights from Voyager regarding impact destruction of icy moons (Smith *et al.*, 1981, 1982) introduced the important concept of rings as derivative from earlier but locally formed moons of various sizes, tying Saturn's rings (conceptually at least) to other ring systems that had then been discovered, and introducing some flexibility to the *time* of ring origin. Since the Voyager era, the time of ring formation has assumed a leading role in the saga, in that several arguments lead to formation times much more recent than the nominal 4.5 Gyr of solar-system formation, creating difficulties for both intrinsic and extrinsic scenarios.

In any case, we need to look back through a very substantial evolution of ring properties to tease out their "initial" state. Two of the main processes thought to be driving evolution in today's ring system are (a) viscous and dynamical evolution, and (b) meteoroid bombardment. Below, we briefly describe these processes and then review the leading ring origin scenarios, all of which regard the rings as derivative of some earlier-formed parent. The reader is referred to several recent review chapters (including one in this volume) for a deeper discussion of ring and satellite system origin theories (Charnoz *et al.*, 2009; Johnson and Estrada, 2009; Mosqueira *et al.*, 2010b; see also Chapter 18).

3.10.1 Viscous and Dynamical Evolution and Origin of Close-in Ring-Moons

The current ring viscosity, as constrained by wave damping, ring thickness, and particle size or self-gravity wakes (Figure 3.6, bottom) is far too small to evolve the rings globally (e.g. spread them significantly) on timescales shorter than the age of the solar system (Goldreich and Tremaine, 1982; Schmidt *et al.*, 2009), but the preservation of small-scale sharp edges does require "shepherding" of some sort (Schmidt *et al.*, 2009) to prevent spreading on short timescales. Discrete moonlets can evolve radially on shorter timescales, due to angular momentum transfer in their numerous resonances with remote and local ring material (see chapters cited above). Comparison of the sizes of Pan and Daphnis with the widths of the Encke and Keeler gaps validates the torques obtained from nominal approaches. The rates of semi-major axis expansion for the close-in ringmoons under these torques would drive them away from the rings in a time much less than the age of the solar system (Goldreich and Tremaine, 1982), while the A ring would shrink accordingly. This was the original "short-timescale" problem with Saturn's rings. However, Poulet and Sicardy (2001) found that outward evolution of the closest-in ring-moons could be frustrated by extended periods of resonance trapping and/or mutual destruction requiring reassembly, weakening this process over time and providing a possible way out of the dynamical age problem.

Depending on their origin, the rings might have started with a much higher surface mass density, which has a higher viscosity and faster evolution timescale due to strong self-gravity wake effects. Salmon *et al.* (2010) found the current system to have some resemblance to models with age on the order of 10^8 years. However, their models included no "shepherding" or ballistic transport physics (see below) that might preserve ring edges, so may not preclude a much older system. Charnoz *et al.* (2010) modeled such a viscously spreading disk, allowing accretion to occur at its outer edges (last panel of Figure 3.3). The moonlets so formed recede from the rings based on their wave torques, shepherding the ring edge with isolated resonances as is observed. The observed radial and mass distribution of small ringmoons (Atlas through Janus/Epimetheus) was matched fairly well after 500 Myr, and evolution slowed thereafter (however, no attempt was made to model inter-moonlet resonances, as in Poulet and Sicardy, 2001). The exciting discovery of "Peggy" (Section 3.8) suggested that we were seeing this process in action, but Peggy broke into multiple objects that apparently continue to wander in and out near the A ring edge (C. Murray, personal communication 2016). So, the moonlet birth process is apparently complicated.

3.10.2 Meteoroid Bombardment, Ballistic Transport, and Ring Pollution

An entire chapter is devoted to this process in this volume (see Chapter 9) so we will only sketch the highlights. Interplanetary meteoroids bombard the rings, depositing a cosmic mix of ices, silicates, and carbonaceous material; the impact ejecta cannot escape the rings but transport mass and angular momentum radially. Saturn's rings are highly sensitive to evolution under this process, because their intrinsic non-icy fraction is so small (Section 3.7) and their surface-to-mass ratio is so huge (10^5 times larger than Mimas). Both ring structure *and* ring composition are affected. Doyle *et al.* (1989) found that the estimated meteoroid mass flux into the rings would "pollute" the ring material to the observed nonicy fraction in about 10^8 years; this became the second "short timescale problem" for Saturn's rings.

Subsequently, Durisen *et al.* (1992, 1996) showed that observed ring structure (such as inner A and B ring edges) could be produced by ballistic transport on a comparable timescale and then Cuzzi and Estrada (1998) found that observed global and regional radial profiles of ring particle color and albedo could also be produced by meteoroid bombardment on the same timescales of a few hundred Myr. Specifically, darker and less-red C ring and Cassini Division particles arose naturally in the context of bombardment of an initially icy but reddish ring by dark, neutrally colored meteoroids. This is because the more massive A and B rings suffered less *fractional* pollution than the C and CD regions (given the incidence angles involved, nearly all incoming material interacts with all main ring components, which have greatly varying surface mass densities). Even the radial profile of color at the inner B ring edge resembled model predictions.

Ballistic transport models have a number of parameters, some constrained by experiment and some less so. Estrada *et al.* (2015b) combined the structural and compositional evolution modeling and re-assessed the parameter dependence. In general, the conclusions are unchanged regarding global structure and composition, but really matching *local* structure and composition such as in the C ring plateaus remains a challenge that will require more realistic modeling of ejecta and/or local viscosity/mass density.

One of the more subtle parameters is the ejecta yield; unlike lab experiments in which a large projectile slams into a solid or even grainy surface, the ring particle surfaces are bombarded by projectiles not much bigger than a regolith grain, and the microstructure of these surfaces may vary from place to place depending on the compaction of the particles by collisions (see Chapter 15). Another regime as yet untreated is destruction of a ring particle by a relatively large meteoroid; the angular distribution and speeds of the ejecta will be quite different from those currently modeled by cratering ejecta. The underlying viscosity and surface mass density σ of different regions are not yet well understood – for instance, density wave mass densities suggest that the C ring plateaus, while having higher τ than their surroundings, are no different in σ (Hedman and Nicholson, 2013, 2014).

Ring mass density In a more profound, global sense, it has been suggested that σ for the main rings in general (in particular the dense A and B rings) could be *much* larger than generally believed because mass could be "hidden" in dense clumps (Robbins *et al.*, 2010). A much larger σ would more easily resist pollution darkening, perhaps allowing the rings to have a primordial age. However, while taking the mass flux at its current value over only the past few 10^8 years may not be a bad guess, one probably encounters a steeply increasing and unconstrained meteoroid mass flux in pushing back to primordial times, so a larger current ring mass alone doesn't *guarantee* a primordial age. Moreover, there is little uncertainty in the A ring mass densities (Figure 3.6), so if the B ring *were* much more massive, one would need a younger age for the A ring, coincidentally in proportion to the σ ratio, to explain why its color and brightness agree so well with those of the B ring (Estrada *et al.*, 2015b). Finally, new analyses of spiral density wave features in dense parts of the B ring (Hedman and Nicholson, 2015) lead to σ values in good agreement with traditional estimates. In any case, Cassini plans to measure σ directly in its Grand Finale orbits using the tiny gravitational perturbations of the rings on the spacecraft's orbit, and resolve this issue.

Meteoroid mass flux Perhaps a more serious uncertainty surrounds the incoming meteoroid mass flux. The value most often used (Grün *et al.*, 1985; Cuzzi and Estrada, 1998) assumes a "cometary" population, and satisfies spacecraft observations (Landgraf *et al.*, 2000). These estimates are highly uncertain, because the meteoroid size containing most of the mass flux is probably much larger than sampled by spacecraft observations. Moreover, newer models suggest that the primary meteoroid population at Saturn derives from collisions between prograde, ecliptic "Kuiper Belt" objects, and retains those orbits as it drifts inwards (Han *et al.*, 2011; Poppe and Horányi, 2012). The gravitational focussing by Saturn depends strongly on whether pre-encounter orbits are "cometary" or "ecliptic."

The Cassini CDA investigation has attempted, by multiple methods, to detect the incoming meteoroid mass flux independently of the known E ring background (see Figure 3.27). Indirect techniques were first attempted, as in Sremčević *et al.* (2005), using close flybys of Tethys and Rhea; nothing was detected, giving only an (unpublished) upper limit on meteoroid mass flux (R. Srama, personal communication 2014). More recently, the growing sample of *direct* detections, in regions uncontaminated by E ring material, is starting to set meaningful constraints, which will improve in the last few years of the mission. This work-in-progress has been reported by Kempf *et al.* (2013, 2014); while not apparent from the published abstracts, the CDA team is leaning towards a mass flux not too different from the traditional value (Chapter 9, and S. Kempf, personal communication 2015). A firmer conclusion, from the CDA standpoint, is that the incoming population is clearly Kuiper-Belt-like in orbital properties, and not cometary. On the other

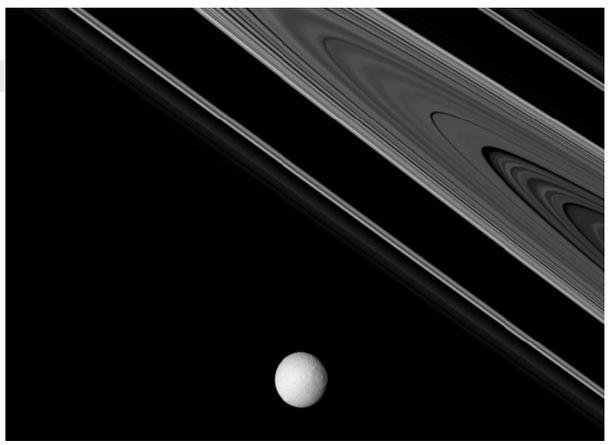

Figure 3.27 A near-true-color Cassini image capturing the (unlit face of) the rings, and Tethys. Even without any color enhancement it is obvious that the rings are substantially "redder" than Tethys. The color difference can be seen in spectra, as a more drastic quantitative drop in brightness between the Cassini Green and Blue (or UV) filters; the wavelength where the drop occurs does not differ much between the rings and the icy satellites (Filacchione *et al.*, 2012). (A black and white version of this figure will appear in some formats. For the color version, please refer to the plate section.)

hand, a model developed by Poppe (2016) finds that Oort cloud comets, Jupiter family comets, and KBOs contribute almost equally to the mass flux at the rings. The directional properties of the incident flux do have implications for ballistic transport (see Chapter 9), so it seems there is more work to be done reconciling models and observations.

The specifics of the meteoroid size distribution are also of interest, because while the 1–100 μm particles carrying most of the mass leave polluting nonicy materials close to particle surfaces, impacts by larger projectiles are needed to mix the pollution throughout the ring layer. Models of the regolith mixing of pollutants have been developed by Elliott and Esposito (2011, 2015). Further modeling of this process, and more careful analysis, may turn up *recent events* such as at albedo anomalies noted in the B ring by Cuzzi *et al.* (1984).

While we hope the Cassini CDA never has the chance to sample a cm-sized particle moving at km/s, several other indirect observations may help to constrain the meteoroid size distribution in that size range. The flux of objects in the m-size range has been estimated from their impacts on the rings (Tiscareno *et al.*, 2013a; Schmidt and Tiscareno, 2013) and there may be some hope for detection of larger objects even from Earth (Hueso *et al.*, 2013). The Cassini RPWS instrument observed still-unexplained detections of impulsive plasma waves during Saturn Orbit Insertion (SOI) that *may* be caused by ring impacts, and if so allows a number flux to be determined (Gurnett *et al.*, 2004). However, sophisticated modeling is needed to infer the *size* of the projectiles involved from the strength of the observed pulses (D. Gurnett, personal communication 2006, and work in preparation).

3.10.3 Ring Parent: Intrinsic or Extrinsic?

As noted above, and discussed in more detail by Charnoz *et al.* (2009; see also Chapter 18), ring formation scenarios can be thought of as either *extrinsic* or *intrinsic*. In either case, the properties of the materials involved, and of the so-called "Roche zone" where tides dominate accretion, must be kept in mind (Tiscareno *et al.*, 2013a; Hedman, 2015). In cases involving either extrinsic ring parents, or extrinsic projectiles disrupting *intrinsic* ring parents, low flux through Saturn's Roche zone is a consistent problem, especially for "young" rings. Pushing ring formation back to the beginning of the solar system, or to the only slightly younger "Late Heavy Bombardment" period, to increase the flux of projectiles, runs afoul of "young" (i.e. 400–500 Myr old) ring arguments.

Extrinsic origin Extrinsic scenarios envision the tidal disruption and partial capture of some close-passing interloper from beyond the Saturn system. Such a scenario is the most straightforward to analyze, both in terms of the flux of interlopers, which is constrained by observations of comets, and in terms of tidal disruption itself (Dones, 1991; Dones *et al.*, 2008; Charnoz *et al.*, 2009; Leinhardt *et al.*, 2012; Hyodo *et al.*, 2015; see also Chapter 18). While not impossible, such a scenario is statistically unlikely. The actual flux of km-radius (and maybe even 25-km radius) interlopers (Hedman *et al.*, 2011a; Marouf *et al.*, 2011a; Hedman and Showalter, 2016; Zhang *et al.*, 2017) may be slightly higher than normally assumed, but not by the several orders of magnitude it would take to make a "young" (*c.* 500 Myr) ring origin by this path plausible. In fact, extrinsic parent models must be "lucky" twice over – both in the low probability of having the proper close encounter geometry in the age of the solar system (not to mention in the 500 Myr age of the "young" ring scenario) and again to be an unusual *differentiated* centaur-like object, with a nearly rock-free mantle available to make the rings.

Intrinsic origin Intrinsic ring origin would involve either some kind of nebula condensation scenario (Pollack, 1975; only plausible if the rings are primordial) or the destruction by tidal stresses or impact (possibly by some interloper) of some ice-rich moon that grew within the Saturn system. Models of the creation of the narrow rings of Uranus and Neptune by destruction of small, locally grown moons are well developed (Colwell, 1994, and references therein), but the sheer mass of Saturn's rings *and* their dominance by ice (which requires a differentiated parent), force us to consider the entire process of the formation and evolution of satellite systems containing objects large enough to differentiate.

There are several main schools of thought on how this transpired (and derivatives of each); the end products are similar by design and choice of parameters, but the underlying physical assumptions and the properties of the circumplanetary nebulae involved are rather different (Canup and Ward, 2002, 2006; Mosqueira and Estrada, 2003a,b; Estrada and Mosqueira, 2006). With the possible exception of the problem of Iapetus (Mosqueira *et al.*, 2010a), there are few testable predictions to distinguish these models, and from the standpoint of the formation of Saturn's rings, it seems either one could serve up an appropriate mix of precursors.

The simplest intrinsic model might just involve the catastrophic destruction by an interloper of some intrinsic, ice-rich moon lying not too far beyond the Roche zone. The flux of objects large enough to destroy already present, Mimas-size moons is much larger than the flux of already-Mimas-size, differentiated interlopers as required by extrinsic formation scenarios, and formation of a "young" ring system in this way is not improbable given the proper parent in the proper place.

In another intrinsic model, Canup (2010) describes a multistage scenario fleshing out Roche's original suggestion quantitatively, in which a partly differentiated, Titan-sized ring "grandparent" is stranded close enough to Saturn at the end of accretion to evolve inwards and be ripped apart tidally, with tidal heating contributing to differentiation. The icy mantle is stripped off and repelled back outside the Roche zone by torques from the silicate core, which is lost into the planet. The nearly pure ice can then reaccrete into a Rhea-size ring parent, which subsequently *also* tidally evolves back inside the Roche zone and is again torn apart to produce a very massive primordial ring. The massive ring evolves very rapidly (Salmon *et al.*, 2010), losing mass into the planet and evolving into the current ring. Note however, that the *actual* ring parent is a Rhea-sized, primarily icy object residing close to Saturn, an end condition not incompatible with alternate satellite formation models (Mosqueira and Estrada, 2003a,b). Either way, a sizeable icy moon close enough to enter the Roche zone by tidal evolution at all, cannot survive tidal evolution for *long*, so this simple a scenario is unlikely to produce a "young" ring. A *massive* early ring could resist meteoroid pollution better than today's

(probably) Mimas-mass ring, but massive rings are not *guaranteed* to be primordial, because early *pollution fluxes* were probably much larger than today's, as well.

A third variant, involving "late" formation of the Saturn ringmoon system, has been suggested by Asphaug and Reufer (2013). In this model "late" means post-Late Heavy Bombardment (say, 3.8 Gyr ago), but perhaps this scenario could operate as recently as 500 Myr ago. This scenario envisions a more or less stable primordial satellite system resembling that of Jupiter, with fewer and larger moons than seen in Saturn's system today, all differentiated. Something destabilizes the system (several possible causes are speculated on), and the large moons enter a regime of mutual, destructive collisions in which their icy mantles are stripped away to form the ice-rich rings and mid-size, ice-rich satellites like Tethys, while the remnants merge into Titan. Based on the angular and size distribution of crater counts on the midsized moons, Dones *et al.* (2009) had previously wondered if a "Nice-model-like" destabilization had destroyed a previous satellite system, allowing the current icy moons to accrete from a planetocentric swarm of debris which could leave such a cratering fingerprint.

A dynamically motivated scenario leading to just such a catastrophic restructuring of the Saturn system has been recently discussed by Ćuk *et al.* (2016), who argue from orbital properties that the midsized moons of Saturn are probably *not* primordial, but indeed only about 100 Myr old. Their scenario is that an "evection" resonance (between satellite orbit precession and the sun, moving at the orbit period of the planet) destabilizes a prior, more stable system that had been slowly evolving outward under planetary tidal torques.

The composition of the original, pre-pollution ring material surely contains clues as to its parentage. One great advantage of intrinsic models is that the Saturnian system is, for whatever reason, full of ice-rich, differentiated objects, spread throughout the system; in this it is actually slightly unusual, like the rings themselves. On the other hand, most (but not all) Mimas-size interloper centaurs would be dark, probably undifferentiated objects. Indeed the rings (and Prometheus) are much redder between 0.3–0.55 μm wavelength than any of the moons but the difference is quantitative, rather than qualitative, and the clusters of ring and satellite colors indeed connect, suggesting perhaps different surface processing from similar starting materials (Section 3.7 and Figure 3.28). Visual inspection of icy moon spectra *does* show short-wavelength absorptions qualitatively similar, but less dramatic, than seen in the rings (Filacchione *et al.*, 2012).

However, the extreme redness of the rings does create problems. Pollution models (Cuzzi and Estrada, 1998) suggest the original icy-red material was not far from today's A/B rings in composition which, according to several models, is most consistent with a small amount ($\sim$ 2% by mass) of intramixed organic material, perhaps rich in aromatic compounds (Section 3.7). Whether the intrinsic redness is caused by organics or iron, the *direction* of color evolution under meteoroid bombardment is *away from* the icy-red A/B rings, through the less-so C ring and Cassini Division, *to* spectral properties resembling Dione, Rhea, and Janus (see Figure 3.28). The less-red and more-icy Mimas, Tethys, and Enceladus can be explained by surface pollution of the Dione–Rhea–Janus composition by nearly pure

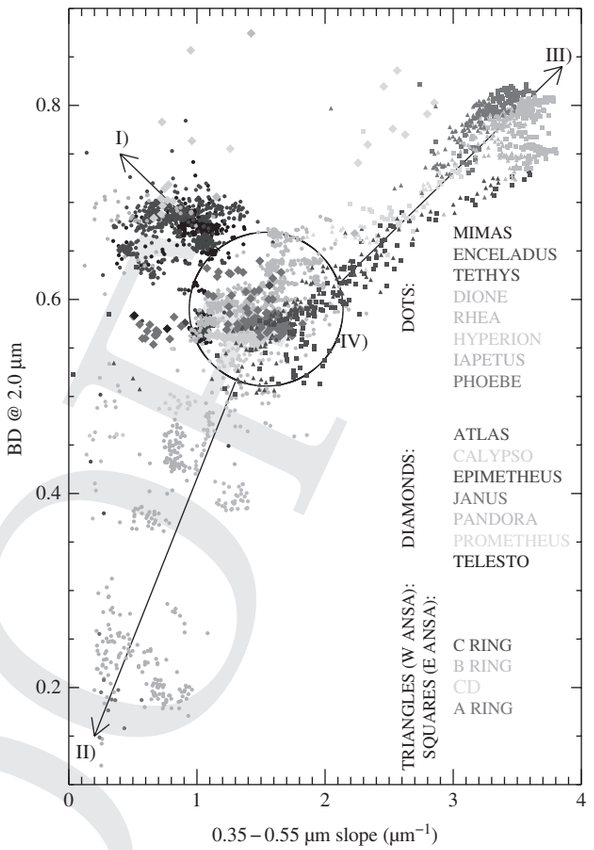

Figure 3.28 Scatterplot of the 0.35–0.55 μm slope vs. 2.0 μm water ice band depth for icy satellites and rings from VIMS observations from Filacchione *et al.*, 2012. Data show four different clusters. (I) High albedo icy satellites, grouped in the top-left diagonal branch, including Enceladus, Tethys, Iapetus trailing hemisphere, Pandora, and Calypso as extremes. These objects are the most water ice-rich, having large band depth and low reddening. (II) Low albedo icy satellites: these are spread through the bottom left diagonal branch, which includes Phoebe, Iapetus leading hemisphere and Dione trailing hemisphere. These surfaces show the lowest amount of water ice in the population. (III) A–B rings and Prometheus, grouped in the top-right diagonal branch, correspond to the maximum band depth BD(2.0 μm)=0.85 and maximum reddening S(0.35–0.55 μm)=3.8 μm^{-1}. (IV) Intermediate albedo satellites and rings are contained in the central circle around BD(2.0 μm)=0.55 and S(0.35–0.55μm)=1.5 μm^{-1}. This group includes Rhea, Dione leading hemisphere, Hyperion, Janus, C ring, and CD. One plausible evolution takes intrinsic icy surfaces *from* region IV *to* region I by deposition of pure water ice from the E ring. If the rings were derived from typical Saturnian moon icy material, the direction of evolution then must have been *from* region IV *to* region III. However, the ring material that lies in region IV is the C ring and Cassini Division material, which is currently thought to have evolved *from* the much icier and redder "primordial" A and B ring material by meteoroid darkening. (A black and white version of this figure will appear in some formats. For the color version, please refer to the plate section.)

water ice from Enceladus, *via* the E ring see Figure 3.28). If the rings also shared a common parentage with Dione–Rhea–Janus, meteoroid bombardment would make the C ring and Cassini Division *even less icy and red*, moving them in the direction towards Iapetus and Phoebe in color plate 2. As noted

by Filacchione *et al.* (2012), only Prometheus shares the icy-red composition of the main rings.

Unfortunately, analogs of the presumably primordial A and B ring material are hard to find; comparably red outer solar system objects have extremely weak water ice bands (Cuzzi *et al.*, 2009, their figure 15.37). So, overall, the intrinsic scenarios may have a bit of an edge, if the extreme redness of the A/B rings can somehow be explained by some local processing acting to make them redder than Dione, Rhea, and Janus (Figure 3.28) *before* meteoroid pollution starts to evolve their composition in a fashion related to ther current optical depths. Intrinsic scenarios have a little more trouble disposing of some residual, ice-poor core, but in this connection, the recent discovery of what seems to be a large amount of buried silicate material in the middle of the C Ring (Zhang *et al.*, 2017) comes to mind. While nominally ascribing it to the remnants of an interloper rocky centaur, Zhang *et al.* (2017) also mention that it may be the remnants of a disrupted core. Perhaps such a core was separated from its stripped icy mantle by torques as suggested by Canup (2010), or collisions as suggested by Asphaug and Reufer (2013), but never made it into the planet before being turned to rubble.

3.11 PUZZLES AND CHALLENGES

In this section we summarize outstanding problems worthy of future attention.

Embedded moonlets Where are the missing moonlets, especially in the Cassini Division gaps? There may be enough Cassini imaging data in the archives for meaningful limits to be set, including in the outer gap where the so-called "charming" dusty ringlet appeared after Cassini's arrival at Saturn. What drives the apparently random orbital migration of the A ring propeller objects? Perhaps the required mass of responsible clumps can be inferred, and perhaps those clumps are associated with "straw" (Section 3.5.1).

What creates and maintains the C ring plateaus? It seems clear that a resonance with internal structure of the planet is responsible for the Maxwell Gap itself (Section 3.5.4). The plateaus are arrayed so symmetrically around that gap that a related cause may be implicated. These features also present odd particle size distributions (Cuzzi *et al.*, 2009; Colwell *et al.*, 2011a; Marouf *et al.*, 2011b); in particular, their significant optical depth increments above their surroundings are not echoed in their surface mass densities. They also reveal an unusual, canted, streaky structure in rare images having < 1 km resolution (unpublished results of JNC).

The B ring structure remains unexplained in general The pervasive B ring "irregular" structure has, so far, no established explanation, although there are hints that ballistic transport might play a role (see Chapter 9 for a review). So-called "viscous overstabilities" (Schmidt *et al.*, 2009) are generally thought to manifest only on much shorter radial lengthscales. Also, there are many examples in the B ring of extremely sharp radial transitions between opaque and semi-opaque regions – not between opaque regions and cleared gaps. No hypotheses for these transitions have been advanced. The inner B ring edge (and the similar inner A ring edge) have been explained by ballistic transport, based on assumptions that the optical depth is a good marker for surface mass density, but that seems not to be the case at least across the inner A ring edge. Finally, what is the mass of the B ring? If things continue to go as planned, it will be measured accurately during Cassini's Grand Finale orbits.

How does the F ring remain stable? The ring is embedded in a region of strong orbital chaos due primarily to Prometheus. Some recent work is suggestive, even if as yet unpublished and resting partly on a not-entirely-accepted concept of "antiresonance" (Section 3.5.6; Cuzzi *et al.*, 2014b; see also Chapter 13), but there remains no explanation as to how the true F ring core, apparently composed of discontinuous segments, maintains a common apse.

What is the mysterious red constituent? Models of recent Hubble Space Telescope Imaging Spectrometer (STIS) data, and the prevalence of organic materials throughout the Saturn system, suggest it is some organic material. Looked at more closely, discrepancies emerge as to whether the organic material is more aliphatic or more aromatic. Is there any way to change the composition, and its reddening potential, *in situ* by some chemical process after or during emplacement of the ring material but before meteoroid pollution begins? A high priority goal of the Grand Finale orbits is for CDA and/or INMS to measure the composition of the rings' non-icy material directly. Still, remote observations and their analyses will be required to compare properties with the icy moons, and understand radial variations.

Photometric modeling To interpret remotely sensed data in terms of composition, a battery of modeling must be applied and not all of these models are quantitatively reliable. So-called "classical" or many-particle-thick models are known to have systematic errors in connecting particle albedo and ring optical depth to the observed brightness. Some understanding of how to allow for this is emerging. Moreover, a possible role of within-surface shadowing has recently been noted that might change estimates of the "neutral absorber" abundance drastically. The correction associated with this effect is determined only by the particle phase function, which can best be properly isolated and determined using nonclassical photometric models. "Saturnshine" can contribute anomalous color to the rings in certain geometries and should be corrected for or avoided.

Passive microwave and active radar observations Groundbased radar observations launched the modern study of Saturn's rings in the 1970s. Unfortunately, *all* the modeling of those observations was based on classical "doubling" multiple scattering models which cannot properly allow for closely spaced particles, and worse yet, neglected the "coherent backscattering" effect to which a radar observation is intrinsically subject. Since all of our estimates of the bulk content of nonicy material (probably silicates) is based on these observations and analyses, a critical goal for future study (when computational power allows it) is to apply closely packed and/or coherent backscattering models to analyze all the groundbased and spacebased microwave and/or radar observations. In the Grand Finale orbits, Cassini will obtain unique radar radial profiles with several-hundred-meter resolution, but as of this writing we have no appropriate quantitative models to use for their analysis.

Origin and evolution modeling The advantage of intrinsic parentage for the rings motivates continued, in-depth modeling of the origin of icy satellite systems in general, a field in its infancy with many similarities to the larger problem of planetary formation in the circumsolar disk, but complicated by very short timescales and vigorous dynamical evolution. Models of ring evolution under meteoroid bombardment and ballistic transport will continue to be of central importance, especially if the meteoroid flux turns out to be comparable to that which was estimated prior to Cassini. Of special importance is understanding the ejecta yield, and distribution of mass, velocity, and direction. These properties must be determined due to both "cratering" impacts by regolith-sized grains, and disruptive impacts, as well as how outcomes vary with, *eg.* surface porosity.

Old or young rings? The meteoroid mass flux is absolutely fundamental, but at the time of this writing, its uncertainties are too large to distinguish between 0.5 Gyr and 4.5 Gyr old rings. By the end of the Cassini mission, one expects that the mass flux *and* the ring mass should have become well enough determined to answer the question of ring "exposure age", with some remaining uncertainty dominated by model parameters. Meanwhile, other clues should be explored regarding the age and parentage of the rings, including crater size and spatial distributions on the icy moon surfaces, and the controversial role of Saturn's tidal Q (Lainey *et al.*, 2017; Ćuk *et al.*, 2016). Perhaps we can learn something about Saturn's interior, related to Q, from newly discovered waves in the C ring. Some thought could be devoted to local evolutionary processes by which the ring material could become more red than local icy moons from which it might have derived.

ACKNOWLEDGEMENTS

JNC was supported by his IDS grant from the Cassini project. GF acknowledges the financial support from INAF-IAPS and ASI-Italian Space Agency. EAM was supported by his Radio Science Team Member grant from the Cassini Project. We thank the hundreds of JPL project staff for their dedication in making Cassini NASA's most successful interplanetary mission to date. We thank M. Ciarniello, M.Ćuk, C. Murray, and Z. Zhang for material in advance of publication, M. Tiscareno for a thorough editorial review, and P. Estrada, T. Bradley, E. Deau, M. Hedman, C. Murray, and A. Hendrix for helpful conversations and supporting materials.

REFERENCES

Albers, N., Sremčević, M., Colwell, J. E., and Esposito, L. W. 2012. Saturn's F ring as seen by Cassini UVIS: Kinematics and statistics. *Icarus*, **217**, 367–388.

Alexander, A. F. O. 1962. *The Planet Saturn: a History of Observation, Theory, and Discovery.* Newyork, Macmillan.

Asphaug, E., and Reufer, A. 2013. Late origin of the Saturn system. *Icarus*, **223**, 544–565.

Attree, N. O., Murray, C. D., Cooper, N. J., and Williams, G. A. 2012. Detection of low-velocity collisions in Saturn's F Ring. *Astrophys. J. Lett.*, **755**, L27.

Attree, N. O., Murray, C. D., Williams, G. A., and Cooper, N. J. 2014. A survey of low-velocity collisional features in Saturn's F ring. *Icarus*, **227**, 56–66.

Baillié, K., Colwell, J. E., Lissauer, J. J., Esposito, L. W., and Sremčević, M. 2011. Waves in Cassini UVIS stellar occultations. 2. The C ring. *Icarus*, **216**, 292–308.

Baillié, K., Colwell, J. E., Esposito, L. W., and Lewis, M. C. 2013. Meter-sized moonlet population in Saturn's C ring and Cassini Division. *Astron. J.*, **145**, 171.

Becker, T. M., Colwell, J. E., Esposito, L. W., and Bratcher, A. D. 2016. Characterizing the particle size distribution of Saturn's A ring with Cassini UVIS occultation data. *Icarus*, **279**, 20–35.

Beurle, K., Murray, C. D., Williams, G. A., *et al.* 2010. Direct evidence for gravitational instability and moonlet formation in Saturn's rings. *Astrophys. J. Lett.*, **718**, L176–L180.

Bobrov, M. S. 1970. *The Rings of Saturn.* Moskva, Nauka.

Bodrova, A., Schmidt, J., Spahn, F., and Brilliantov, N. 2012. Adhesion and collisional release of particles in dense planetary rings. *Icarus*, **218**, 60–68.

Boduch, P., da Silveira, E. F., Domaracka, A., *et al.* 2011. Production of oxidants by ion bombardment of icy moons in the outer solar system. *Advances in Astronomy*, **2011**, 327641.

Borderies, N., Goldreich, P., and Tremaine, S. 1985. A granular flow model for dense planetary rings. *Icarus*, **63**, 406–420.

Bosh, A. S., Olkin, C. B., French, R. G., and Nicholson, P. D. 2002. Saturn's F ring: Kinematics and particle sizes from stellar occultation studies. *Icarus*, **157**, 57–75.

Bradley, E. T., Colwell, J. E., Esposito, L. W., *et al.* 2010. Far ultraviolet spectral properties of Saturn's rings from Cassini UVIS. *Icarus*, **206**, 458–466.

Bradley, E. T., Colwell, J. E., and Esposito, L. W. 2013. Scattering properties of Saturn's rings in the far ultraviolet from Cassini UVIS spectra. *Icarus*, **225**, 726–739.

Brilliantov, N., Krapivsky, P., Bodrova, A., *et al.* 2013. Size distribution of particles in Saturn's rings from aggregation and fragmentation. *ArXiv e-prints*, Feb.

Bromley, B. C., and Kenyon, S. J. 2013. Migration of small moons in Saturn's rings. *Astrophys. J.*, **764**, 192.

Brooks, S. M., Esposito, L. W., Showalter, M. R., and Throop, H. B. 2004. The size distribution of Jupiter's main ring from Galileo imaging and spectroscopy. *Icarus*, **170**, 35–57.

Burns, J. A., Showalter, M. R., and Morfill, G. E. 1984. The ethereal rings of Jupiter and Saturn. Pages 200–272 of: Greenberg, R., and Brahic, A. (eds.), *IAU Colloq. 75: Planetary Rings*.

Burns, J. A., Simonelli, D. P., Showalter, M. R., *et al.* 2004. *Jupiter's Ring-Moon System*. Pages 241–262.

Canup, R. M. 2010. Origin of Saturn's rings and inner moons by mass removal from a lost Titan-sized satellite. *Nature*, **468**, 943–946.

Canup, R. M., and Esposito, L. W. 1995. Accretion in the Roche zone: Coexistence of rings and ring moons. *Icarus*, **113**, 331–352.

Canup, R. M., and Ward, W. R. 2002. Formation of the Galilean satellites: Conditions of accretion. *Astron. J.*, **124**, 3404–3423.

Canup, R. M., and Ward, W. R. 2006. A common mass scaling for satellite systems of gaseous planets. *Nature*, **441**, 834–839.

Caudal, G. V. 2013. The role of tidal torques on the evolution of the system of Saturn's co-orbital satellites Janus and Epimetheus. *Icarus*, **223**, 733–740.

Chandrasekhar, S. 1960. *Radiative Transfer*. Newyork, Dover,

Charnoz, S. 2009. Physical collisions of moonlets and clumps with the Saturn's F-ring core. *Icarus*, **201**, 191–197.

Charnoz, S., Porco, C. C., Déau, E., *et al.* 2005. Cassini discovers a kinematic spiral ring around Saturn. *Science*, **310**, 1300–1304.

Charnoz, S., Dones, L., Esposito, L. W., Estrada, P. R., and Hedman, M. M. 2009. Origin and evolution of Saturn's ring system.

Page 537 of: Dougherty, M. K., Esposito, L. W., and Krimigis, S. M. (eds.), *Saturn From Cassini-Huygens*. Springer Science+Business Media B.V.

Charnoz, S., Salmon, J., and Crida, A. 2010. The recent formation of Saturn's moonlets from viscous spreading of the main rings. *Nature*, **465**, 752–754.

Christon, S. P., Hamilton, D. C., Plane, J. M. C., *et al.* 2015. Discovery of suprathermal Fe^{+} in Saturn's magnetosphere. *Journal of Geophysical Research (Space Physics)*, **120**, 2720–2738.

Ciarniello, M., Capaccioni, F., Filacchione, G., *et al.* 2011. Hapke modeling of Rhea surface properties through Cassini-VIMS spectra. *Icarus*, **214**, 541–555.

Ciarniello, M., Filacchione, G., Capaccioni, F., *et al.* 2016, in review. Cassini-VIMS observations of Saturn's main rings: II. A spectrophotometric study by means of Monte Carlo ray-tracing and Hapke's theory. *Icarus*.

Clark, R. N., Pearson, N., Takir, D., *et al.* 2012a. Nano-iron on outer solar system satellites, implications for space weathering. *AGU Fall Meeting Abstracts*, Dec., B5.

Clark, R. N., Cruikshank, D. P., Jaumann, R., *et al.* 2012b. The surface composition of Iapetus: Mapping results from Cassini VIMS. *Icarus*, **218**, 831–860.

Colwell, J., Jerousek, R., Nicholson, P., *et al.* 2014. Abundance of small particles in Saturn's rings from Cassini UVIS and VIMS stellar occultations. Page 2479 of: *EGU General Assembly Conference Abstracts*. EGU General Assembly Conference Abstracts, vol. 16.

Colwell, J. E. 1994. The disruption of planetary satellites and the creation of planetary rings. *Planet. Sp. Sci.*, **42**, 1139–1149.

Colwell, J. E., and Esposito, L. W. 1990a. A model of dust production in the Neptune ring system. *Geophys. Res. Lett.*, **17**, 1741–1744.

Colwell, J. E., and Esposito, L. W. 1990b. A numerical model of the Uranian dust rings. *Icarus*, **86**, 530–560.

Colwell, J. E., and Esposito, L. W. 1992. Origins of the rings of Uranus and Neptune. I – Statistics of satellite disruptions. *J. Geophys. Res.*, **97**, 10227.

Colwell, J. E., Esposito, L. W., and Sremčević, M. 2006. Self-gravity wakes in Saturn's A ring measured by stellar occultations from Cassini. *Geophys. Res. Lett.*, **33**, 7201.

Colwell, J. E., Esposito, L. W., Sremčević, M., Stewart, G. R., and McClintock, W. E. 2007. Self-gravity wakes and radial structure of Saturn's B ring. *Icarus*, **190**, 127–144.

Colwell, J. E., Nicholson, P. D., Tiscareno, M. S., *et al.* 2009. The structure of Saturn's rings. Page 375 of Dougherby, M. K., Esposito, L. W., and Krimigis, S. M. (eds.) *Saturn From Cassini-Huygens*. Springer Science+Business Media B.V.

Colwell, J. E., Esposito, L. W., Jerousek, R. G., *et al.* 2010. Cassini UVIS Stellar occultation observations of Saturn's rings. *Astron. J.*, **140**, 1569–1578.

Colwell, J. E., Esposito, L. W., Jerousek, R. G., *et al.* 2011a. More weird size distributions in the C ring plateaus. In: Burns, J. A. (ed.), *Planetary Rings Summer Workshop, Cornell, June 2011*.

Colwell, J. E., Cooney, J., and Esposito, L. W. 2011b. Properties of Saturn's rings from stellar occultation statistics. *AGU Fall Meeting Abstracts*, Dec.

Colwell, J. E., Cooney, J. H., Esposito, L. W., and Sremcevic, M. 2012. Particle sizes and small-scale structure in Saturn's rings from stellar occultation statistics. Page 501.05 of: *AAS/Division for Planetary Sciences Meeting Abstracts*. AAS/Division for Planetary Sciences Meeting Abstracts, vol. 44.

Colwell, J. E., Cooney, J., Esposito, L. W., and Sremcevic, M. 2013. Saturn's rings particle and clump sizes from Cassini UVIS occultation statistics (Invited). *AGU Fall Meeting Abstracts*, Dec.

Connerney, J. 2013. Solar system: Saturn's ring rain. *Nature*, **496**, 178–179.

Connerney, J. E. P., and Waite, J. H. 1984. New model of Saturn's ionosphere with an influx of water from the rings. *Nature*, **312**, 136–138.

Cooke, M. L. 1991. *Saturn's rings: Photometric studies of the C Ring and radial variation in the Keeler Gap*. Ph.D. thesis, Cornell University, Ithaca, NY.

Cooke, M. L., Nicholson, P. D., and Showalter, M. R. 1991. Photometric studies of Saturn's C-ring. Page 1180 of: *Bulletin of the American Astronomical Society*. Bulletin of the American Astronomical Society, vol. 23.

Cooper, N. J., and Murray, C. D. 2004. Dynamical influences on the orbits of Prometheus and Pandora. *Astron. J.*, **127**, 1204–1217.

Cooper, N. J., Murray, C. D., Evans, M. W., *et al.* 2008. Astrometry and dynamics of Anthe (S/2007 S 4), a new satellite of Saturn. *Icarus*, **195**, 765–777.

Cooper, N. J., Murray, C. D., and Williams, G. A. 2013. Local variability in the orbit of Saturn's F ring. *Astron. J.*, **145**, 161.

Cooper, N. J., Renner, S., Murray, C. D., and Evans, M. W. 2015. Saturn's inner satellites: Orbits, masses, and the chaotic motion of atlas from new Cassini imaging observations. *Astron. J.*, **149**, 27.

Crida, A., Papaloizou, J. C. B., Rein, H., Charnoz, S., and Salmon, J. 2010. Migration of a moonlet in a ring of solid particles: Theory and application to Saturn's propellers. *Astron. J.*, **140**, 944–953.

Cruikshank, D. P., Dalle Ore, C. M., Clark, R. N., and Pendleton, Y. J. 2014. Aromatic and aliphatic organic materials on Iapetus: Analysis of Cassini VIMS data. *Icarus*, **233**, 306–315.

Ćuk, M., Dones, L., and Nesvorný, D. 2016. Dynamical evidence for a late formation of Saturn's moons. *Astrophys. J.*, **820**, 97.

Cuzzi, J., Clark, R., Filacchione, G., *et al.* 2009. Ring particle composition and size distribution. Page 459 of Dougherby, M. K., Esposito, L. W., and Krimigis, S. M. (eds.) *Saturn From Cassini-Huygens*. Springer Science+Business Media B.V.

Cuzzi, J. N. 1985. Rings of Uranus – Not so thick, not so black. *Icarus*, **63**, 312–316.

Cuzzi, J. N., and Estrada, P. R. 1998. Compositional evolution of Saturn's rings due to meteoroid bombardment. *Icarus*, **132**, 1–35.

Cuzzi, J. N., and Pollack, J. B. 1978. Saturn's rings: Particle composition and size distribution as constrained by microwave observations. I – Radar observations. *Icarus*, **33**, 233–262.

Cuzzi, J. N., Pollack, J. B., and Summers, A. L. 1980. Saturn's rings – Particle composition and size distribution as constrained by observations at microwave wavelengths. II – Radio interferometric observations. *Icarus*, **44**, 683–705.

Cuzzi, J. N., Lissauer, J. J., and Shu, F. H. 1981. Density waves in Saturn's rings. *Nature*, **292**, 703–707.

Cuzzi, J. N., Lissauer, J. J., Esposito, L. W., *et al.* 1984. Saturn's rings – Properties and processes. Pages 73–199 of: Greenberg, R., and Brahic, A. (eds.), *IAU Colloq. 75: Planetary Rings*.

Cuzzi, J. N., French, R. G., and Dones, L. 2002. HST multicolor (255–1042 nm) photometry of Saturn's main rings. I: radial profiles, phase and opening angle variations, and regional spectra. *Icarus*, **158**, 199–223.

Cuzzi, J. N., Burns, J. A., Charnoz, S., *et al.* 2010. An evolving view of Saturn's dynamic rings. *Science*, **327**, 1470.

Cuzzi, J. N., Whizin, A. D., Hogan, R. C., *et al.* 2014a. Saturn's F Ring core: Calm in the midst of chaos. *Icarus*, **232**, 157–175.

Cuzzi, J. N., Marouf, E. A., French, R. C., and Jacobson, R. 2014b. Saturn's F ring core: Calm in the midst of chaos; Part 2. In: Esposito, L. W. (ed), *Planetary Rings Summer Workshop, Boulder, Colo, August 2014*.

Cuzzi, J. N., Chambers, L., and Hendrix, A. R. 2016. Rough surfaces: Is the dark stuff just shadow? *Icarus, in press*.

Cuzzi, J. N., French, R. C., and Hendrix, A. R. 2017. HST-STIS observations of Saturn's rings, and the composition of the UV absorber. *Icarus, in preparation*.

D'Aversa, E., Bellucci, G., Nicholson, P. D., *et al.* 2010. The spectrum of a Saturn ring spoke from Cassini/VIMS. *GRL*, **37**, 1203.

Davis, D. R., Weidenschilling, S. J., Chapman, C. R., and Greenberg, R. 1984. Saturn ring particles as dynamic ephemeral bodies. *Science*, **224**, 744–747.

Déau, E. 2012. Variations of the apparent angular size of the Sun across the entire Solar System: Implications for planetary opposition surges. *J. Spect. Quant. Rad. Transf.,* **113**, 1476–1487.

Déau, E. 2015. The opposition effect in Saturn's main rings as seen by Cassini ISS: 2. Constraints on the ring particles and their regolith with analytical radiative transfer models. *Icarus*, **253**, 311–345.

Déau, E., Flandes, A., Spilker, L. J., and Petazzoni, J. 2013. Reanalysis of previous laboratory phase curves: 1. Variations of the opposition effect morphology with the textural properties, and an application to planetary surfaces. *Icarus*, **226**, 1465–1488.

Dones, H. C., Agnor, C. B., and Asphaug, E. 2008. Formation of Saturn's Rings by Tidal Disruption of a Centaur. Page 18.07 of: *AAS/Division of Dynamical Astronomy Meeting #39*. AAS/Division of Dynamical Astronomy Meeting, vol. 39.

Dones, L. 1991. A recent cometary origin for Saturn's rings? *Icarus*, **92**, 194–203.

Dones, L., Chapman, C. R., McKinnon, W. B., *et al.* 2009. Icy satellites of Saturn: Impact cratering and age determination. Page 613 of Dougherby, M. K., Esposito, L. W., and Krimigis, S. M. (eds.) *Saturn From Cassini-Huygens*. Springer Science+Business Media B.V.

Doyle, L. R., and Grün, E. 1990. Radiative transfer modeling constraints on the size of the spoke particles in Saturn's rings. *Icarus*, **85**, 168–190.

Doyle, L. R., Dones, L., and Cuzzi, J. N. 1989. Radiative transfer modeling of Saturn's outer B ring. *Icarus*, **80**, 104–135.

Durisen, R. H., Bode, P. W., Cuzzi, J. N., Cederbloom, S. E., and Murphy, B. W. 1992. Ballistic transport in planetary ring systems due to particle erosion mechanisms. II – Theoretical models for Saturn's A- and B-ring inner edges. *Icarus*, **100**, 364–393.

Durisen, R. H., Bode, P. W., Dyck, S. G., *et al.* 1996. Ballistic transport in planetary ring systems due to particle erosion mechanisms. III. Torques and mass loading by meteoroid impacts. *Icarus*, **124**, 220–236.

El Moutamid, M., Nicholson, P. D., French, R. G., *et al.* 2016. How Janus' orbital swap affects the edge of Saturn's A ring? *Icarus*, **279**, 125–140.

Elliott, J. P., and Esposito, L. W. 2011. Regolith depth growth on an icy body orbiting Saturn and evolution of bidirectional reflectance due to surface composition changes. *Icarus*, **212**, 268–274.

Elliott, J. P., and Esposito, L. W. 2015. Evolution of regolith depth and fractional pollution of Saturn's rings. Page #218.13 of: *AAS/Division for Planetary Sciences Meeting Abstracts*. AAS/Division for Planetary Sciences Meeting Abstracts, vol. 47.

Elrod, M. K., Tseng, W.-L., Woodson, A. K., and Johnson, R. E. 2014. Seasonal and radial trends in Saturn's thermal plasma between the main rings and Enceladus. *Icarus*, **242**, 130–137.

Epstein, E. E., Janssen, M. A., Cuzzi, J. N., Fogarty, W. G., and Mottmann, J. 1980. Saturn's rings – 3-mm observations and derived properties. *Icarus*, **41**, 103–118.

Esposito, L. W. 1986. Structure and evolution of Saturn's rings. *Icarus*, **67**, 345–357.

Esposito, L. W. 2010. Composition, structure, dynamics, and evolution of Saturn's rings. *Annual Review of Earth and Planetary Sciences*, **38**, 383–410.

Esposito, L. W. 2014. *Planetary Rings: A Post-Equinox View*. Cambridge, UK, Cambridge Planetary Science.

Esposito, L. W., Cuzzi, J. N., Holberg, J. B., *et al.* 1984. *Saturn's Rings – Structure, Dynamics, and Particle Properties*. Pages 463–545.

Esposito, L. W., Albers, N., Meinke, B. K., *et al.* 2012. A predator-prey model for moon-triggered clumping in Saturn's rings. *Icarus*, **217**, 103–114.

Estrada, P. R., and Mosqueira, I. 2006. A gas-poor planetesimal capture model for the formation of giant planet satellite systems. *Icarus*, **181**, 486–509.

Estrada, P. R., Cuzzi, J. N., and Showalter, M. R. 2003. Voyager color photometry of Saturn's main rings: a correction. *Icarus*, **166**, 212–222.

Estrada, P. R., Durisen, R. H., Cuzzi, J. N., and Morgan, D. A. 2015a. Combined structural and compositional evolution of planetary rings due to micrometeoroid impacts and ballistic transport. *Icarus*, **252**, 415–439.

Estrada, P. R., Durisen, R. H., Cuzzi, J. N., and Morgan, D. A. 2015b. Combined structural and compositional evolution of planetary rings due to micrometeoroid impacts and ballistic transport. *Icarus*, **252**, 415–439.

Farmer, A. J., and Goldreich, P. 2006. Understanding the behavior of Prometheus and Pandora. *Icarus*, **180**, 403–411.

Ferrari, C., and Reffet, E. 2013. The dark side of Saturn's B ring: Seasons as clues to its structure. *Icarus*, **223**, 28–39.

Filacchione, G., Capaccioni, F., Ciarniello, M., *et al.* 2012. Saturn's icy satellites and rings investigated by Cassini-VIMS: III – Radial compositional variability. *Icarus*, **220**, 1064–1096.

Filacchione, G., Capaccioni, F., Clark, R. N., *et al.* 2013. The radial distribution of water ice and chromophores across Saturn's system. *Astrophys. J.*, **766**, 76.

Filacchione, G., Ciarniello, M., Capaccioni, F., *et al.* 2014. Cassini-VIMS observations of Saturn's main rings: I. Spectral properties and temperature radial profiles variability with phase angle and elevation. *Icarus*, **241**, 45–65.

Flandes, A., Spilker, L., Morishima, R., *et al.* 2010. Brightness of Saturn's rings with decreasing solar elevation. *Planet. Sp. Sci.*, **58**, 1758–1765.

French, R. G., and Nicholson, P. D. 2000. Saturn's rings II. Particle sizes inferred from stellar occultation data. *Icarus*, **145**, 502–523.

French, R. G., Nicholson, P. D., Porco, C. C., and Marouf, E. A. 1991. *Dynamics and Structure of the Uranian Rings*. Pages 327–409.

French, R. G., McGhee, C. A., Dones, L., and Lissauer, J. J. 2003. Saturn's wayward shepherds: the peregrinations of Prometheus and Pandora. *Icarus*, **162**, 143–170.

French, R. G., Salo, H., McGhee, C. A., and Dones, L. 2007a. HST observations of azimuthal asymmetry in Saturn's rings. *Icarus*, **189**, 493–522.

French, R. G., Verbiscer, A., Salo, H., McGhee, C., and Dones, L. 2007b. Saturn's rings at true opposition. *Pub. Ast. Soc. Pacific*, **119**, 623–642.

French, R. G., Marouf, E. A., Rappaport, N. J., and McGhee, C. A. 2010. Occultation observations of Saturn's B ring and Cassini Division. *Astron. J.*, **139**, 1649–1667.

French, R. G., Nicholson, P. D., Hedman, M. M., *et al.* 2016. Deciphering the embedded wave in Saturn's Maxwell ringlet. *Icarus*, **279**, 62–77.

French, R. S., Showalter, M. R., Sfair, R., *et al.* 2012. The brightening of Saturn's F ring. *Icarus*, **219**, 181–193.

French, R. S., Hicks, S. K., Showalter, M. R., Antonsen, A. K., and Packard, D. R. 2014. Analysis of clumps in Saturn's F ring from Voyager and Cassini. *Icarus*, **241**, 200–220.

Fuller, J. 2014. Saturn ring seismology: Evidence for stable stratification in the deep interior of Saturn. *Icarus*, **242**, 283–296.

Fuller, J. 2015. Saturn ring seismology: How ring dynamics reveal the internal structure of the planet. Page #200.03 of: *AAS/Division of Dynamical Astronomy Meeting*. AAS/Division of Dynamical Astronomy Meeting, vol. 46.

Gehrels, T., Baker, L. R., Beshore, E., *et al.* 1980. Imaging photopolarimeter on Pioneer Saturn. *Science*, **207**, 434–439.

Goldreich, P., and Rappaport, N. 2003. Origin of chaos in the Prometheus–Pandora system. *Icarus*, **166**, 320–327.

Goldreich, P., and Tremaine, S. 1982. The dynamics of planetary rings. *Ann. Rev. Astron. Astrophys.*, **20**, 249–283.

Goldstein, R. M., and Morris, G. A. 1973. Radar observations of the rings of Saturn. *Icarus*, **20**, 260–262.

Goldstein, R. M., Green, R. R., Pettengill, G. H., and Campbell, D. B. 1977. The rings of Saturn – Two-frequency radar observations. *Icarus*, **30**, 104–110.

Griv, E. 2011. Formation of moonlets in Saturn's rings: The role of the constructive interference of Lin-Shu-type circular and spiral density waves. *Astrophys. J.*, **733**, 43.

Grün, E., Zook, H. A., Fechtig, H., and Giese, R. H. 1985. Collisional balance of the meteoritic complex. *Icarus*, **62**, 244–272.

Grün, E., Goertz, C. K., Morfill, G. E., and Havnes, O. 1992. Statistics of Saturn's spokes. *Icarus*, **99**, 191–201.

Gurnett, D., Kurth, W., Hospodarsky, G., Persoon, A., and Cuzzi, J. 2004. Evidence of meteoroid impacts on the rings from Cassini plasma wave measurements. *AGU Fall Meeting Abstracts*, Dec.

Hahn, J. M. 2006. Small shepherd satellites in Saturn's Encke Gap? In: Mackwell, S., and Stansbery, E. (eds.), *37th Annual Lunar and Planetary Science Conference*. Lunar and Planetary Inst. Technical Report, vol. 37.

Hahn, J. M., and Spitale, J. N. 2013. An N-body integrator for gravitating planetary rings, and the outer edge of Saturn's B ring. *Astrophys. J.*, **772**, 122.

Han, D., Poppe, A. R., Piquette, M., Grün, E., and Horányi, M. 2011. Constraints on dust production in the Edgeworth–Kuiper Belt from Pioneer 10 and New Horizons measurements. *Geophys. Res. Lett.*, **38**, L24102.

Hapke, B. 1993. *Theory of Reflectance and Emittance Spectroscopy*. Cambridge, UK, Cambridge University Press.

Harbison, R. A., Nicholson, P. D., and Hedman, M. M. 2013. The smallest particles in Saturn's A and C rings. *Icarus*, **226**, 1225–1240.

Harris, A. W. 1984. The origin and evolution of planetary rings. Pages 641–659 of: Greenberg, R., and Brahic, A. (eds.), *IAU Colloq. 75: Planetary Rings*.

Hedman, M. M. 2015. Why are dense planetary rings only found between 8 AU and 20 AU? *Astrophys. J. Lett.*, **801**, L33.

Hedman, M. M., and Nicholson, P. D. 2013. Kronoseismology: Using density waves in Saturn's C ring to probe the planet's interior. *Astron. J.*, **146**, 12.

Hedman, M. M., and Nicholson, P. D. 2014. More Kronoseismology with Saturn's rings. *M.N.R.A.S.*, **444**, 1369–1388.

Hedman, M. M., and Nicholson, P. D. 2015. How massive is Saturn's B ring? Clues from cryptic density waves. Page #200.05 of: *AAS/Division of Dynamical Astronomy Meeting*. AAS/Division of Dynamical Astronomy Meeting, vol. 46.

Hedman, M. M., and Showalter, M. R. 2016. A new pattern in Saturn's D ring created in late 2011. *Icarus*, **279**, 155–165.

Hedman, M. M., and Stark, C. C. 2015. Saturn's G and D rings provide nearly complete measured scattering phase functions of nearby debris disks. *Astrophys. J.*, **811**, 67.

Hedman, M. M., Burns, J. A., Showalter, M. R., *et al.* 2007a. Saturn's dynamic D ring. *Icarus*, **188**, 89–107.

Hedman, M. M., Nicholson, P. D., Salo, H., *et al.* 2007b. Self-gravity wake structures in Saturn's A ring revealed by Cassini VIMS. *Astron. J.*, **133**, 2624–2629.

Hedman, M. M., Nicholson, P. D., Salo, H., *et al.* 2007c. Self-gravity wake structures in Saturn's A ring revealed by Cassini VIMS. *Astron. J.*, **133**, 2624–2629.

Hedman, M. M., Burns, J. A., Tiscareno, M. S., *et al.* 2007d. The source of Saturn's G ring. *Science*, **317**, 653.

Hedman, M. M., Murray, C. D., Cooper, N. J., *et al.* 2009. Three tenuous rings/arcs for three tiny moons. *Icarus*, **199**, 378–386.

Hedman, M. M., Cooper, N. J., Murray, C. D., *et al.* 2010a. Aegaeon (Saturn LIII), a G-ring object. *Icarus*, **207**, 433–447.

Hedman, M. M., Nicholson, P. D., Baines, K. H., *et al.* 2010b. The architecture of the Cassini Division. *Astron. J.*, **139**, 228–251.

Hedman, M. M., Burt, J. A., Burns, J. A., and Tiscareno, M. S. 2010c. The shape and dynamics of a heliotropic dusty ringlet in the Cassini Division. *Icarus*, **210**, 284–297.

Hedman, M. M., Burns, J. A., Evans, M. W., Tiscareno, M. S., and Porco, C. C. 2011a. Saturn's curiously corrugated C ring. *Science*, **332**, 708.

Hedman, M. M., Nicholson, P. D., Showalter, M. R., *et al.* 2011b. The Christiansen Effect in Saturn's narrow dusty rings and the spectral identification of clumps in the F ring. *Icarus*, **215**, 695–711.

Hedman, M. M., Burns, J. A., Hamilton, D. P., and Showalter, M. R. 2012. The three-dimensional structure of Saturn's E ring. *Icarus*, **217**, 322–338.

Hedman, M. M., Nicholson, P. D., Cuzzi, J. N., *et al.* 2013a. Connections between spectra and structure in Saturn's main rings based on Cassini VIMS data. *Icarus*, **223**, 105–130.

Hedman, M. M., Burns, J. A., Hamilton, D. P., and Showalter, M. R. 2013b. Of horseshoes and heliotropes: Dynamics of dust in the Encke Gap. *Icarus*, **223**, 252–276.

Hedman, M. M., Burt, J. A., Burns, J. A., and Showalter, M. R. 2014. Non-circular features in Saturn's D ring: D68. *Icarus*, **233**, 147–162.

Hedman, M. M., Burns, J. A., and Showalter, M. R. 2015. Corrugations and eccentric spirals in Saturn's D ring: New insights into what happened at Saturn in 1983. *Icarus*, **248**, 137–161.

Hirata, N., and Miyamoto, H. 2012. Dust levitation as a major resurfacing process on the surface of a saturnian icy satellite, Atlas. *Icarus*, **220**, 106–113.

Hoffmann, H., Seiß, M., and Spahn, F. 2013. Vertical relaxation of a moonlet propeller in Saturn's A ring. *Astrophys. J. Lett.*, **765**, L4.

Hoffmann, H., Seiß, M., Salo, H., and Spahn, F. 2015. Vertical structures induced by embedded moonlets in Saturn's rings. *Icarus*, **252**, 400–414.

Horányi, M., Burns, J. A., Hedman, M. M., Jones, G. H., and Kempf, S. 2009. Diffuse rings. Page 511 of Dougherby, M. K., Esposito, L. W., and Krimigis, S. M. (eds.) *Saturn From Cassini-Huygens*. Springer Science+Business Media B.V.

Horn, L. J., and Cuzzi, J. N. 1996. Characteristic Wavelengths of Irregular Structure in Saturn's B ring. *Icarus*, **119**, 285–310.

Hsu, H.-W., Postberg, F., Kempf, S., *et al.* 2011. Stream particles as the probe of the dust-plasma-magnetosphere interaction at Saturn. *Journal of Geophysical Research (Space Physics)*, **116**, A09215.

Hsu, S., Tseng, W. L., Juhasz, A., Kempf, S., and Horanyi, M. 2014. Photolysis and radiolysis of ice in Saturn's E ring. *AGU Fall Meeting Abstracts*, Dec., B3993.

Hueso, R., Pérez-Hoyos, S., Sánchez-Lavega, A., *et al.* 2013. Impact flux on Jupiter: From superbolides to large-scale collisions. *Astron. Astrophys.*, **560**, A55.

Hyodo, R., and Ohtsuki, K. 2014. Collisional disruption of gravitational aggregates in the tidal environment. *Astrophys. J.*, **787**, 56.

Hyodo, R., Charnoz, S., Ohtsuki, K., and Genda, H. 2015. Physics of tidal disruption of big objects at the close encounter to Saturn. Page 218.10 of: *AAS/Division for Planetary Sciences Meeting Abstracts*. AAS/Division for Planetary Sciences Meeting Abstracts, vol. 47.

Imanaka, H., Khare, B. N., Elsila, J. E., *et al.* 2004. Laboratory experiments of Titan tholin formed in cold plasma at various pressures: implications for nitrogen-containing polycyclic aromatic compounds in Titan haze. *Icarus*, **168**, 344–366.

Imanaka, H., Cruikshank, D.P., Khare, B.N., and McKay, C.P. 2012. Optical constants of Titan tholins at mid-infrared wavelengths (2.5–25 μm) and the possible chemical nature of Titan's haze particles. *Icarus*, **218**, 247–261.

Jacobson, R. A., Spitale, J., Porco, C. C., *et al.* 2008. Revised orbits of Saturn's small inner satellites. *Astron. J.*, **135**, 261–263.

Jerousek, R. G., Colwell, J. E., Nicholson, P. D., *et al.* 2014. Particle size distribution in Saturn's C ring and Cassini Division from VIMS and UVIS stellar occultations. *AGU Fall Meeting Abstracts*, Dec.

Johnson, R. E., Luhmann, J. G., Tokar, R. L., *et al.* 2006. Production, ionization and redistribution of O_2 in Saturn's ring atmosphere. *Icarus*, **180**, 393–402.

Johnson, T. V., and Estrada, P. R. 2009. *Origin of the Saturn System*. Page 55.

Juhász, A., Horányi, M., and Morfill, G. E. 2007. Signatures of Enceladus in Saturn's E ring. *Geophys. Res. Lett.*, **34**, 9104.

Karkoschka, E. 1994. Spectrophotometry of the jovian planets and Titan at 300- to 1000-nm wavelength: The methane spectrum. *Icarus*, **111**, 174–192.

Kempf, S., Altobelli, N., Horanyi, M., and Srama, R. 2013. The mass flux of micrometeoroids into the Saturnian system. *AGU Fall Meeting Abstracts*, Dec.

Kempf, S., Altobelli, N., Horanyi, M., and Srama, R. 2014. The mass flux of micrometeoroids into the Saturn. Page 15324 of: *EGU General Assembly Conference Abstracts*. EGU General Assembly Conference Abstracts, vol. 16.

Lainey, V., Jacobson, R. A., Tajeddine, R., *et al.* 2017. New constraints on Saturn's interior from Cassini astrometric data. *Icarus*, **281**, 286–296.

Landgraf, M., Baggaley, W. J., Grün, E., Krüger, H., and Linkert, G. 2000. Aspects of the mass distribution of interstellar dust grains in the solar system from in situ measurements. *J. Geophys. Res.*, **105**, 10 343–10 352.

Latter, H. N., Rein, H., and Ogilvie, G. I. 2012. The gravitational instability of a stream of co-orbital particles. *M.N.R.A.S.*, **423**, 1267–1276.

Lawney, B. P., Jenkins, J. T., and Burns, J. A. 2012. Collisional features in a model of a planetary ring. *Icarus*, **220**, 383–391.

Leinhardt, Z. M., Ogilvie, G. I., Latter, H. N., and Kokubo, E. 2012. Tidal disruption of satellites and formation of narrow rings. *M.N.R.A.S.*, **424**, 1419–1431.

Liu, C.-M., and Ip, W.-H. 2014. A new pathway of Saturnian ring-ionosphere coupling via charged nanograins. *Astrophys. J.*, **786**, 34.

Longaretti, P.-Y. 1989. Saturn's main ring particle size distribution – an analytic approach. *Icarus*, **81**, 51–73.

Luhmann, J. G., Johnson, R. E., Tokar, R. L., Ledvina, S. A., and Cravens, T. E. 2006. A model of the ionosphere of Saturn's rings and its implications. *Icarus*, **181**, 465–474.

Madhusudhanan, P., Esposito, L., and Torres, P. 2016, in review. A combined dynamical and transport model for producing haloes at resonances in Saturn's rings. *Icarus*.

Marley, M. S. 2014. Saturn ring seismology: Looking beyond first order resonances. *Icarus*, **234**, 194–199.

Marley, M. S., and Porco, C. C. 1993. Planetary acoustic mode seismology – Saturn's rings. *Icarus*, **106**, 508.

Marouf, E., Wong, K., French, R., Rappaport, N. J., and McGhee, C. 2010a. Saturn's F-Ring Discontinuous core and orbit model. Page 6 of: *38th COSPAR Scientific Assembly*. COSPAR Meeting, vol. 38.

Marouf, E. A., Tyler, G. L., and Eshleman, V. R. 1982. Theory of radio occultation by Saturn's rings. *Icarus*, **49**, 161–193.

Marouf, E. A., Tyler, G. L., Zebker, H. A., Simpson, R. A., and Eshleman, V. R. 1983. Particle size distributions in Saturn's rings from Voyager 1 radio occultation. *Icarus*, **54**, 189–211.

Marouf, E. A., French, R., Rappaport, N., *et al.* 2008. Physical properties of Saturn's rings from Cassini radio occultations. Page 429 of: *AAS/Division for Planetary Sciences Meeting Abstracts #40*. Bulletin of the American Astronomical Society, vol. 40.

Marouf, E. A., Wong, K., French, R., Rappaport, N., and McGhee, C. 2010b. The discontinuous core of Saturn's F-ring and orbit model. Page 988 of: *AAS/Division for Planetary Sciences Meeting Abstracts #42*. Bulletin of the American Astronomical Society, vol. 42.

Marouf, E. A., French, R. G., Rappaport, N. J., *et al.* 2011a. Six centuries old spiral of vertical corrugations in Saturn's C-ring. *AGU Fall Meeting Abstracts*, Dec.

Marouf, E. A., French, R. G., Rappaport, N. J., *et al.* 2011b. Weird size distribution in the C Ring plateaus. In: Burns, J. A. (ed.), *Planetary Rings Summer Workshop, Cornell, June 2011*.

Marouf, E. A., Wong, K. K., French, R. G., and Rappaport, N. J. 2013. Particle Sizes in Saturn's Rings from Cassini Radio Occultations. *AGU Fall Meeting Abstracts*, Dec.

Marouf, E. A., Wong, K. K., French, R. G., Rappaport, N. J., and McGhee-French, C. A. 2014. Scattering by gravitational wakes in Saturn's A-ring and inference of wake sizes from multiple Cassini radio occultations. Page 402.03 of: *AAS/Division for Planetary Sciences Meeting Abstracts*. AAS/Division for Planetary Sciences Meeting Abstracts, vol. 46.

Mastrapa, R., Sandford, S.A., Roush, T.L., Cruikshank, D.P., and Dalle Ore, C. M. 2009. Optical constants of amorphous, crystalline H_2O ice: 2.5–22 μm. *Astrophys. J.*, **701**, 1347–1356.

McGhee, C. A., Nicholson, P. D., French, R. G., and Hall, K. J. 2001. HST Observations of Saturnian satellites during the 1995 ring plane crossings. *Icarus*, **152**, 282–315.

McGhee, C. A., French, R. G., Dones, L., *et al.* 2005. HST observations of spokes in Saturn's B ring. *Icarus*, **173**, 508–521.

Meinke, B. K., Esposito, L. W., Albers, N., and Sremčević, M. 2012. Classification of F ring features observed in Cassini UVIS occultations. *Icarus*, **218**, 545–554.

Mendis, D. A., Hill, J. R., Ip, W.-H., Goertz, C. K., and Gruen, E. 1984. *Electrodynamic Processes in the Ring System of Saturn*. Pages 546–589.

Michikoshi, S., and Kokubo, E. 2011. Formation of a propeller structure by a moonlet in a dense planetary ring. *Astrophys. J. Lett.*, **732**, L23.

Mitchell, C. J., Horányi, M., Havnes, O., and Porco, C. C. 2006. Saturn's spokes: Lost and found. *Science*, **311**, 1587–1589.

Mitchell, C. J., Porco, C. C., Dones, H. L., and Spitale, J. N. 2013. The behavior of spokes in Saturn's B ring. *Icarus*, **225**, 446–474.

Moore, L., O'Donoghue, J., Mueller-Wodarg, I., and Mendillo, M. 2013 (Oct.). Saturn's ring rain: Initial estimates of ring mass loss rates. Page 512.06 of: *AAS/Division for Planetary Sciences Meeting Abstracts*, vol. 45.

Moore, L., O'Donoghue, J., Müller-Wodarg, I., Galand, M., and Mendillo, M. 2015. Saturn ring rain: Model estimates of water influx into Saturn's atmosphere. *Icarus*, **245**, 355–366.

Morishima, R., Edgington, S. G., and Spilker, L. 2012. Regolith grain sizes of Saturn's rings inferred from Cassini-CIRS far-infrared spectra. *Icarus*, **221**, 888–899.

Morishima, R., Spilker, L., Brooks, S., Deau, E., and Pilorz, S. 2016. Incomplete cooling down of Saturn's A ring at solar equinox: Implication for seasonal thermal inertia and internal structure of ring particles. *Icarus*, **279**, 2–19.

Mosqueira, I., and Estrada, P. R. 2003a. Formation of the regular satellites of giant planets in an extended gaseous nebula I: subnebula model and accretion of satellites. *Icarus*, **163**, 198–231.

Mosqueira, I., and Estrada, P. R. 2003b. Formation of the regular satellites of giant planets in an extended gaseous nebula II: satellite migration and survival. *Icarus*, **163**, 232–255.

Mosqueira, I., Estrada, P. R., and Charnoz, S. 2010a. Deciphering the origin of the regular satellites of gaseous giants – Iapetus: The Rosetta ice-moon. *Icarus*, **207**, 448–460.

Mosqueira, I., Estrada, P., and Turrini, D. 2010b. Planetesimals and satellitesimals: formation of the satellite systems. *Sp. Sci. Revs.*, **153**, 431–446.

Murray, C. D., and Dermott, S. F. 1999. *Solar System Dynamics*. Cambridge, UK, Cambridge University Press.

Murray, C. D., Beurle, K., Cooper, N. J., *et al.* 2008. The determination of the structure of Saturn's F ring by nearby moonlets. *Nature*, **453**, 739–744.

Murray, C. D., Cooper, N. J., Williams, G. A., Attree, N. O., and Boyer, J. S. 2014. The discovery and dynamical evolution of an object at the outer edge of Saturn's A ring. *Icarus*, **236**, 165–168.

Nicholson, P. D., and Hedman, M. M. 2010a. Self-gravity wake parameters in Saturn's A and B rings. *Icarus*, **206**, 410–423.

Nicholson, P. D., and Hedman, M. M. 2010b. Self-gravity wake parameters in Saturn's A and B rings. *Icarus*, **206**, 410–423.

Nicholson, P. D., Hedman, M. M., Clark, R. N., *et al.* 2008. A close look at Saturn's rings with Cassini VIMS. *Icarus*, **193**, 182–212.

Nicholson, P. D., French, R. G., Hedman, M. M., *et al.* 2014a. Architecture of the Cassini Division revisited. Page #402.01 of: *AAS/Division of Dynamical Astronomy Meeting*. AAS/Division of Dynamical Astronomy Meeting, vol. 45.

Nicholson, P. D., French, R. G., Hedman, M. M., Marouf, E. A., and Colwell, J. E. 2014b. Noncircular features in Saturn's rings I: The edge of the B ring. *Icarus*, **227**, 152–175.

Nitter, T., Havnes, O., and Melandsø, F. 1998. Levitation and dynamics of charged dust in the photoelectron sheath above surfaces in space. *J. Geophys. Res.*, **103**, 6605–6620.

Northrop, T. G., and Hill, J. R. 1982. Stability of negatively charged dust grains in Saturn's ring plane. *J. Geophys. Res.*, **87**, 6045–6051.

Northrop, T. G., and Hill, J. R. 1983a. The adiabatic motion of charged dust grains in rotating magnetospheres. *J. Geophys. Res.*, **88**, 1–11.

Northrop, T. G., and Hill, J. R. 1983b. The inner edge of Saturn's B ring. *J. Geophys. Res.*, **88**, 6102–6108.

O'Donoghue, J., Stallard, T. S., Melin, H., *et al.* 2013. The domination of Saturn's low-latitude ionosphere by ring 'rain'. *Nature*, **496**, 193–195.

Ohtsuki, K. 2006. Rotation rate and velocity dispersion of planetary ring particles with size distribution II. Numerical simulation for gravitating particles. *Icarus*, **183**, 384–395.

Ohtsuki, K., Yasui, Y., and Daisaka, H. 2013. Accretion rates of moonlets embedded in circumplanetary particle disks. *Astron. J.*, **146**, 25.

Orton, G. S., Baines, K. H., Cruikshank, D., *et al.* 2009. Review of knowledge prior to the Cassini-Huygens mission and concurrent research. Page 9 of Dougherby, M. K., Esposito, L. W., and Krimigis, S. M. (eds.) *Saturn From Cassini-Huygens*. Springer Science+Business Media B.V.

Pan, M., and Chiang, E. 2010. The propeller and the frog. *Astrophys. J. Lett.*, **722**, L178–L182.

Pan, M., and Chiang, E. 2012. Care and feeding of Frogs. *Astron. J.*, **143**, 9.

Pan, M., Rein, H., Chiang, E., and Evans, S. N. 2012. Stochastic flights of propellers. *M.N.R.A.S.*, **427**, 2788–2796.

Pilorz, S., Altobelli, N., Colwell, J., and Showalter, M. 2015. Thermal transport in Saturn's B ring inferred from Cassini CIRS. *Icarus*, **254**, 157–177.

Pollack, J. B. 1975. The rings of Saturn. *Sp. Sci. Revs*, **18**, 3–93.

Pollack, J. B., Summers, A., and Baldwin, B. 1973. Estimates of the sizes of the particles in the rings of Saturn and their cosmogonic implications. *Icarus*, **20**, 263–278.

Poppe, A. R. 2016. An improved model for interplanetary dust fluxes in the outer Solar System. *Icarus*, **264**, 369–386.

Poppe, A. R., and Horányi, M. 2012. On the Edgeworth–Kuiper Belt dust flux to Saturn. *Geophys. Res. Lett.*, **39**, L15104.

Porco, C., Danielson, G. E., Goldreich, P., Holberg, J. B., and Lane, A. L. 1984. Saturn's nonaxisymmetric ring edges at 1.95 R(s) and 2.27 R(s). *Icarus*, **60**, 17–28.

Porco, C. C. 2006. Rings of Saturn (R/2006 S 1, R/2006 S 2, R/2006 S 3, R/2006 S 4). *IAU Circ.*, **8759**, 1.

Porco, C. C., Nicholson, P. D., Cuzzi, J. N., Lissauer, J. J., and Esposito, L. W. 1995. Neptune's ring system. Pages 703–804 of: Cruikshank, D. P., Matthews, M. S., and Schumann, A. M. (eds.), *Neptune and Triton*.

Porco, C. C., Baker, E., Barbara, J., *et al.* 2005. Cassini imaging science: Initial results on Saturn's rings and small satellites. *Science*, **307**, 1226–1236.

Porco, C. C., Helfenstein, P., Thomas, P. C., *et al.* 2006. Cassini observes the active south pole of Enceladus. *Science*, **311**, 1393–1401.

Porco, C. C., Thomas, P. C., Weiss, J. W., and Richardson, D. C. 2007. Saturn's small inner satellites: Clues to their origins. *Science*, **318**(5856), 1602.

Porco, C. C., Weiss, J. W., Richardson, D. C., *et al.* 2008. Simulations of the dynamical and light-scattering behavior of Saturn's rings and the derivation of ring particle and disk properties. *Astron. J.*, **136**, 2172–2200.

Postberg, F., Kempf, S., Hillier, J. K., *et al.* 2008. The E-ring in the vicinity of Enceladus. II. Probing the moon's interior – The composition of E-ring particles. *Icarus*, **193**, 438–454.

Poulet, F., and Sicardy, B. 2001. Dynamical evolution of the Prometheus-Pandora system. *M.N.R.A.S.*, **322**, 343–355.

Poulet, F., Cuzzi, J. N., French, R. G., and Dones, L. 2002. A study of Saturn's ring phase curves from HST observations. *Icarus*, **158**, 224–248.

Poulet, F., Cruikshank, D. P., Cuzzi, J. N., Roush, T. L., and French, R. G. 2003. Compositions of Saturn's rings A, B, and C from high resolution near-infrared spectroscopic observations. *Astronomy and Astrophysics*, **412**, 305–316.

Reffet, E., Verdier, M., and Ferrari, C. 2015. Thickness of Saturn's B ring as derived from seasonal temperature variations measured by Cassini CIRS. *Icarus*, **254**, 276–286.

Rein, H., and Papaloizou, J. C. B. 2010. Stochastic orbital migration of small bodies in Saturn's rings. *Astron. Astrophys.*, **524**, A22.

Renner, S., Sicardy, B., and French, R. G. 2005. Prometheus and Pandora: masses and orbital positions during the Cassini tour. *Icarus*, **174**, 230–240.

Robbins, S. J., Stewart, G. R., Lewis, M. C., Colwell, J. E., and Sremčević, M. 2010. Estimating the masses of Saturn's A and

B rings from high-optical depth N-body simulations and stellar occultations. *Icarus*, **206**, 431–445.

Rosen, P. A., and Lissauer, J. J. 1988. The Titan-1:0 nodal bending wave in Saturn's ring C. *Science*, **241**, 690–694.

Rosen, P. A., Tyler, G. L., Marouf, E. A., and Lissauer, J. J. 1991. Resonance structures in Saturn's rings probed by radio occultation. II – Results and interpretation. *Icarus*, **93**, 25–44.

Salmon, J., Charnoz, S., Crida, A., and Brahic, A. 2010. Long-term and large-scale viscous evolution of dense planetary rings. *Icarus*, **209**, 771–785.

Salo, H. 1995. Simulations of dense planetary rings. III. Self-gravitating identical particles. *Icarus*, **117**, 287–312.

Salo, H. 2012. Simulating the formation of fine-scale structure in Saturn's rings. *Progress of Theoretical Physics Supplement*, **195**, 48–67.

Salo, H., and French, R. G. 2010. The opposition and tilt effects of Saturn's rings from HST observations. *Icarus*, **210**, 785–816.

Scharringhausen, B. R., and Nicholson, P. D. 2013. The vertical structure of the F ring of Saturn from ring-plane crossings. *Icarus*, **226**, 1275–1293.

Schmidt, J., and Tiscareno, M. S. 2013. Ejecta clouds from meteoroid impacts on Saturn's rings: Constraints on the orbital elements and size of the projectiles. *AGU Fall Meeting Abstracts*, Dec.

Schmidt, J., Ohtsuki, K., Rappaport, N., Salo, H., and Spahn, F. 2009. Dynamics of Saturn's dense rings. Page 413 of Dougherby, M. K., Esposito, L. W., and Krimigis, S. M. (eds.) *Saturn From Cassini-Huygens*. Springer Science+Business Media B.V.

Seiß, M., Spahn, F., Sremčević, M., and Salo, H. 2005. Structures induced by small moonlets in Saturn's rings: Implications for the Cassini Mission. *Geophys. Res. Lett.*, **32**, L11205.

Shi, J., Raut, U., Kim, J.-H., Loeffler, M., and Baragiola, R. A. 2011. Ultraviolet photon-induced synthesis and trapping of H_2O_2 and O_3 in porous water ice films in the presence of ambient O_2: Implications for extraterrestrial ice. *Astrophys. J. Lett.*, **738**, L3.

Showalter, M. R. 1991. Visual detection of 1981S13, Saturn's eighteenth satellite, and its role in the Encke gap. *Nature*, **351**, 709–713.

Showalter, M. R., and Burns, J. A. 1982. A numerical study of Saturn's F-ring. *Icarus*, **52**, 526–544.

Showalter, M. R., and Nicholson, P. D. 1990. Saturn's rings through a microscope – Particle size constraints from the Voyager PPS scan. *Icarus*, **87**, 285–306.

Showalter, M. R., Pollack, J. B., Ockert, M. E., Doyle, L. R., and Dalton, J. B. 1992. A photometric study of Saturn's F ring. *Icarus*, **100**, 394–411.

Showalter, M. R., de Pater, I., Verbanac, G., Hamilton, D. P., and Burns, J. A. 2008. Properties and dynamics of Jupiter's gossamer rings from Galileo, Voyager, Hubble and Keck images. *Icarus*, **195**, 361–377.

Showalter, M. R., Hedman, M. M., and Burns, J. A. 2011. The impact of Comet Shoemaker-Levy 9 sends ripples through the rings of Jupiter. *Science*, **332**, 711.

Shu, F. H. 1984. Waves in planetary rings. Pages 513–561 of: Greenberg, R., and Brahic, A. (eds.), *IAU Colloq. 75: Planetary Rings*.

Shu, F. H., Cuzzi, J. N., and Lissauer, J. J. 1983. Bending waves in Saturn's rings. *Icarus*, **53**, 185–206.

Shu, F. H., Yuan, C., and Lissauer, J. J. 1985a. Nonlinear spiral density waves - an inviscid theory. *Astrophys. J.*, **291**, 356–376.

Shu, F. H., Dones, L., Lissauer, J. J., Yuan, C., and Cuzzi, J. N. 1985b. Nonlinear spiral density waves – Viscous damping. *Astrophys. J.*, **299**, 542–573.

Smith, B. A., Soderblom, L., Beebe, R. F., *et al.* 1981. Encounter with Saturn – Voyager 1 imaging science results. *Science*, **212**, 163–191.

Smith, B. A., Soderblom, L., Batson, R. M., *et al.* 1982. A new look at the Saturn system – The Voyager 2 images. *Science*, **215**, 504–537.

Spahn, F., and Sremčević, M. 2000. Density patterns induced by small moonlets in Saturn's rings? *Astron. Astrophys.*, **358**, 368–372.

Spilker, L., Ferrari, C., and Morishima, R. 2013. Saturn's ring temperatures at equinox. *Icarus*, **226**, 316–322.

Spitale, J. N., and Hahn, J. M. 2016. The shape of Saturn's Huygens ringlet viewed by Cassini ISS. *Icarus*, **279**, 141–154.

Spitale, J. N., and Porco, C. C. 2009. Time variability in the outer edge of Saturn's A-ring revealed by Cassini imaging. *Astron. J.*, **138**, 1520–1528.

Spitale, J. N., and Porco, C. C. 2010. Detection of free unstable modes and massive bodies in Saturn's Outer B ring. *Astron. J.*, **140**, 1747–1757.

Spitale, J. N., Jacobson, R. A., Porco, C. C., and Owen, Jr., W. M. 2006. The orbits of Saturn's small satellites derived from combined historic and Cassini imaging observations. *Astron. J.*, **132**, 692–710.

Srama, R., Hsu, H., Kempf, S., and Horanyi, M. 2011. Constraints on the nanoscale minerals on the surface of Saturnian icy moons. *AGU Fall Meeting Abstracts*, Dec.

Sremčević, M., Spahn, F., and Duschl, W. J. 2002. Density structures in perturbed thin cold discs. *M.N.R.A.S.*, **337**, 1139–1152.

Sremčević, M., Krivov, A. V., Krüger, H., and Spahn, F. 2005. Impact-generated dust clouds around planetary satellites: model versus Galileo data. *Planet. Sp. Sci.*, **53**, 625–641.

Sremčević, M., *et al.* 2007. A belt of moonlets in Saturn's A ring. *Nature*, **449**, 1019–1021.

Sremčević, M., Esposito, L. W., Colwell, J. E., and Albers, N. 2011a. B ring gray ghosts in Cassini UVIS occultations. Page 1616 of: *EPSC-DPS Joint Meeting 2011*.

Sremčević, M., Stewart, G., Albers, N., and Esposito, L. W. 2011b. Discovery of B ring propellers in Cassini UVIS and ISS. *AGU Fall Meeting Abstracts*, Dec.

Sremčević, M., Stewart, G. R., Albers, N., and Esposito, L. W. 2012 (Oct.). Discovery of B ring propellers in Cassini UVIS, and ISS. Page 513.06 of: *AAS/Division for Planetary Sciences Meeting Abstracts*. AAS/Division for Planetary Sciences Meeting Abstracts, vol. 44.

Sremčević, M., Stewart, G. R., Albers, N., and Esposito, L. W. 2013. Propellers in Saturn's rings. *AGU Fall Meeting Abstracts*, Dec.

Sremčević, M., Stewart, G. R., Albers, N., and Esposito, L. W. 2014 (Nov.). Propellers in Saturn A and B rings. Page 417.01 of: *AAS/Division for Planetary Sciences Meeting Abstracts*. AAS/Division for Planetary Sciences Meeting Abstracts, vol. 46.

Sun, K.-L., Seiss, M., and Spahn, F. 2015a. Dust in the arcs of Methone and Anthe. *ArXiv e-prints*, Oct.

Sun, K.-L., Schmidt, J., and Spahn, F. 2015b. Particle dynamics in the central ringlet of Saturn's Encke gap. *ArXiv e-prints*, Oct.

Thomas, P. C., Burns, J. A., Tiscareno, M. S., Hedman, M. M., and Helfenstein, P. 2013a. Saturn's mysterious arc-embedded moons: Recycled fluff? Page 1598 of: *Lunar and Planetary Science Conference*. Lunar and Planetary Inst. Technical Report, vol. 44.

Thomas, P. C., Burns, J. A., Hedman, M., *et al.* 2013b. The inner small satellites of Saturn: A variety of worlds. *Icarus*, **226**, 999–1019.

Thomson, F. S., Marouf, E. A., Tyler, G. L., French, R. G., and Rappoport, N. J. 2007. Periodic microstructure in Saturn's rings A and B. *Geophys. Res. Lett.*, **34**, 24203.

Throop, H. B., Porco, C. C., West, R. A., *et al.* 2004. The jovian rings: new results derived from Cassini, Galileo, Voyager, and Earth-based observations. *Icarus*, **172**, 59–77.

Tiscareno, M. S. 2013a. A modified Type I migration model for propeller moons in Saturn's rings. *Planet. Sp. Sci.*, **77**, 136–142.

Tiscareno, M. S. 2013b. *Planetary Rings*. Page 309.

Tiscareno, M. S., Burns, J. A., Hedman, M. M., *et al.* 2006. 100-metre-diameter moonlets in Saturn's A ring from observations of propeller structures. *Nature*, **440**, 648–650.

Tiscareno, M. S., Burns, J. A., Hedman, M. M., and Porco, C. C. 2008. The population of propellers in Saturn's A ring. *Astron. J.*, **135**, 1083–1091.

Tiscareno, M. S., Perrine, R. P., Richardson, D. C., *et al.* 2010a. An analytic parameterization of self-gravity wakes in Saturn's rings, with application to occultations and propellers. *Astron. J.*, **139**, 492–503.

Tiscareno, M. S., Burns, J. A., Sremčević, M., *et al.* 2010b. Physical characteristics and non-Keplerian orbital motion of "propeller" moons embedded in Saturn's rings. *Astrophys. J. Lett.*, **718**, L92–L96.

Tiscareno, M. S., Hedman, M. M., Burns, J. A., and Castillo-Rogez, J. 2013a. Compositions and origins of outer planet systems: Insights from the Roche critical density. *ApJL*, **765**, L28.

Tiscareno, M. S., Hedman, M. M., Burns, J. A., Weiss, J. W., and Porco, C. C. 2013b. Probing the inner boundaries of Saturn's A ring with the Iapetus -1:0 nodal bending wave. *Icarus*, **224**, 201–208.

Torres, P. J., Madhusudhanan, P., and Esposito, L. W. 2013. Mathematical analysis of a model for moon-triggered clumping in Saturn's rings. *Physica D Nonlinear Phenomena*, **259**, 55–62.

Tseng, W.-L., Ip, W.-H., Johnson, R. E., Cassidy, T. A., and Elrod, M. K. 2010. The structure and time variability of the ring atmosphere and ionosphere. *Icarus*, **206**, 382–389.

Tseng, W.-L., Johnson, R. E., and Ip, W.-H. 2013. The atomic hydrogen cloud in the saturnian system. *Planet. Sp. Sci.*, **85**, 164–174.

Tyler, G. L., Marouf, E. A., Simpson, R. A., Zebker, H. A., and Eshleman, V. R. 1983. The microwave opacity of Saturn's rings at wavelengths of 3.6 and 13 CM from Voyager 1 radio occultation. *Icarus*, **54**, 160–188.

Vahidinia, S., Cuzzi, J. N., Hedman, M., *et al.* 2011. Saturn's F ring grains: Aggregates made of crystalline water ice. *Icarus*, **215**, 682–694.

van Allen, J. A. 1982. Findings on rings and inner satellites of Saturn of Pioneer 11. *Icarus*, **51**, 509–527.

Ward, W. R. 1997. Protoplanet migration by nebula tides. *Icarus*, **126**, 261–281.

Ward, W. R., and Hahn, J. M. 1994. Damping of orbital inclinations by bending waves. *Icarus*, **110**, 95–108.

Warren, S. G. 1984. Optical constants of ice from the ultraviolet to the microwave. *Appl. Opt.*, **23**, 1206–1225.

Weidenschilling, S. J., Chapman, C. R., Davis, D. R., and Greenberg, R. 1984. Ring particles – Collisional interactions and physical nature. Pages 367–415 of: Greenberg, R., and Brahic, A. (eds), *IAU Colloq. 75: Planetary Rings*.

Weiss, J. W., Porco, C. C., and Tiscareno, M. S. 2009. Ring edge waves and the masses of nearby satellites. *Astron. J.*, **138**, 272–286.

West, R., Lavvas, P., Anderson, C., and Imanaka, H. 2014. *Titan Haze*.

Williams, G. A., and Murray, C. D. 2011. Stability of co-orbital ring material with applications to the Janus–Epimetheus system. *Icarus*, **212**, 275–293.

Winter, O., Sfair, R., Mourao, D., *et al.* 2014. The Janus–Epimetheus ring and the micrometeoroids's flux at Saturn. Page 3642 of: *40th COSPAR Scientific Assembly*. COSPAR Meeting, vol. 40.

Winter, O. C., Mourão, D. C., Giuliatti Winter, S. M., Spahn, F., and da Cruz, C. 2007. Moonlets wandering on a leash-ring. *M.N.R.A.S.*, **380**, L54–L57.

Winter, O. C., Mourão, D. C., and Giuliatti Winter, S. M. 2010. Short Lyapunov time: a method for identifying confined chaos. *Astron. Astrophys.*, **523**, A67.

Wyatt, M. C. 2008. Evolution of debris disks. *Ann. Rev. Astron. Astrophys.*, **46**, 339–383.

Yasui, Y., Ohtsuki, K., and Daisaka, H. 2014. Gravitational accretion of particles onto moonlets embedded in Saturn's rings. *Astrophys. J.*, **797**, 93.

Zebker, H. A., and Tyler, G. L. 1984. Thickness of Saturn's rings inferred from Voyager 1 observations of microwave scatter. *Science*, **223**, 396–398.

Zebker, H. A., Marouf, E. A., and Tyler, G. L. 1985. Saturn's rings – Particle size distributions for thin layer model. *Icarus*, **64**, 531–548.

Zhang, Z., Hayes, A. G., Janssen, M. A., *et al.* 2017. Cassini microwave observations provide clues to the origin of Saturn's C ring. *Icarus*, **281**, 297–321.

Zubko, V.G., Mennella, V., Colangeli, L., and Bussoletti, E. 1996. Optical constants of cosmic carbon analogue grains. – I. Simulation of clustering by a modi ed continuous distribution of ellipsoids. *M. N. R. A. S.*, **282**, 1321–1329.